University of Pisa

Faculty of Engineering

PhD Course in
Chemical and Material Engineering
XXVI Cycle

SSD Ing-Ind 34

PhD Thesis

Study, development and realisation of microfluidic devices able to generate nonlinear concentration gradients

Tutor
Eng. Giovanni Vozzi
Prof. Eng. Roberto Mauri

PhD student
Gianni Orsi

2014

Abstract

Biomolecular gradients are an important, evolutionarily-conserved signalling mechanism for guiding growth, migration, and differentiation of cells within dynamic, three-dimensional environments of living tissues. Gradients play essential roles in many phenomena including development, inflammation, wound healing, and cancer. Interest in elucidating these phenomena has led to the development of numerous in vitro methods for exposing cells to chemical gradients.

The core of this research was to develop and to realise engineered devices able to generate nonlinear concentration gradients of soluble species in cell culture chambers, in order to study cell response. During this PhD the 2D concentration gradient generator paradigm was first analysed in all its aspect, from theory (using fluid-electrical analogies) to simulation (CFD simulation showing accurately the species distribution within the device), ending with the realisation and experimental validation of the developed device. While advancing with the work, practical issues proper of those systems were faced, critically analysed and finally engineered solutions were proposed and applied, in order to make possible a reliable cell perfusion within the device.

Concentration gradient concept was extended from common 2D to 3D, because soluble gradients in-vivo act in a 3D environment, thus

stimulating a 3D scaffold with a 3D concentration gradient could lead in mimicking a more physiological environment. Gradients of mechanical properties could lead cell migration and differentiation, and also them are in 3D in living tissues, i.e in the cartilage-subchondral bone system.

For this reason a novel 3D concentration gradient maker, able to generate steady three-dimensional concentration gradients, was developed and realised.The device was applied as an hydrogel maker, fabricating hydrogel matrixes with a 3D gradient of mechanical properties. Those construct could be used as smart scaffolds.

It is also important to guarantee the possibility to monitor environmental variables such as pH either into microfluidic devices and smart scaffolds, with not invasive/destructive methods.

For this reason we developed 2D pH sensitive surfaces, with the perspective to be integrated into micro devices. To create a biocompatible 2D pH sensor, sensitive nanoparticles could be immobilised inside a hydrogel matrix, in order to guarantee a proper fluorescence Signal to Noise Ratio. Using extended range pH sensitive nanoparticles developed by the University of Nottingham, we developed sensitive surfaces. The idea of sensitive surfaces was then extended using inkjet printing coupled with Sol-gel method, using as polymeric matrix a Gelatine/Glycidoxypropyltrimethoxysilane (GPTMS) system, because the picoliter-size ink droplets evaporate quickly, thus allowing quick sol-gel transitions on the printed surface. An Ink with the pH sensitive nanoparticles was successfully printed with a modified Inkjet printer.Thanks to inkjet printing is also possible to think at

3D smart scaffolds of Gelatine/GPTMS, which inner behaviour could be investigated by optical fluorescence techniques, such as confocal microscopy, in order to have in-situ measurements.

Devices and techniques developed during this PhD could have applications in biological research, as integrated tools for simultaneously stimulating and monitoring live cells, in order to gain knowledge about their behaviour. Also pharmacological profiling with "one-shot" experiments, so drawing the dose-response curve of a compound in a single experimental run, could be an application of interest.

To my family and Caterina

If you can't explain it ***simply****, you don't understand it well enough.*

Albert Einstein

Contents

Introduction

Biomolecular gradients are an important, evolutionarily-conserved signalling mechanism for guiding growth, migration, and differentiation of cells within dynamic, three-dimensional (3D) environments of living tissues. Gradients play essential roles in many physiological phenomena including development, inflammation, wound healing, and cancer. Interests in elucidating these phenomena led to the development of numerous in vitro methods for exposing cells to chemical gradients. Traditional in vitro gradient-generating methods have been instrumental in shaping our current understanding of gradient signalling, but they are not ideal for examining the quantitative/combinatorial nature of gradient signalling due to their inability to produce precise, user-defined gradients with tailored spatial and temporal profiles. Chemical gradients generated by traditional methods often evolve unpredictably/uncontrollably over space and time, becoming difficult to characterise quantitatively. The gradients form and dissipate within a few hours, greatly limiting the range of cell types and questions that can be studied. Elucidation of the complexities of gradient signalling requires more detailed knowledge and control over the spatiotemporal distribution of chemical species in the extracellular environment, and the ability to directly visualise cells within that environment. Because molecules diffuse isotropically and unrestricted in free solution, maintaining one or more gradients requires con-

stant supply and removal of molecules at precise locations within well-defined liquid volumes. Microfluidic technology, whereby fluids can be routed precisely and with significant levels of automation at micrometer/nanometer dimensions, provides an appealing strategy to control the fluid flow necessary to create gradients on a scale suitable for cellular studies. Recently, several microfluidic devices have been developed for generating gradients that are predictable, reproducible, and easily quantified. The milestone in the field is undoubtedly the first gradient maker developed by Whitesides group in 2000 (1). The rapid evolution of the microelectronics industry during the past 30 years produced numerous tools and methods for fabricating micrometer-scale features in and on various substrates with very high precision and at relatively low cost. Realisation that these advances in microfabrication technology could be used to control the micrometer-scale environment, or microenvironment, of cultured cells has led to the development and rapid expansion of two closely related fields: Biomedical Electromechanical Systems (BioMEMS) and Microfluidics. BioMEMS and Microfluidics research have provided a plethora of ways to explore how cells respond to micrometer- scale modifications of their physical and chemical environments. Because microfabrication allows creation of well-defined cell culture environments with micrometer precision, quantitative characterisation and experimental reproducibility are greatly enhanced.Recently, researchers have focused on the need for better gradient-generating methods. Microfluidic cell culture environments are uniquely suited to achieve the level of quantification and gradient control required to correlate observed cell responses with specific gradient characteristics, and elucidate how cells integrate different biomolecule gradients to achieve particular biological responses. The precise dimensions of micro devices, combined with detailed understanding of fluids behaviour at the micrometer scale, confers unique advantages to gradient makers over traditional

methods. Fluids flowing in micrometer-scale conduits, or microchannels, are dominated by the viscous properties of the fluid at the expense of inertial forces generated by the fluid. This specialised flow regime, called laminar flow, is well-understood both conceptually and mathematically (2) allowing the movement of momentum, heat, and chemical species inside a microfluidic device to be calculated with great accuracy(3). When used with commercially-available Computational Fluid Dynamics (CFD) packages, the defining equations developed for laminar flow can be used to characterise an existing device or help prototype new devices to create specific, engineered cell culture environments. Virtual prototyping streamlines the fabrication process, ensuring that the appropriate cell culture environment will be created in the actual device. Microfluidic devices have practical advantages that increase the throughput and reduce the cost of gradient experiments when compared to traditional gradient-generating methods. The parallel nature of microfabrication methods, or scalability, and the small physical footprint of most microfluidic devices allow multiple gradient-generating cell culture environments to be constructed and placed in the same physical space typically occupied by a single traditional set up. The greater experimental throughput reduces the time and cost of each experiment. In addition, the small volumes of microfluidic devices require vastly smaller amounts of reagents. This reduces the cost of each experiment and enables the creation of biomolecule gradients that would be too expensive to create using traditional gradient-generating methods. Microfluidic gradient generators have been used to infect cells with graded concentrations of virus (4), generate gradients of mechanical stiffness (5) and cell-adhesion molecules in synthetic extracellular matrices, (6) create adsorbed gradients of extracellular matrix proteins (7, 8, 9), induce proliferation and differentiation in neural stem cells (10), and examine the effects of various biomolecule gradients on the chemotaxis of neutrophils

(11, 12, 13, 14), bacteria (15, 16), and sperm (17). Steady-state gradient generators create distinct regions of constant concentration to form time-invariant gradients across a cell culture area. Although the time-invariant gradients they create do not mimic the spatio-temporal gradients cells encounter in vivo, they do provide detailed, quantitative information about how biomolecule concentration or gradient profile influences cell behaviour. These concentration and profile dependencies will provide appropriate context for in vitro studies seeking to understand how gradient timing and spatiotemporal dynamics influence cell behaviour. Steady-state gradient generators developed to date have employed one of two different strategies. The microfluidics Gradient Makers (GM), exploit the lack of convective mixing that occurs between adjacent fluid streams under laminar flow. Because mixing only occurs via diffusion perpendicular to the direction of fluid flow, chemical gradients form with characteristics (i.e. shape, concentration range, etc.) that depend upon the composition, flow rates of the respective streams and the length of time the streams have been in contact. The resulting gradients are constant as long as the input flow rates and compositions are constant. They are capable of creating and maintaining a wide variety of gradients for periods of time limited only by the supply of reagents (i.e. size of inlet reservoir, cost, etc.). Rapid formation of steady-state gradients allows correlations to be made between observed cell responses and specific gradient characteristics (11, 12). By carefully choosing the concentration of the input fluid streams and the manner in which they are combined, a wide variety of gradient shapes and concentration ranges can be created. Adjustment of the inlet flow rates also offers the user some dynamic control over the gradient formed within the device. The main disadvantage of parallel flow gradient generators is the requirement for constant fluid flow. Flow rates typically have units in mL/min, requiring many millilitres of reagents for a long-term experiment. For

some biomolecules, the required liquid volumes are cost-prohibitive. Constant fluid flow also imparts mechanical forces on cells that can introduce experimental bias (18), and may initiate intracellular signalling cascades that can confound experimental results or damage cells. Jeon and colleagues of Whitesides' group (1) developed a parallel flow gradient generator (Figure 1) that has been used to study the effects of soluble biomolecule gradients on neutrophil migration (11, 12, 13), neural stem cell differentiation (10), and breast cancer cell chemotaxis (19).

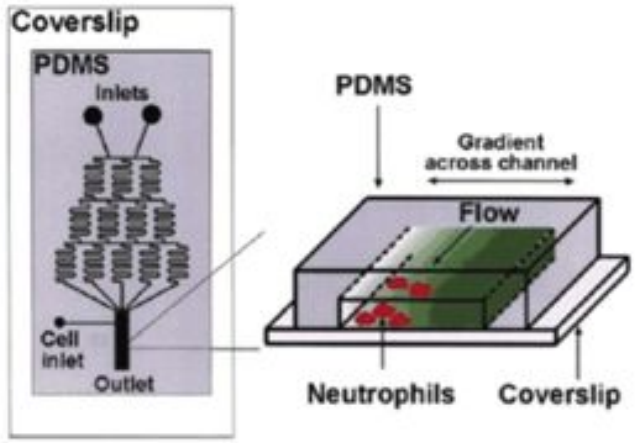

Figure 1: 2D schematic of the device with 3D exploded view of the gradient generated downstream of the microfluidic mixer.

The device has also been used to create substrate-bound biomolecule gradients to direct the growth of hippocampal neurons (20). This GM however only forms gradients under constant fluid flow, which consumes significant amounts of reagents, and flushes away potentially important cell-secreted factors. The

device can generate combinatorial gradients with two factors (13) and theoretically more, but the gradients can only be arranged along a single axis orthogonal to the direction of flow. The user can dynamically modify the gradient via inlet flow rate control but is constrained by the upstream mixer design. However microfluidics-based gradient makers allow to enhance our understanding of fundamental biological processes, due to their high efficiency for analysis of cell behaviour in two-dimensional environments. Toxicity tests could be easily implemented with this kind of systems, giving the possibility to run a single "one-shot" test instead of the classical protocols, that are usually based on a multi concentration set of experiments.

The core of this PhD thesis is to study, to develop and to realise engineered devices able to generate nonlinear concentration gradients in cell culture chambers. It is important that those concentration gradients are nonlinear (in particular with power laws), because that behaviour mimics the classical toxicity dose-response tests that are normally performed in several companies (pharmacological, environmental, chemical and so on). During this research the 2D GM idea was first analysed in all its aspect, from theory (using fluid-electrical analogies) to simulation (CFD simulation showing accurately the species distribution within the device), ending with realisation and experimental validation of the developed device. While advancing with the work however, practical issues proper of the GM systems were faced:

- hydrophobicity;
- bubbles nucleation which clogs micro channels and also destroy the cells in the culture;
- challenges in a reliable cell seeding;

- easiness of using the GM for biological research.

Any of those issues was critically analysed and a solution was proposed. During this research the concept of GM was extended: **from 2D to 3D**. In fact soluble gradients in-vivo acts in a 3D environment, so stimulating a 3D scaffold with a 3D concentration gradient could lead in mimicking a more physiologically close environment. Gradients of mechanical properties could lead cell migration and differentiation, and also them are in 3D in living tissues. Substrate rigidity has been recognised as an important property that affects cellular physiology and functions. While the phenomenon has been well recognised, understanding the underlying mechanism may be greatly facilitated by creating a microenvironment with designed rigidity patterns. A novel 3D Concentration Gradient Maker, able to generate stable three-dimensional concentration gradients, was then developed. It could be used for scaffolds perfusion with a 3D concentration gradient, but it could also be applied as an hydrogel maker, making hydrogel matrixes with a controlled 3D gradient of mechanical properties, which could be used as "smart scaffolds" components. Computational Fluid Dynamic analysis was used to develop the device; Finite Elements Analysis and experimental studies were used to validate the 3D gradient of stiffness.

The device could have several applications in studying phenomena related to cell chemotaxis and mechanotaxis, but also on differentiation in simultaneous presence of gradients of both soluble chemical species and substrates stiffness.

Currently there is great interest in designing smart material capable not only to drive cell processes, but also to monitor them. This idea could in principle be realised by transforming a conventional scaffold into a "smart scaffold" that acts as both cell stimulus source, and sensor for monitoring cell activities. So this was the last thing needed into the developed systems: the possibility to

monitor environmental variables inside the scaffolds or on a surface, with not invasive methods such as fluorescence microscopy. For this reason engineered pH sensitive surfaces were developed, in collaboration with the University of Nottingham. An automated image analysis system was also developed in order to quickly extract pH measurements from 2D fluorescence images of the sensitive surfaces.

Chapter 1

Development of a 2D concentration gradient generating device

In this chapter the principles of design and the architecture of the planar microfluidic gradient maker with the shape of any given monotonic function are described. Each microfluidic network is fed by two separate source solutions and delivers at its outlet a set of N solutions that differ each other in concentration. The microfluidic gradient makers can be seen, in fact, as fluidic function generators, where a continuous function is represented as $2^N + 1$ points discrete function. In this case of a concentration gradient shaped as e^{10x} with $x \in [0, 3]$ was designed, constructed and characterised either by CFD and experiments. Also a MATLAB library able to quickly design microfluidic gradient makers and export them to a CAD compatible format (.DXF) was developed.

1.1 Introduction

Microfluidic gradient generators or gradient makers (GM) can produce spatial and temporal distributions of biochemical molecules by controlling convective and diffusive transport processes. Low Reynolds number characterises the advection in microscale, so the flow regime is laminar. In laminar flow, streams of miscible fluids flow side-by-side and mix by diffusion without turbulent mixing. This offers a reliable approach for controlling the distribution of diffusing molecules under conditions where unpredictable factors such as eddies are eliminated. Flow-based gradient generators produce concentration gradients by utilising this basic physical phenomenon. Streams of fluids composed of different chemical species or concentrations are brought together in a microfluidic channel where the solutes are allowed to diffuse across the interface as they flow down the microchannel. The Peclet number (Pe) provides a valid indication for predicting the formation of the diffusive profile between laminar streams. The magnitude of Pe dictates the length of the channel required to fully homogenise the concentration of laminar streams. Based on the well-characterised mixing process at the interface of laminar flow streams, a wide variety of custom concentration gradient profiles can be generated by using microchannel networks designed to control input and output streams.

1.2 2D Microfluidic gradient maker: how it works

Whitesides (1) first developed this type of gradient generator with a premixing microchannel network. In this design, a microchannel network similar to a "Christmas tree" is used with a series of bifurcated microchannels that repetitively split and recombine, as explained in previous chapter. Solutions of different concentrations are first introduced at the inlet and the fluid streams are

repeatedly split, mixed (in serpentine channel regions) and recombined to produce multiple streams of mixed solutions having different proportions of input solutions. At the end of the premixing network, these streams are brought together into a chamber to generate a gradient across it. The splitting ratios at each branching point can be calculated by treating the fluidic microchannel network as an equivalent electronic circuit. This modelling allows effective calculation of output stream concentrations and can be used to predict the gradient profiles. Campbell et al. (21) used modified premixing networks to generate gradients with reduced stages of flow splitting and mixing (Figure 1.1).

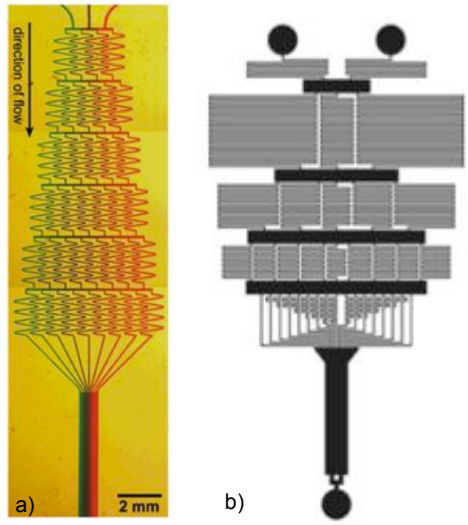

Figure 1.1: View of different paradigms for making microfluidic GM: a) Whitesides' model; b) Campbell model. At is it possible to see the network of a) in N=6 layers has 8 different inlets in the gradient chamber, while b) in N=4 layers has 17 inlets in the gradient chamber. b) is then more compact and accurate than a).

The microchannel network consisted of horizontal and serpentine channels that sequentially mix and redistribute flow streams. The microchannel network

precisely controls the distribution of flow streams with the aid of serpentine channels having different hydraulic resistances. By constructing microchannel networks according to the proposed mathematical scheme, any gradients of defined monotonic profile can be generated. In my microdevice the microchannels are 50 μm wide each one, and the layer structure is derived from Campbell's work (21). The chamber is 6 mm wide and $\simeq$ 20 mm long, in order to reach the same surface area of a single well of a 16-well plate. This was done because we could compare the results that we will obtain with the same amount of cells of a single well, knowing that for making a standard toxicity test several wells with different drug concentration are needed. The concentration gradient in the chamber was approximated with a series of step functions, dependent on the number of microchannels in last layer (Figure **??**.

The optimal configuration I found was 4 layers with $2^4+1 = 17$ microchannels in last layer. However by advancing in the chamber the function becomes more smooth because to diffusion. It is important to set the mean velocity in the chamber low enough to have a smooth gradient, but high enough to maintain it stable on chamber length avoiding larger diffusion effects. Other considerations on main chamber velocity are based on cell survival due to shear stress and oxygen/nutrients demand.

Similarly to the devices introduced originally by Whitesides (1, 22) the microfluidic device described in this section consists of two parts: a gradient-making network and a gradient chamber. The gradient-making network is fed by two source solutions with different concentrations injected into the device through separate inlets, and it generates N solutions of different concentrations. These solutions are directed into the test channel through N separate narrow channels (the lower row of serpentine channels in Figure 1.3. In this section an $N = 17$ (Fig. 1.3) was chosen. It is convenient to number the serpentine channels from

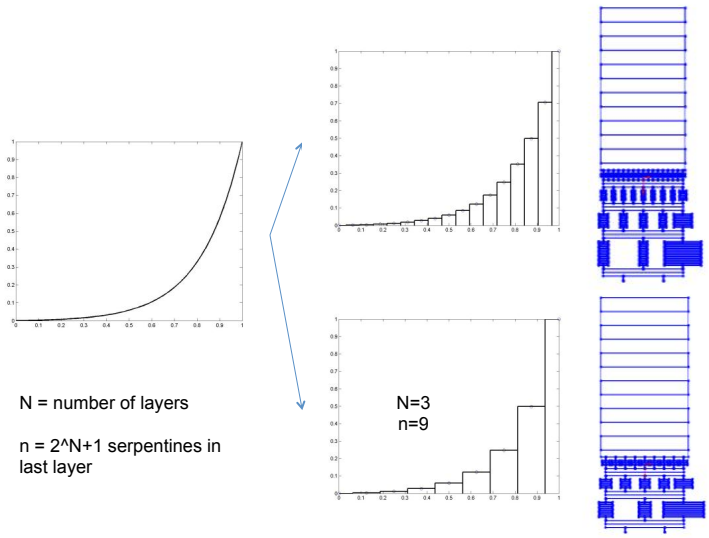

Figure 1.2: The concentration profile discretisation depending on the number of layers N. The same function can be represented from different microfluidic networks, differentiating only for the quality of approximation. The images comes as the results of the MATLAB library for quickly designing microfluidic devices.

left to right, and designate the concentration in the n-th serpentine channel as c_n, where $1 \leq n \leq N$. The set of c_n is constructed to be a discrete representation of the desired concentration profile across the chamber $c(y)$. Streams of injected solutions have the same volumetric flux and approximately the same width in the test channel, $\Delta y \simeq w/N$, where w is the width of the chamber. Exceptions are the two streams at the edges, which are somewhat wider because the flow velocity near the edges of the test channel is lower than in the middle, so the section needed to have the same flow rate as other streams is larger. As the flow advances along the chamber, the initial discontinuity in concentration between adjacent streams gradually disappears due to molecular diffusion. The charac-

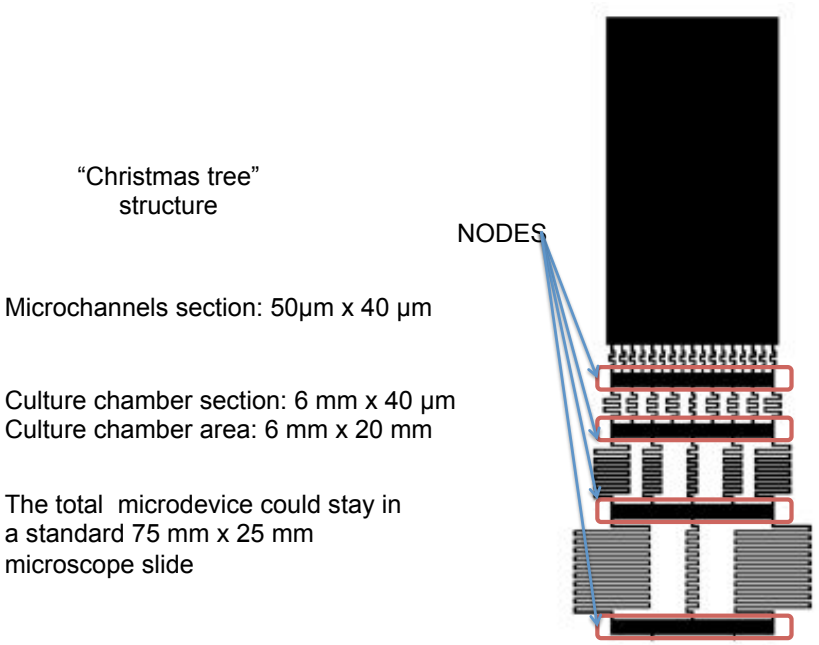

Figure 1.3: Concept view of the microfluidic device.

teristic diffusion time is $\tau_D = \Delta y^2/D$, corresponding to a characteristic distance $\Delta x = U\tau_D$ from the stream merging point at the beginning of the test channel. Here D is the coefficient of diffusion of the solute, and U is the mean flow speed. (For the actual chamber, the analysis is somewhat more complicated because of variation of the channel width in the beginning.) At distances $x > \Delta x$, $c(y)$ is a smooth function. Molecular diffusion across the test channel also levels off the non-uniformity of $c(y)$ on the scale of the whole channel, making $c(y)$ increasingly different from its desired shape as x and the residence time in the flow increase. The characteristic time of this unwanted levelling off can be estimated as $w^2/D = (N\Delta y)^2/D = N^2\tau_D$, corresponding to a distance $N^2\Delta x$ from the

beginning. These simple arguments show that a suitable working range of x, at which the distribution $c(y)$ is both smooth and closely matching the set of c_n,is given by $\Delta x < x \ll N^2 \Delta x$. Furthermore,at $\Delta x < x \ll N^2 \Delta x$, the concentration profile has little sensitivity to variations of U. Therefore, it is essential that N is sufficiently large, $N^2 \gg 1$, for the device to operate well. In addition to providing a long working region in the test channel, a large value of N also allows accurate definition of $c(y)$ by the discrete set of c_n. The latter is especially important for nonlinear $c(y)$, because the molecular diffusion between the adjacent streams in the test channel tends to reduce the curvature of the concentration profile. The gradient-making network consists of consecutive stages, each comprised of a wide horizontal channel (the "node", see Figure 1.3), and a set of narrow serpentine channels downstream from it, the "resistances".The nodes distribute the flow emerging from the upstream serpentine channels over a larger number of the downstream serpentine channels. In addition, due to low flow resistance of the nodes, all serpentine channels belonging to the same stage have equal pressures at their inlets and equal pressures at their outlets, acting as expected. The function of the serpentine channels is to provide diffusive mixing of solutions injected into them and to generate a homogeneous solution of an intermediate concentration, which is fed into a downstream horizontal channel. The diffusive mixing is facilitated by the small width and large length of the serpentine channels, resulting in small characteristic diffusion time and large liquid residence time, respectively. Volumetric flux through a channel, $q = \Delta P/R$, is defined by the difference in pressure between the inlet and the outlet, ΔP, and by the channel flow resistance, R. The flow resistance is proportional to the channel contour length, $R = kL$, where k is the same for all serpentine channels, as they all have the same width and depth, $w_s = 50\mu m$ and $h = 40\mu m$, respectively. In accord with (21), serpentine channels belonging to the same

stage have different lengths, L, leading to different R and different q through the channels. Variability of q makes it possible to mix solutions in individually adjustable proportions and to generate concentration profiles with a variety of shapes. The stream from an individual serpentine channel of the k-th stage is split between 3 serpentine channels of the $(k + 1)$th stage. An exception are streams from the channels at the edges, which are split between 2 channels of the $(k + 1)$th stage. The gradient-making networks are built so that each odd-numbered serpentine channel of the $(k + 1)$th stage is fed by a single channel of the kth stage and thus carries solution of the same concentration, as depicted in Figure 1.4.

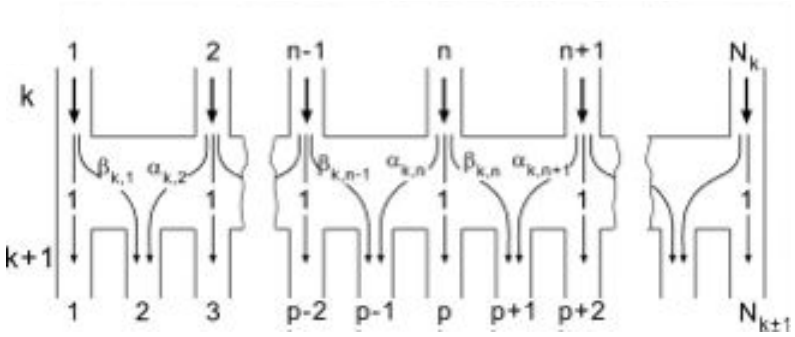

Figure 1.4: Splitting and redistribution of flux in a node. Schematic diagram showing splitting and redistribution of flux between serpentine channels of the kth and $(k+1)$th stages and illustrating the meaning of the coefficients α and β. Serpentine channels of the kth and $(k+1)$th stages are shown as vertical channels at the top and bottom, respectively, and are numbered from 1 to N_k and from 1 to $N_k + 1$, respectively. Coefficients at the arrows show portions of flux in the channel of the $(k + 1)$th stage supplied by the channel of the kth stage.

Each even-numbered serpentine channel of the $(k + 1)$th stage is fed by two

adjacent channels of the kth stage, and a solution with an intermediate concentration is generated in it. The numbers of solutions with different concentrations within the k-th and $(k+1)$th stages, N_k and N_{k+1}, are connected by a recurrence relation, $N_{k+1} = N_k + (N_k - 1)$. Given i.e $N_1 = 3$, it is possible to derive $N_k = 2^k + 1$ and $k = log_2(N_k - 1)$, meaning that the number of stages in this kind networks increases logarithmically with the number of distinct concentrations at the network outlet. Construction of a gradient-making network begins with the definition of the desired shape of the concentration profile, $c(y)$, and the number of stages in the network. To keep the notation more compact, the n-th serpentine channel (as counted from the left) of the k-th stage as channel $< k, n >$, see Figure 1.4. The concentration and volumetric flux in channel $< k, n >$ will be designated as $c_{k,n}$ and $q_{k,n}$, respectively. The resistance and length of channel $< k, n >$ will be designated as $R_{k,n}$ and $L_{k,n}$, respectively. The concentrations in the serpentine channels of the last stage are chosen as a discrete set approximating the desired profile. In the case of an N=4 exponential profile, i.e. $c(y) = e^{10y}$, with $y \in [0, 3]$, we have a discrete concentration set $c_{N,n}$ in the last stage as shown in Figure 1.2. With the condition that each odd-numbered channel of the $(k+1)$-th stage be fed by a single channel from the kth stage uniquely defines the set of concentration in the serpentine channels of the 3rd stage. Applied recursively from bottom to top, the same condition defines the concentrations in the serpentine channels of the 2nd and 1st stages, as well as in the two channels connecting the inlets with the horizontal channel of the 1st stage. We notice that $c_{0,1}$ and $c_{0,2}$ are the concentrations of the solutions injected into the inlets.Volumetric fluxes in serpentine channels of the k-th stage are specified by concentrations in channels of the $k-$th and $(k+1)$-th stage and fluxes in channels of the $(k+1)$-th stage (Figure 1.4). If channel $< k, n >$ is neither the first nor the last of the k-th stage, it supplies flux to three channels

of the $(k+1)$-th stage: $< k+1, p-1 >$,$< k+1, p >$,and $< k+1, p+1 >$,where $p = 2n-1$. Channel $< k, n >$ is the sole source of flux supplied to channel $< k+1, p >$. Therefore, the flux in channel $< k, n >$ is calculated as

$$q_{k,n} = \alpha_{k,n} q_{k+1,p-1} + q_{k+1,p} + \beta_{k,n} q - k + 1, p + 1 \tag{1.1}$$

Here, $\alpha_{k,n}$ and $\beta_{k,n}$ are portions of the volumetric fluxes in channels $< k+1, p-1 >$ and $< k+1, p+1 >$, respectively, which are supplied by channel $< k, n >$; $0 \leq k \leq 3$ and $1 \leq n \leq 2^k+1$.Once solution fed to channel $< k+1, p-1 >$ (from $< k, n >$ and $< k, n-1 >$) and to channel $< k+1, p+1 >$ (from $< k, n >$ and $< k, n+1 >$) are mixed, the concentrations in these two channels become $c_{k+1,p-1} = \alpha k, n c_{k,n} + \beta_{k,n-1} c_{k,n-1}$ and $c_{k+1,p+1} = \beta_{k,n} c_{k,n} + \alpha_{k,n+1} c_{k,n+1}$, Fig. 1.4. In order to find $\alpha_{k,n}$ and $\beta_{k,n}$, we further notice that $\alpha_{k,n} + \beta_{k,n-1} = 1$ and $\beta_{k,n} + \alpha_{k,n+1} = 1$. Taken together, these equations give $c_{k+1,p-1} = \alpha_{k,n} c_{k,n} + (1-\alpha_{k,n}) c_{k,n-1}$ and $c_{k+1,p+1} = \beta_{k,n} c_{k,n} + (1-\beta_{k,n}) c_{k,n+1}$. Finally, it is possible to derive

$$\alpha_{k,n} = \frac{c_{k+1,p-1} - c_{k,n-1}}{c_{k,n} - c_{k,n-1}} \tag{1.2}$$

$$\beta_{k,n} = \frac{c_{k+1,p+1} - c_{k,n+1}}{c_{k,n} - c_{k,n+1}} \tag{1.3}$$

For the first channel of a stage, the coefficient α is zero, and for the last channel of a stage the coefficient β is zero. The coefficients $\alpha_{k,n}$ and $\beta_{k,n}$ are readily calculated from the values of concentrations in the serpentine channels (which are uniquely defined by the concentrations in the channels of the last stage, $c_n = cN, n$) and then plugged into 1.1. The system of 1.1 is closed by specifying the volumetric fluxes in the serpentine channels of the last stage, $q_{N,n}$, which are all equal to 1 in relative units. The values of $q_{k,n}$ are calculated

iteratively, stage by stage from bottom to top. The calculated values of $q_{k,n}$ are used to select $L_{k,n}$. For all pairs of channels $< k, n >$ and $< k, m >$ belonging to the same k-th stage, we have an equation

$$\frac{L_{k,n}}{L_{k,m}} = \frac{q_{k,m}}{q_{k,n}} \tag{1.4}$$

setting coefficients of proportionality between the channel lengths. This equation gives a general recipe for building a functional network. Nevertheless, it does not specify the ratios between lengths of serpentine channels belonging to different stages. These ratios and the actual values of $L_{k,n}$ can be rationally selected based on the characteristic time of diffusive mixing in a serpentine channel and the mean flow velocity, $U_{k,s}$, in the shortest channel of the stage, $< k, s >$, at typical operation conditions of the device. For any given stage, the shortest serpentine channel has the shortest residence time of liquid in it, $\tau_{k,s} = L_{k,s}/U_{k,s} \propto L_{k,s}/q_{k,s} \propto L_{k,s}^2$, and $\tau_{k,s}$ has to be sufficiently long to allow complete diffusive mixing in the channel. In the network under consideration, the shortest serpentine channel of a stage is always the channel in the middle. Since pressures at the device inlets are equal, the ratio of $L_{0,1}$ and $L_{0,2}$ is given by $L_{0,1}q_{0,1} = L_{0,2}q_{0,2}$. There is no diffusive mixing in the channels of the 0th stage, however. Therefore, $L_{0,1}$ and $L_{0,2}$ do not have to be proportional to the lengths of the serpentine channels of other stages. The network described above is constructed to generate an exponential profile shaped as $c(y) = e^{10y}$, where the left and right edges of the test channel correspond to y = 0 and y = 1, respectively, and the maximum concentration is e^{10} in relative units. However until now with this algorithm proposed by (21) we calculated just the relative length and weights. For settling effective velocities we must set a velocity in one channel or in the culture chamber, and the other are calculated consequently. The gradient-making microchannel network can be used to generate any given

concentration profile with one essential limitation: $c(y)$ has to be a monotonic function. This limitation originates from the fact that the concentration in any serpentine channel (except for channels at the edges) is a weighted average of the concentrations in the two adjacent channels, precluding local minima or maxima of concentration in the networks with two inlets. Concentration profiles with local maxima and minima can be produced by using networks with three or more inlets or by directing streams emerging from several independent networks into a single test channel. With the common planar architecture of the microfluidic devices, each channel can have only one or two channels immediately adjacent to it. Hence, a stream emerging from a channel can be directly merged with only one or two other streams, and by splitting and merging streams from a planar array of N channels, not more than $N-1$ new mixtures can be produced (this limitation is lifted if a 3D microchannel network is used). The logarithmically small number of steps (stages), $k = log_2(N_k - 1)$ (21) needed to generate a given number of distinct concentrations allows significant reduction in area occupied by the network and in pressure required to drive flow through the network compared with Whitesides (1, 22).

1.3 A MATLAB library for drawing custom microfluidic concentration gradient generators

One of the main problems faced was to generate quickly different designs of microfluidics GM in CAD environment. In fact the microfluidics networks were constructed using Campbell's (21) algorithm , but drawing them quickly and reliably with an automated software was a different thing. Doing a parametric CAD drawing did not give so much flexibility, so a different approach was chosen. The chosen solution was to develop a MATLAB library, able to draw

custom geometries in Drawing eXchange Format (.DXF files), which is a common CAD format. The geometry file could be easily imported in common CAD environments (i.e. Solidworks) and drawing programs (i.e. CorelDraw), making it either a tool for speed the simulation/design process and soft-lithography mask realisation (Figure 1.5).

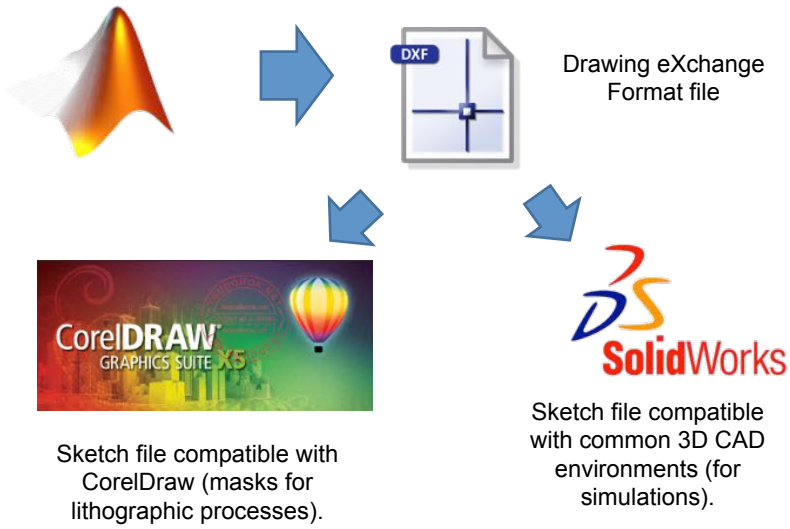

Figure 1.5: Concept of the MATLAB library for generating micro devices geometry. Thanks to the .DXF format, it is easy to use the library as design tools for soft-lithography masks and 3D drawings.

The output .DXF file, that could be easily imported as sketch in common 3D CAD environments and then extruded up to desired height. The now 3D CAD file can easily be exported to simulations software such as Ansys/COMSOL or directly exported for a 3D Printing, if needed (Figure 1.6). Further details about the library are in **Appendix 1**. Parameters the MATLAB library needs for properly working are explained in Table 1.1.

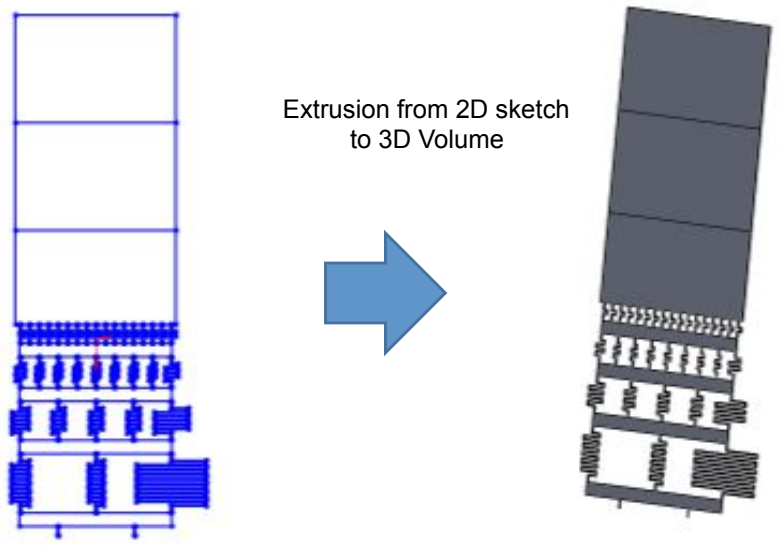

Figure 1.6: Example of sketch extrusion to 3D.

1.4 Characterisation

1.4.1 Numerical Model

1.4.1.1 Governing Equations

In general the governing equations for describing the behaviour of an incompressible isothermal fluid are:

$$\nabla \cdot \mathbf{u} = 0 \tag{1.5}$$

$$\rho \mathbf{u} \cdot \nabla \mathbf{u} + \nabla p = \nabla \cdot [\mu(\nabla \mathbf{u} + \nabla \mathbf{u}^{+})] + \rho \mathbf{g}. \tag{1.6}$$

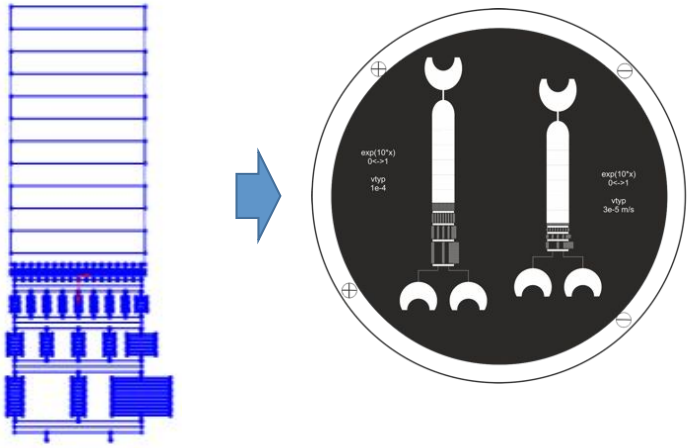

Figure 1.7: Example of .DXF to soft-lithography mask process.

Here $\mathbf{u}$ denotes the velocity vector, ρ is the fluid density, p the pressure, μ the viscosity, $\mathbf{g}$ the gravity acceleration. In case the diffusion of a specie is involved, we have to add the advection-diffusion equation (4.3) to the governing equations:

$$\mathbf{u} \cdot \nabla \phi = D \nabla^2 \phi. \tag{1.7}$$

In this case we chose to treat the species diffusion as the mixing of two identical fluids, each one diffusing in the other with a diffusion coefficient D, as did in (23) and (24), instead of tracking the specie concentration as a scalar. By imagining to add a small amount of contaminant, i.e. a dye, to one of the fluids (which therefore continue to have the same physical properties) we have that ϕ indicates the (normalized) dye mass fraction. The characteristics of the velocity and concentration fields can be described through the Reynolds (Re),

Table 1.1: MATLAB Library Parameters

Parameter	Example Value	Description
N	4	Number of layers of the microchannels network
D	$5 \cdot 10^{-10}\, m^2/s$	Diffusion coefficient of used specie
w	$50\,\mu m$	Microchannels width
h	$40\,\mu m$	Microchannels height
lchamber	$6\,mm$	Chamber width
vtypical	$10^{-4}\, m/s$	Average velocity within the chamber
eta	$10^{-3}\, Pa \cdot s$	Fluid Viscosity
rho	$10^{3}\, Kg/m^3$	Fluid Density
f	e^{10x}	Desired Profile

Peclet (Pe) and Schmidt (Sc) numbers

$$Re = \frac{Ud}{\nu}; \qquad Pe = \frac{Ud}{D} = ReSc; \qquad Sc = \frac{\nu}{D}; \tag{1.8}$$

where U is the mean velocity, while the characteristic fluid length d is assumed to be the hydraulic diameter, i.e.,

$$d = \frac{2wh}{w+h} \tag{1.9}$$

where w and h are chosen channel width and height, respectively. Sc represents the Schmidt number, which take into account the ratio between momentum diffusivity and mass diffusivity, and is used to characterize fluid flows in which there are simultaneous momentum and mass diffusion convection processes..

1.4.1.2 Mesh and Boundary Conditions

Simulations were performed using the commercial software Ansys 13, with the FLUENT fluid dynamics package. The grid consisted of cubic elements with $5\mu m$ edge, corresponding, approximately, to the viscosity-dependent typical dimension $\mu/\rho U$. This leads to a mesh of 80 elements in each cross section of the mixing channel, thus in agreement with the recommendation by (25), regarding how to accurately describe the velocity fields. A second order discretisation scheme was used to solve all the governing equations; using higher-order scheme did not lead to any significant change. Simulations were typically considered converging when the normalised residuals for velocities were stationary with iterations and fell below 10^{-6}.The steadiness of the solution with iterations was also assessed by checking the velocity and concentration field in the outlet section of the mixing channels at different iterations. As mentioned above, here the concentration field is discretised using the same mesh size as the velocity field. Clearly, since in our case $Sc = O(10^3)$, so that $Pe \gg Re$, a rigorous simulation of mass diffusion should require a grid resolution much finer than that of the velocity field (see the extensive discussion in (26), about this issue). This, however, would lead to unacceptably long computation times. In fact a grid independence study was performed on the velocity field, showing that, repeating the numerical simulation with smaller cubical elements, the simulations give results that do not differ from the original simulation. A quite similar analysis was also conducted by (23, 24), using a different geometric setup. In any case, it should be stressed that the simulations allow only a qualitative analysis of the concentration fields, while further studies (experiments, above all !!) are required to better quantify them. The boundary conditions consist of no-slip velocity and no-mass-flux at the channel walls, a constant ambient pressure at the chamber outlet, while at

the two inlets a plug flow with velocities v_1 and v_2 calculated with the algorithm were imposed. Since that the velocity field is developed after few microns, as demonstrated by the formula for the length to fully developed velocity profile (le) in laminar flow (eq. 1.10):

$$le = 0.06 \cdot Re \cdot d \tag{1.10}$$

that in this case give approximately $2\,\mu m$, because $Re \ll 1$.

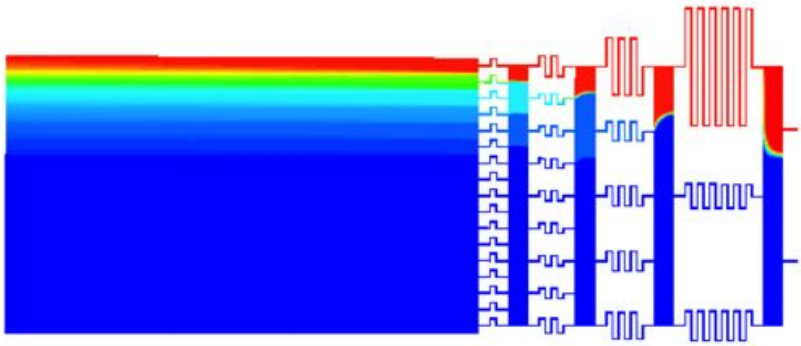

Figure 1.8: View of CFD simulation of concentration profile within the microdevice.

1.4.2 Materials and Methods

The device was realised in Poly-Dimethyl-Siloxane (PDMS) by using Soft-Lithography techniques. Briefly, silicon 100 wafers were spin-coated with SU-8 photoresist, baked to drive away the solvent, and then exposed to UV light in a Bottom Side Mask Aligner through a mask. The mask was created using Corel Draw 15.0, by importing the geometry files previously created in MATLAB, and printed on

a transparency using a commercial Linotronic-Hercules 3300 dpi high-resolution line printer. Exposed photoresist was then developed and subsequently the wafers were baked (Figure 1.9).

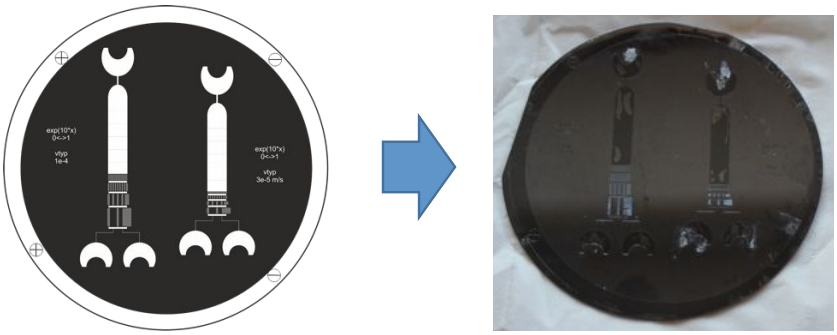

Figure 1.9: Workflow: from mask design to silicon wafer realisation.

PDMS prepolymer was prepared by mixing the commercially available prepolymer and catalyser (Sylgard 184 kit) in a 10:1 w/w ratio. The mixture was degassed under vacuum to eliminate bubbles created during mixing. The prepolymer solution was cast on the master and placed under vacuum once again to remove bubbles that may have been introduced. PDMS was cured by baking for 4 h at 65 degrees. After cooling to room temperature, the PDMS was peeled from the silicon master. Holes were then punched at inlets and outlet and silicone tubes were connected (Figure 1.10).

The integration of PDMS chips, with pumps or connections to reservoirs, has been found to pose serious difficulties because of its associated problems in leaking. Here are presented different approaches for sealing the microfluidic device, without the aid of commercially available connectors and using commonly available consumables in the laboratory. The PDMS mould is bonded with glass in two ways: using hydrophilic and hydrophobic means. Hydrophilic bonding

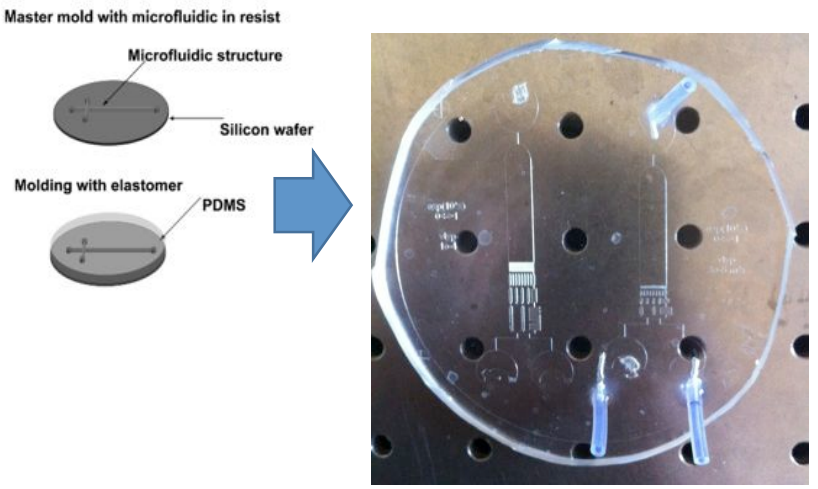

Figure 1.10: Workflow: making the PDMS micro channels part.

involves using a plasma cleaner for oxidation. Hydrophobic bonding is done using a PDMS mixture. Here, we report easy and cost effective hydrophilic and hydrophobic bonding protocols. The hydrophilic bonding can also be performed without the use of conventional plasma oxidation.

1.4.2.1 PDMS -PDMS Hydrophobic Bonding

A serious issue that I faced was the sealing of the device. It was not possible to bond the device to the glass with mechanical pressure. The device showed pouring from the inlets and between the microchannels due to non-uniform sealing pressure. I resolved the problem by using hydrophobic PDMS to PDMS bond for sealing it. It was coated a plastic slide with a thin layer ($\simeq 10\mu m$ thickness) of PDMS mixture with a spin coater, then it was heated at 70 °C for 15 mins (this makes the PDMS hardened but still sticky). Then it was placed the PDMS mould on the sticky PDMS surface. It is important, in order to avoid wrinkles

and air gaps, laying the mould down from one end to the other. The system was cured for 1 h at 70 degrees (Figure 1.11).

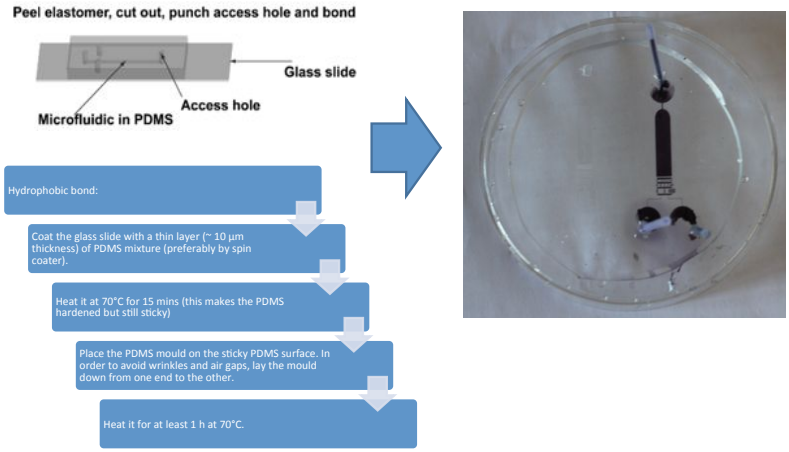

Figure 1.11: Workflow: protocolo for PDMS-PDMS hydrophobic bonding

1.4.2.2 PDMS - Glass Hydrophilic Bonding

Oxidation of PDMS using plasma changes the surface chemistry of PDMS and produces silanol terminations (SiOH) on its surface. This helps make PDMS hydrophilic for thirty minutes. This process also makes the surface resistant to the adsorption of hydrophobic and negatively-charged molecules. In addition, plasma oxidation of PDMS could be used to functionalise the surface of PDMS with the trichlorosilane or to covalently bond PDMS (on an atomic scale) on an oxidised glass surface by the creation of a Si-O-Si bond. Whether the surface of PDMS is oxidised in plasma or not, it does not allow the water, glycerol, methanol or ethanol to infiltrate and deform it. Thus, it is possible to use PDMS with these fluids without fear of micro-structure deformation. The plasma oxida-

tion protocol require to expose the PDMS and the glass to Oxygen Plasma for 30 s (Power 80 W, Pressure 2 mPa), then make the surfaces in contact with a light pressure. The now highly hydrophilic surfaces will stick. In order to enhance the strength of the seal, by promoting Si-O-Si bonds, 2 h of curing at 80 °C must be performed (Figure 1.12). Another technique is to oxidise the glass slide and the PDMS mould in freshly prepared Piranha solution. Piranha solution is 2:1 v/v H_2SO_4 : H_2O_2. The glass slide has to be dipped in the solution for 5 mins, while the PDMS mould for 10 secs. Dipping the PDMS mould for larger times may lead to damage to the mould because of strong oxidation. Then samples has to be rinsed in deionised water at least three times. This step is required to remove any residual acid as well as to prevent hydrophobic recovery. After that both the glass slide and the PDMS must be dried using a compressed stream of dry nitrogen gas. Finally the mould must be placed over the glass slide and heated at 80 degrees for 2 hours. The Piranha protocol, however, showed to be less repeatable than the Oxygen Plasma one, and if not done carefully can cause transparence losses in the PDMS.

1.4.3 Validation

A syringe pump was connected to inlets, and flow was forced trough the system (Figure 1.13) The syringe pump can control two different syringes, imposing different flow rates on them, calculated before. Syringes were filled with different dyes, in order to see the concentration gradient. It was found that the best dyes are inks from InkJet Printers, due to their tendency to not form aggregates and consequently not clog the microchannels.

In particular the device was tested with a 1:100 v/v diluted HP Inkjet cartridge Black Ink injected into inlet 2. The liquid injected into inlet 1 was just deionised water (Figure 1.14). The flow rate in both channel was set to the

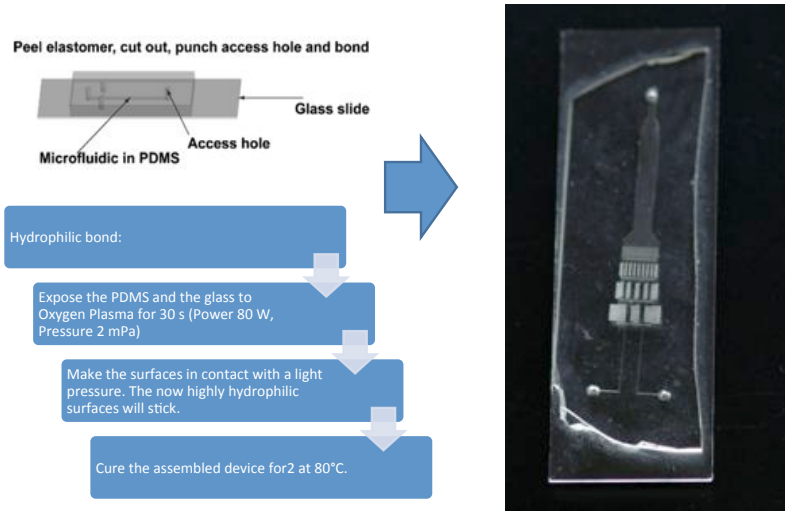

Figure 1.12: Workflow: protocol for PDMS-Glass hydrophilic bonding.

values q_{01} and q_{02} previously calculated in section 1.2. Another protocol was developed to remove air bubbles from the device, which have the effect to destroy the microfluidic gradient because to their interference with the flow. The device was submerged into water, and then placed in vacuum for several hours, in order to have air to flow out the microdevice and be substituted by water. Experimental concentration profile was analysed by standard image processing techniques. In particular, once converted the image to greyscale, the image brightness was inversely correlated to the dye concentration (more black implies more concentration of dye). Then it was selected a line in the image and the relative brightness, once normalised, was evaluated against analytical and simulated concentration profile 4.26. The image was previously filtered with a median filter to smooth the noise.

Profiles of dye distribution within the chamber, $c(y)$, matched the desired

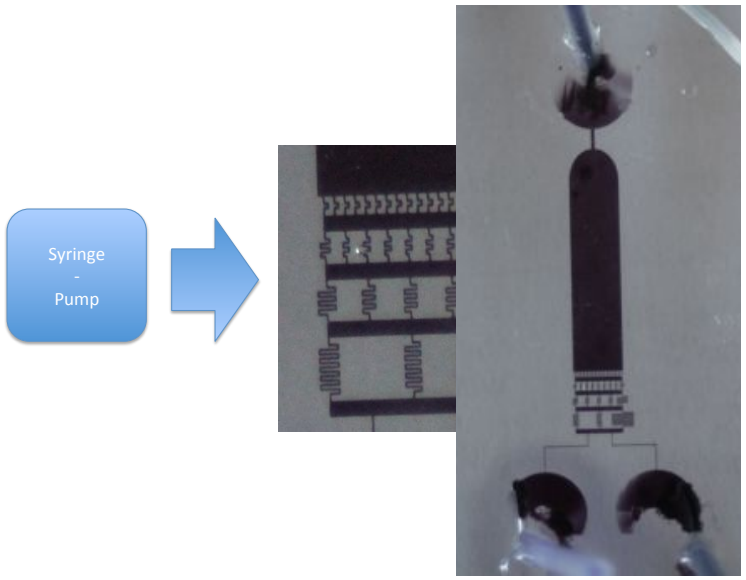

Figure 1.13: View of the micro device filled with diluted black Ink.

concentration profile (Figures 4.26 and 1.16). Notably, there are plateaus of zero and maximal concentration in the marginal regions. A better fit would be obtained if the volumetric fluxes of the streams with zero and maximal concentration injected at the edges would be reduced, because due to the parabolic shaped velocity profile their streams occupies more width than central streams.

1.5 Results

The simulation was shown to closely follow the desired profile (Figure 1.17).

As it is possible to see experimental results almost agreed with analytical and simulated one (Figure 1.18), so the fluid dynamics of the microfluidic device is fully characterised and understood. As it possible to see in figures (Figure

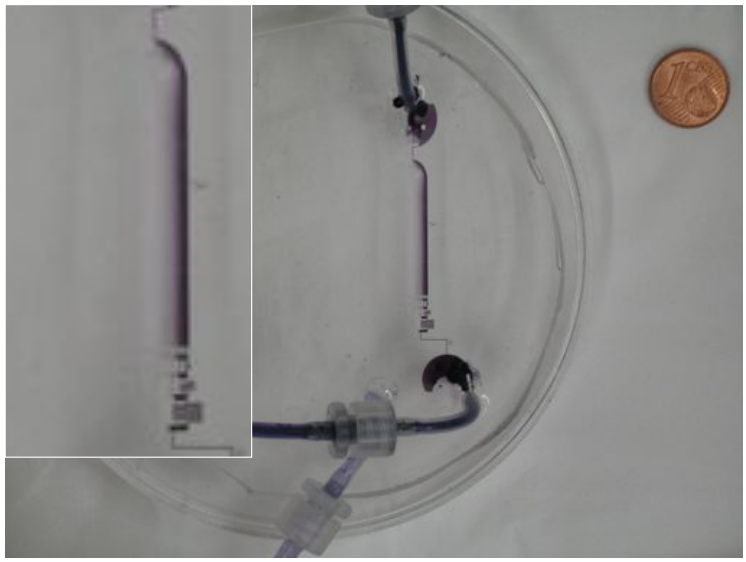

Figure 1.14: View of the Ink gradient developing within the chamber.

1.16), also in the intermediate zones of the micro device the matching between simulated and experimental data is almost perfect. The device works properly as designed. For the fabrication technology the best was the PDMS-Glass one with the aid of a gas plasma, thanks to its easiness of use and repeatable behaviour. Also the post-plasma initial hydrophilicity of the micro device helps the fluid filling the micro channels thanks to capillary interactions. The PDMS-PDMS hydrophobic bonding demonstrated higher resistance to device burst, but was discarded because the making process was too long for practical purposes. The Piranha bonded devices showed performances similar to plasma bonded ones, but the making process is longer and more hazardous.

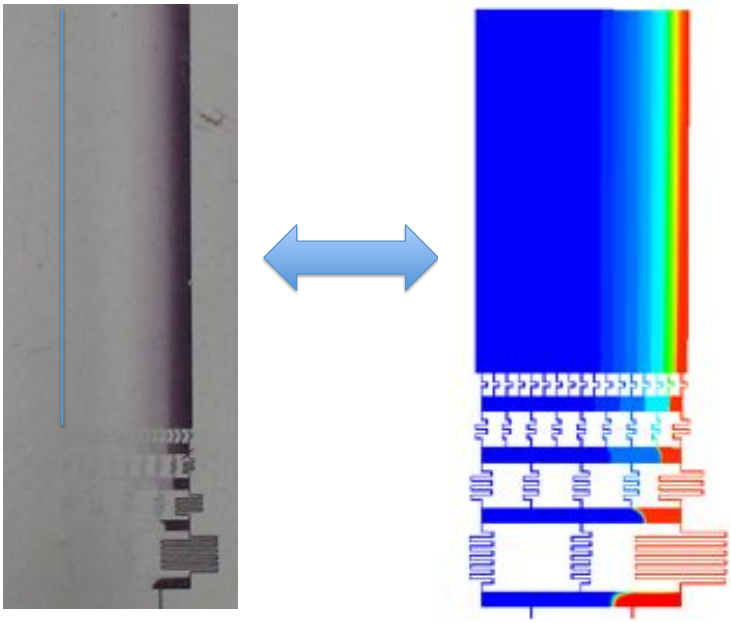

Figure 1.15: View of the Ink gradient within the device vs the simulation. As it is possible to see the concentration profiles are closely matched.

1.6 Conclusions

An engineered microfluidic concentration GM was successfully developed and realised. The match between expected, simulated and experimental behaviour of the device is very close. However the device was still not suitable for cell culturing, because the hydrophobicity of PDMS was an obstacle to GM perfusion, causing unwanted burst due to the local high pressure. Even PDMS-Glass devices after 40 min experienced an hydrophobic recovery, in fact. This causes serious issue when people trying to seed cells from the outlet due to the massive formation of air bubbles (effect also amplified in medium culture respect to

water), and very high shear stresses during cell injection phase.

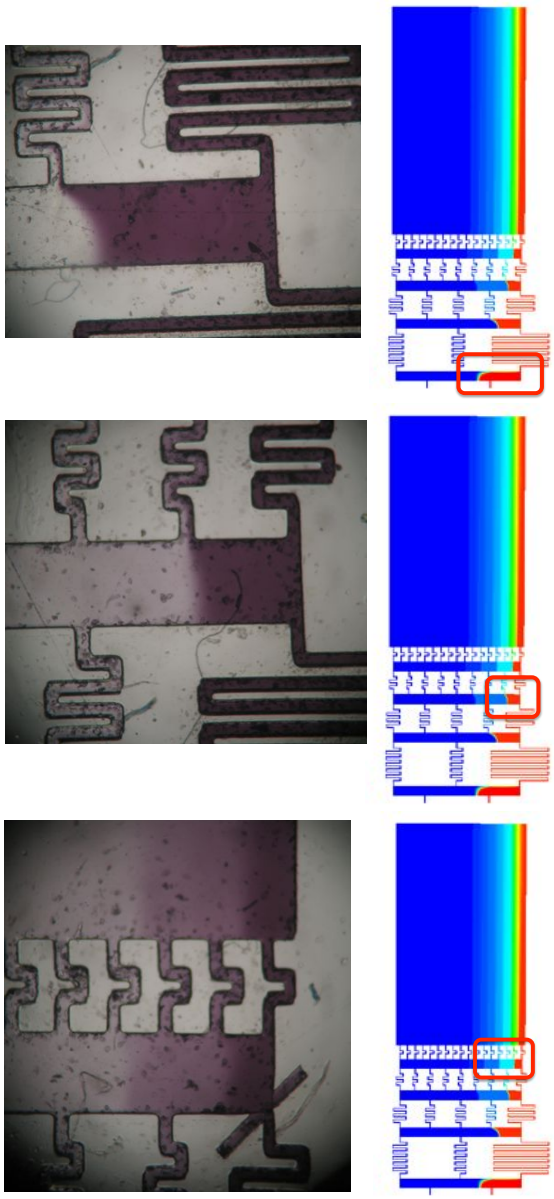

Figure 1.16: Details of the experimental Ink distribution within the device vs the simulation one. As it is possible to see the concentration profiles are closely matched.

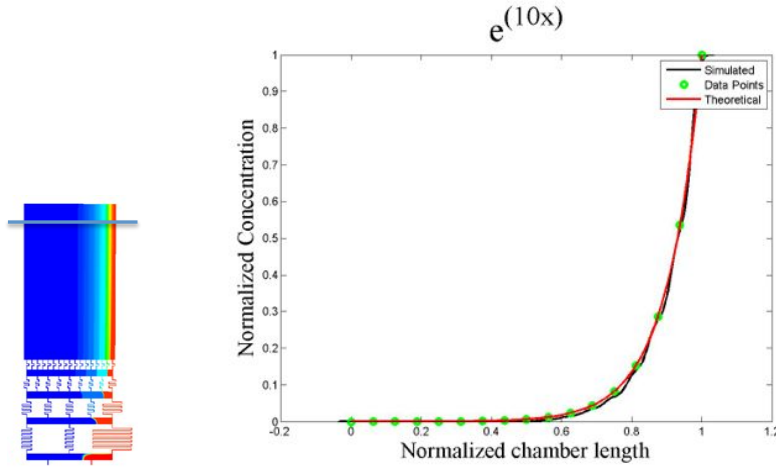

Figure 1.17: Comparison between desired and simulated profile. The two profiles are very close. The green points represents the discretisation points used for approximating the exponential profile

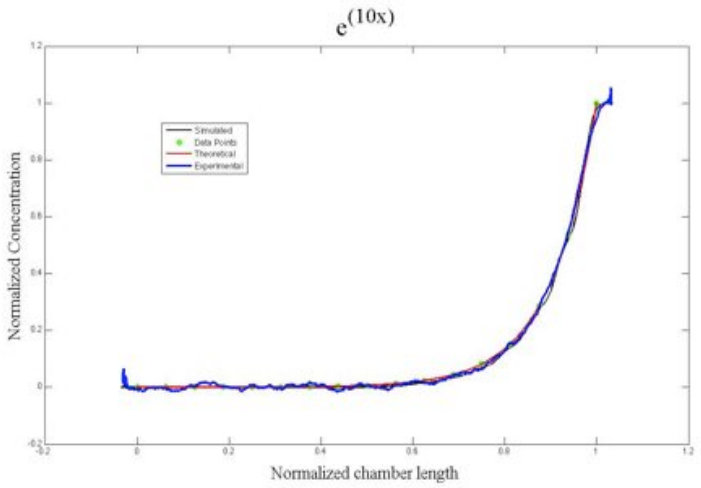

Figure 1.18: Comparison between desired,simulated and experimental concentration profile. All the curves almost collapsed into one, sign that the device is working properly. The green points represents the discretisation points used for approximating the exponential profile

Chapter 2

2D Microfluidic Bioreactor: new design

Designing a microfluidic perfusion culture system involves many decisions, including the choice of materials, microfluidic layout, fabrication process, packaging, and sterilisation technique. PDMS has appealing properties: low autofluorescence, biocompatibility and low cost. Despite the advantages it presents high hydrophobicity, and also water vapour and gas can readily permeate PDMS, potentially causing unwanted evaporation and bubble formation. In order to improve the micro device, a new layout was generated. The culture chamber was enlarged, so that a glass coverslip seeded with cells in a normal multi well or petri dish could be enclosed. There was the need of making long time stable hydrophilic PDMS, in order to allow capillary forces to remove the air bubbles. Using nonionic surfactants mixed with the PDMS it was obtained hydrophic behaviour. The PDMS was then enclosed between two Plexiglas pieces, allowing it to be sealed just by pressure. A CFD analysis of device "robustness" was done, evaluating the sensitivity of formed gradient to different flow conditions from nominal case.

2.1 Introduction

Designing a microfluidic perfusion culture system involves many decisions, including the choice of material, microfluidic layout, fabrication process, packaging, and sterilisation technique (27, 28). Furthermore requirements such as sterility and biocompatibility are non-negotiable. Other design parameters are dictated by the intended application and assay method; the incorporation of cells into the system contributes another important factor that affects the system design and fabrication. For example, surface modification procedures to facilitate cell attachment and cell culture configuration, i.e. cells are cultured as 2D monolayers or in 3D scaffolds or gels, may subsequently place restrictions on the design, fabrication and assembly of the system. PDMS has good properties for microscopy; it has low autofluorescence when compared with many plastics used in microfabrication (29), making it suitable for fluorescence imaging applications. PDMS presents an appealing set of properties that are suitable for constructing general microfluidic perfusion culture systems. Despite the advantages to using PDMS, it presents high hydrophobicity, and also water vapour and organic solvents can readily permeate PDMS, potentially causing unwanted evaporation and changes in osmolality, (30, 31) which is detrimental to cell culture. Microfluidic perfusion culture systems are also susceptible to failure by air bubble disruption of the cell culture due to their enclosed nature, small dimensions and the constant introduction of new culture media. The presence of air bubbles in a microfluidic perfusion culture system is undesirable as they obstruct fluid flow and kill cells at the gas-liquid interface. Air bubbles can arise from residual air due to incomplete priming of the system or spontaneous formation at defect sites. Air bubble kinetics can be divided into 2 phases i.e. nucleation and growth. The growth of existing air bubbles within the microfluidic system

is governed by the Laplace equation: $P_i = P_{atm} + 2\sigma/R$ where P_i (Pa) is the internal bubble pressure, P_{atm} (Pa) is the ambient pressure outside the air bubble, σ (N/m) is the surface tension and R (m) is the air bubble radius (32). The condition for stability i.e. $P_i > P_{atm}$ tends to drive gas diffusion out of the air bubble, which helps to collapse it. Therefore, priming of the microfluidic perfusion culture system under high pressure, known as *blind filling* (33), helps to collapse residual air bubbles that are not flushed out of the system. The GM developed in the previous chapter was fine from an engineering point of view. In fact it was able to generate large controlled concentration gradients in few millimetres, but it proved to be unreliable for cell culturing, due to the hydrophobicity of PDMS. The main issue was:

1. Hydrophobic recovery of PDMS. In fact gas plasma treated PDMS in fact shows an hydrophobic recovery in around 40 minutes, leaving out the possibility of sterilising and stocking it before the use;
2. The second problem was the difficulty in removing bubbles in microchannels (effect also amplified in medium culture respect to water). This also caused device bursts due to the local high pressure in trying to remove bubbles from micro channels;
3. Another problem was the entrance of the bubbles in the device. Bubble enter the device due to PDMS gas permeability (in incubator the effect was increased respect to room temperature/pressure);
4. Finally the device should be sealed by just pressure, allowing to insert a glass/plastic slide already with seeded cells into the device and starting the experiment, but with just seeding the cells via outlet channel injection let them experience an high grade of shear stress, and so a large part of

cells died. For this reason this system did not allow to control cell seeding density. ...

In order to improve the micro device, a new layout was generated. It showed a bigger chamber, where a glass coverslip seeded with cells in a normal multi well or petri dish could be enclosed (Figure 2.1). Also there was the need of making stable hydrophilic PDMS, in order to allow capillary forces to remove the air bubbles themselves. An approach was to use nonionic surfactants mixed with the PDMS in order to make it act with an hydrophilic behaviour. The hydrophilic PDMS was then enclosed between two thick Plexiglas pieces, allowing it to be sealed just by pressure (Figure 2.2). A CFD analysis of the "robustness" of the new layout was done, in order to understand the sensitivity of the formed gradient to different flow conditions from the nominal case.

2.2 The new layout

As depicted in Figure 2.1, the new layout is composed by a 19 mm x 23 mm culture chamber, where a small coverslip (18 mm x 18 mm) could be inserted after cells seeding over it. Since the chamber is big respect previous case, also the channels should be larger. In fact now the channel width w is 250 μm and channel height h is 200 μm. The number of layers N in this case is three instead of four in order to reduce the size of the device. The serpentine channels were generated with the MATLAB library described in the previous chapter. The hydrophilic PDMS was then enclosed between two thick Plexiglas pieces, allowing it to be sealed just by pressure (Figure 2.2), because the PDMS itself acts as a gasket.

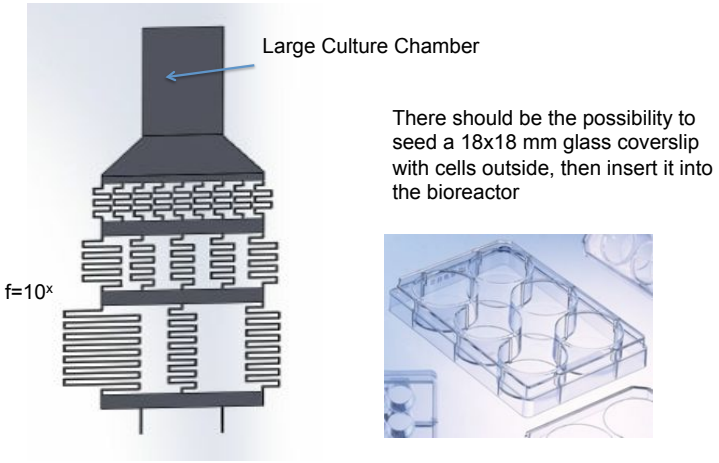

Figure 2.1: View of the gradient maker new layout. The new chamber size allows cells to be seeded and let proliferate outside the GM.

2.2.1 "Node" size determination

Literature about gradient makers is wide, but no considerations about the proper "Node" size are available (Figure 2.3). In this section we demonstrated how to choose the proper node size for a microfluidic gradient maker, by just minimising a proper cost function. In a microfluidic GM node it is important to limit the lateral solute diffusion, in order to avoid unwanted mixing in the node, and choose the lateral hydraulic resistance as low as possible, in order to avoid lateral pressure differences that could lead to not easily controllable flow patterns. As reported in (34), the expression of hydraulic resistance in a square channel is given by the following expression:

$$R = \frac{12\eta L}{wh^3}\left[1 - \sum_{n,odd}^{n} \frac{1}{n^5}\frac{192}{\pi^5}\frac{h}{w}\tanh\left(n\pi\frac{w}{2h}\right)\right]^{-1} \tag{2.1}$$

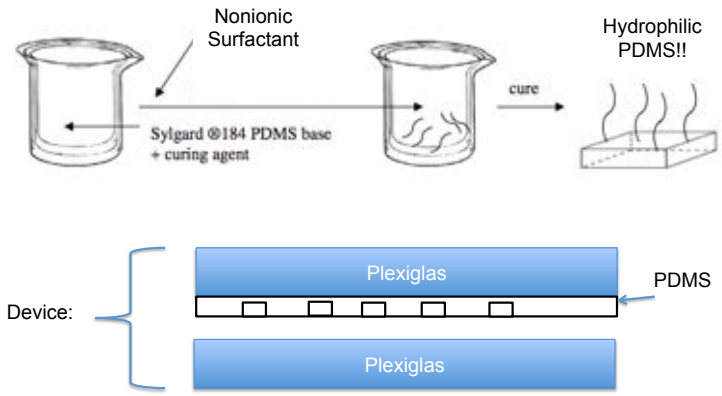

Figure 2.2: View of the new device fabrication method. Top: steps for making hydrophilic PDMS. Bottom: scheme of the new device sealing. Two thick Plexiglas pieces connected by nuts and bolts clamp the hydrophilic PDMS.

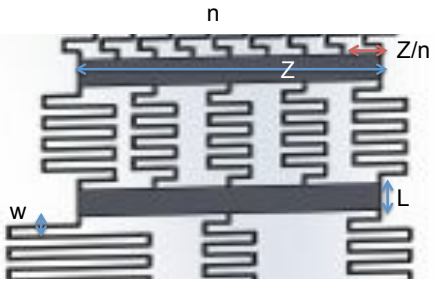

Figure 2.3: View of the typical lengths within the micro device. Z represents the Node Width, L the Node Length and w is micro channels width. n is the number of micro channels that are feeder by the last node.

but for practical calculation purposes the series can be truncated at the 25^{th} term. By labelling with L the node length (Figure 2.3), and with w the serpentine

micro channel typical width, we can write equation (2.2):

$$\frac{R\,Transversal}{R\,Longitudinal}(L) = \frac{w}{L}\frac{\left[1 - \sum_{n,odd}^{n} \frac{1}{n^5}\frac{192}{\pi^5}\frac{h}{w}\tanh\left(n\pi\frac{w}{2h}\right)\right]}{\left[1 - \sum_{n,odd}^{n} \frac{1}{n^5}\frac{192}{\pi^5}\frac{h}{L}\tanh\left(n\pi\frac{L}{2h}\right)\right]} \tag{2.2}$$

The equation represents the ratio between the lateral hydraulic resistances of a node of length w and a node with length L, and has to be kept as low as possible. From the opposite side we have lateral diffusion into the micro channel. The lateral diffusion length is directly proportional to $Pe_{Node} = UZ/D$. We can consider the transversal diffusion of a particle into the flow as 2D diffusion because mass transfer is dominated by diffusion only in cross-sections, as happens in microchannels. In 2D in a time t a particles will travel an average distance $L_{diff} = \sqrt{4Dt}$ from its starting point. If the fluid is moving forward with an average velocity U we have a diffusion length of $d = UL^2/4D$. After that distance we can consider the concentration profile to be almost homogeneous. Since the node width Z is 38 mm, the average velocity U in the node becomes $(v_{01} + v_{02})w/Z = Uw/Z$. The typical diffusion distance of interest, however, is not the whole node width, but the minimum distance between the serpentine channels inlets, namely Z/n, where n is the maximum number of micro channels that go out from the node. But the interface between two fluid streams is placed near to the half distance between two serpentine inlets, so the effective free diffusion space goes down to $Z/2n$. For robustness purposes, finally, we decided to split in half this distance another time, so the maximum (considered node) diffusion length is $Z/4n$. If we consider the ratio between the Node Length and the chosen Diffusion Length we can write equation (2.3):

$$\frac{Node\ Length}{Diffusion\ Length}(L) = L\left[U\frac{w}{Z}\left(\frac{Z}{n}\right)^2\frac{1}{4D}\right]^{-1} \tag{2.3}$$

The cost function to minimise was just the sum of equations (2.2) and (2.3):

$$c.f.(L) = 2\frac{R\ Longitudinal}{R\ Transversal}(L) + \frac{Node\ Length}{Diffusion\ Length}(L). \tag{2.4}$$

As it is possible to see from Fig. 2.4, the final chosen value of 5 mm for the Node Length was around the minimum of the selected cost function. In this work we decided to use the node size obtained with $n = 9$ (that is the minimum diffusion length possible in the micro device) for each node in the device, but considering different node lengths within the micro device related to n coming out from each node is also possible (21).

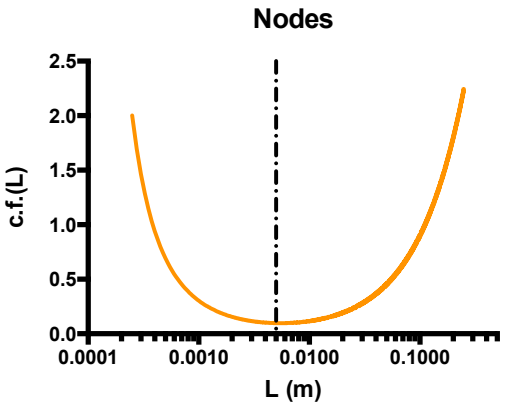

Figure 2.4: View of the cost function value related to node length L. The dash-dot line is related to the chosen Node length value of 5 mm.

2.3 Concentration gradient robustness evaluation via CFD

A rigorous analysis of flow through such networks can be achieved using computational fluid dynamic (CFD) analysis. Parametric sweeps of either boundary conditions (i.e. inlets flow speed) or fluid properties could be performed in order to gain insight on microdevice behaviour. CFD simulations of the microfluidic concentration gradient generator were performed in ANSYS Fluent, in order to evaluate the inlet flow conditions that allow the device to form a proper concentration gradient in the culture chamber. The effect of different Peclet number, obtained by varying diluted specie diffusion coefficient and average chamber flow rate from 1/100 to 100 times the nominal value, was evaluated. Also the effect on chamber concentration profile shape by varying the inlets flow ratio (from 1/10 to 10 times the nominal value at a fixed Peclet number) was investigated. The goal of the study was to find an effective working window for the microdevice.

2.3.1 Peclet Number Sweep

In using the Campbell et. al. (21) algorithm we have to set nominal inlets average velocity (v_{01},v_{02}) or pressure, depending on the favoured control strategy. In particular it was decided to consider the nominal velocity average $U = (v_{01} + v_{02})/2$ as velocity control variable.The nominal velocity U_0 was set to $9.5 \cdot 10^{-4} m/s$. Meanwhile we have to choose a nominal diffusion coefficient $D_0 = 5 \cdot 10^{-10} m^2/s$, in order to choose the proper lengths for serpentine micro channels that allows the complete mixing of the streams. The question we analysed in this section is: what happens if we vary the conditions from the nominal ones, so by changing the flow average speed or the diffusion coefficient D (always maintaining fixed the v_{01}/v_{02} ratio to k_0=3.75). In particular we

decided to sweep U/U_0 and D/D_0 in the interval 10^{-2}-10^{2}. Pe number, defined previously in eq. (1.8), which is the parameter controlling the mixing length, is dependent on both average velocity and diffusion coefficient, so for each swept U/U_0 there are n related D/D_0, leading to a Pe 2D map (Fig. 2.5). Obviously we had to make a discrete sampling on U and D, so we choose for U/U_0 and D/D_0 the values of 1/100, 1/10, 1/5, 1/2, 1, 2, 5, 10, 100. The map in Fig. 2.5 is obtained by contour plot of Pe corresponding to these values.

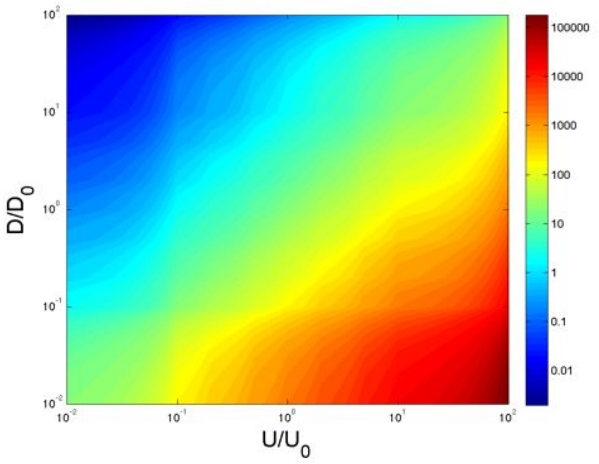

Figure 2.5: Contour plot of Peclet Map. U_0 and D_0 are the nominal average inlet velocity and nominal diffusion coefficient, respectively. U and D are the swept average inlet velocity and diffusion coefficient.

2.3.2 Inlet Ratio Sweep

In this section we decided to perform an analysis complementary to section above: we maintained Pe number to nominal value (950, with U and D either to nominal value), but we varied the inlet ratio v_{01}/v_{02} from the nominal one.

In nominal conditions, by following the algorithm of Campbell et al. (21), $k_0 = v_{01}/v_{02} = 3.75$. By maintaining constant the flow rate coming from the inlets and varying the ratio k_0 for a constant k we have that:

$$\begin{cases} v_1 + v_2 = U_0 \\ v_1 - kk_0v_2 = 0 \end{cases} \tag{2.5}$$

from which we obtain:

$$AIC = 2k + n\ln(RSS/n) \tag{2.6}$$

$$\begin{cases} v_1 = U_0 \dfrac{1}{k_0k + 1} \\ v_2 = U_0 \dfrac{k_0k}{k_0k + 1} \end{cases} \tag{2.7}$$

We chose to analyse the variations in profiles for k ranging between 10^{-1}-10, with in particular k= 10,5,2,1.5,1.2,1.1, 1, 1/1.1, 1/1.2, 1/1.5, 1/2, 1/5, 1/10. The chosen velocities are summarised in Fig. 2.6.

2.3.3 Mesh and Numerical Resolution

Simulations were performed, as in previous chapter, with FLUENT fluid dynamics package of Ansys. The grid consisted of cubic elements with $25\mu m$ edge, corresponding, approximately, to the viscosity-dependent typical dimension $\mu/\rho U$. This leads to a mesh of 80 elements in each cross section of the mixing channel, thus in agreement with the recommendation by Hussong (25), regarding how to accurately describe the velocity fields. A second order discretisation scheme was used to solve all the governing equations; using higher-order scheme did not lead to any significant change. Simulations were typically considered converging when the normalised residuals for velocities were stationary with iterations and

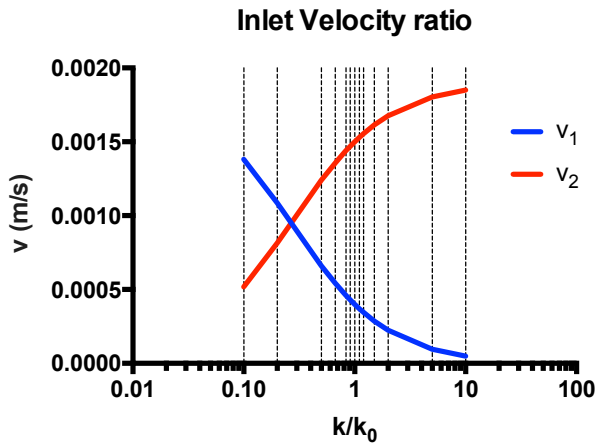

Figure 2.6: View of v_1 and v_2 in function of k. The values k assumes are :10,5,2,1.5,1.2,1.1, 1, 1/1.1, 1/1.2, 1/1.5, 1/2, 1/5, 1/10, and are shown by black dashed lines.

fell below 10^{-6}.The steadiness of the solution with iterations was also assessed by checking the velocity and concentration field in the outlet section of the mixing channels at different iterations. As mentioned above, here the concentration field is discretised using the same mesh size as the velocity field. Also in this case boundary conditions consisted of no-slip velocity and no-mass-flux at the channel walls, a constant ambient pressure at the chamber outlet, while at the two inlets a plug flow with velocities v_{01} and v_{02}, calculated with the previously proposed algorithm, were imposed. Concentration profiles at the chamber outlet were compared.

2.3.4 Results

2.3.4.1 Peclet Number Sweep

Concentration profiles taken at the chamber outlet obtained with different U and D values were compared to desired profile. An RMS error between desired and simulated profile was used as discriminator. Figure 2.8 shows the 2D map of Root Means Squared (RMS) errors obtained at different U and D values. The diagonal lines are at constant Pe, as can be seen in the figure. If we plot the RMS values in function of just the Pe number we obtain Figure 2.7, which shows that, for high Pe, the RMS is almost negligible, giving a "Working Zone" for the device (green highlighted zone). So if the Pe is in the "green zone", which corresponds to the "blue zone" of the 2D map, the device is generating properly the concentration gradient. The Pe number range that falls in the working zone is quite wide, so the device is robust in this sense, because there are no strict requirements for flow speed (so there is not the need of a very precise pump) and species diffusion (meaning that also there is not the need of measuring/estimating the specie diffusion coefficient with high grade of precision), if the chamber Pe is $>$ 10.

2.3.4.2 Inlet Ratio Sweep

The inlet ratio sweep instead shows that the device sensitivity to k parameter, which is the ratio between the inlets velocities, is quite pronounced. In fact Figure 2.9 shows that the RMS error reach low values only in a small interval, specifically $k \in [0.9; 1.5]$, so the effective working window is narrower than previous case, implying that the inlets velocity ratio is a critical parameter to take into account. However knowing the effective working range can give useful hints also in this case. In particular it makes possible to choose a peristaltic pump

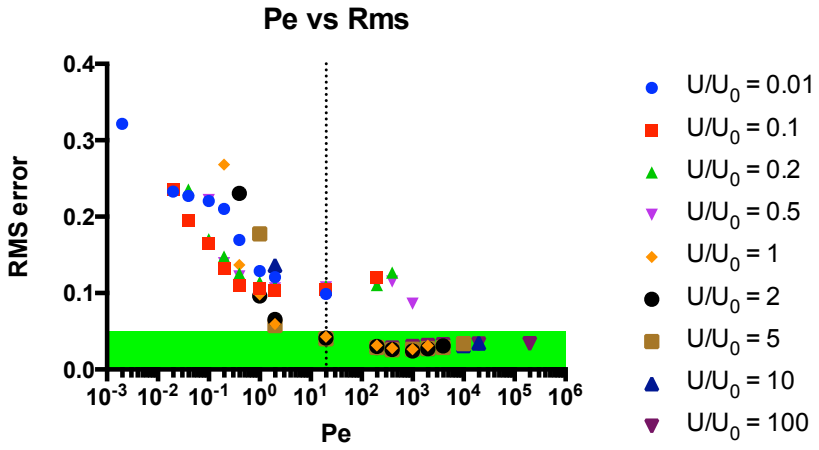

Figure 2.7: View of RMS error between desired and simulated concentration profile. The "green zone" is the effective working zone of the device.The Pe number range that falls in the working zone is quite wide, so the device could be considered robust to chamber Pe variations (if Pe >10).

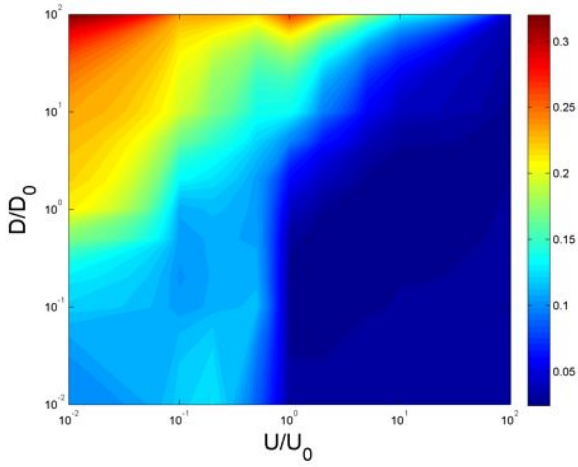

Figure 2.8: View of RMS error map between desired and simulated concentration profile. The "blue zone" is the effective working zone of the device.The Pe number range that falls in the working zone is quite wide, so the device could be considered robust to chamber Pe variations (if Pe >10).

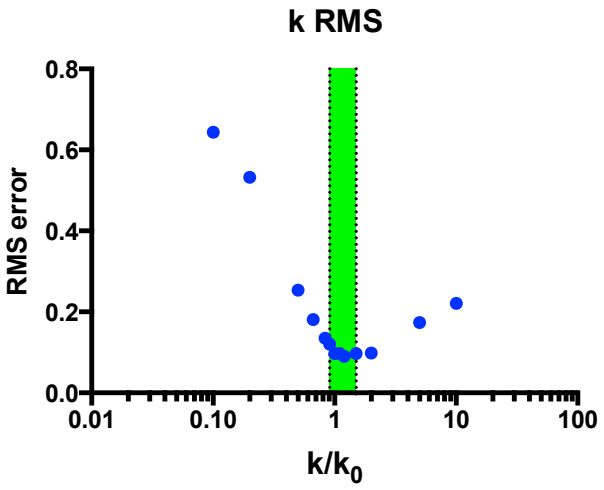

Figure 2.9: View of RMS error map between desired and simulated concentration profile. As it is possible to see here the effective working window is narrower than previous case. In particular only the interval $k \in [0.9; 1.5]$ is suitable for microdevice proper working.

instead of syringe pump, if the ratio between the tube diameters falls within the k working range, reducing the cost of the lab equipment needed for the device to work and letting the device to be perfused longer thanks to peristaltic pump nature.

2.4 Making Hydrophilic PDMS

The outstanding characteristics of polydimethylsiloxane (PDMS) owe its extensive use to the fact that it is a base material for the microfluidic devices manufacturers. In spite of favorable physical and chemical properties, the hydrophobic surface of PDMS is a handicap when pumping aqueous solutions through mi-

crochannels using only capillary forces. There are several techniques to achieve a hydrophilic behaviour of PDMS, but most of them face the problem of hydrophobic recovery after a short period of time while most commercial microdevices require long storage and distribution times. The use of surfactant-added PDMS provides a method to overcome hydrophobicity and to control the hydrophobic recovery over a long period of time. Two non-ionic surfactants, Brij 35 and Tween 20, were added in various mass percentages (1%, 2%, 3%) to PDMS (Sylgard 184). Water contact angle measurements were taken in order to characterise the hydrophilic behaviour of the modified PDMS. An exponential decay model was used for characterising the contact angle behaviour over time. Also microchannels with different width (from 50 to 400 μm) were realised with the modified PDMS. Measurements of capillary-driven flow speed for each channel size were taken and compared.

2.4.1 Contact angle characterisation

Brij 35 is a solid compound that is soluble in water, ethanol and methanol. In order to mix it with the PDMS prepolymer it had to be diluted in water at 30% w/v. Tween 20 instead at environment temperature is a viscous liquid, so it can directly be added to PDMS prepolymer. Five kind of PDMS samples with added surfactant were prepared with the following protocol:

1. PDMS monomer and cross linking agent were mixed at 10:1 w/w ratio, following the kit Sylgard 184 instructions;
2. Surfactant was added to the mixture, in order to achieve 1%, 2% or 3% w/w ratio between monomer and surfactant solution;
3. The mixture was then stirred and let to degas for at least two hours in vacuum. The time is long because the surfactant has the tendency to trap

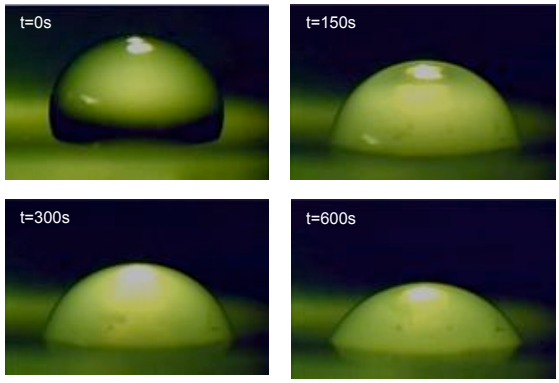

Figure 2.10: View of contact angle of water on PDMS/Brij 3% over time

air inside the mixture;

4. The polymer is then cast into the mould (a standard Petri dish) and let to cure at 60 degrees overnight. ...

For each kind of modified PDMS, water contact angle was measured with a custom analysis system. On each of n=6 samples for each kind of PDMS was deposed a 5 μL drop of deionised water. With the instrument camera were taken movies of the contact angle varying during 10 minutes time (Figure 2.10), that had been analysed with the Contact Angle Toolbox of Fiji.

The dynamic contact angle for each surfactant/PDMS ratio during time was taken as the point wise average of the n=6 samples. The contact angle data were then fitted with an exponential model, in order to evaluate the characteristic time of contact angle drop. Literature showed that usually the contact angle shows a mono exponential or bi-exponential decay (35). By using Akaike Information Criterion (AIC) (36), the mono-exponential model was proven to be the best for fitting the data. AIC is a tool for choosing the best model. Given a likelihood function L to maximize in the fitting, the criteria considers

the number of parameters k and the experimental data n.

$$AIC = 2k - 2n\log(L) \tag{2.8}$$

In general terms given a set of candidate models for a data set, the preferred model is the one with the minimum AIC value. Thus these criterions not only reward goodness of fit, but also include a penalty that is an increasing function of the number of estimated parameters. This penalty discourages overfitting, so we used these criterions to justify the presence of a greater number of parameters in the new model. By taking a likelihood function based on residual sum of squared (RSS), the formula above becomes:

$$AIC = 2k - 2n\log(RSS/n) RSS = \sum_{i=1}^{n} (y_i - x_i)^2 \tag{2.9}$$

where y_i is the fitting curve and x_i is the experimental data point. AIC values obtained from mono exponential model were three times lower than the bi-exponential one, so the former was chosen.

2.4.1.1 Results

Despite Brij 35 and Tween 20 have a different chemical structure, contact angle measurements shows in both cases an increased hydrophilicity in PDMS. Figure 2.11 and **??** show that the contact angle drop is proportional, as could be expected, to surfactant concentration. In particular the contact angle reach a minimum of 47 degrees for 3% Brij35, 72 ° for 2% Brij35, and 76 ° 1% Brij 35. The Tween20 shows contact angle of 84 ° in 1% case and 63 ° for 2% case. The Tween 20 3% case is not analysed because in that concentration the surfactant acted as PDMS polymerisation inhibitor. However the surfactant caused a transparency loss within the PDMS (Figure 2.13). The Brij 35 treated PDMS shows more transparency than the Tween 20 counterpart, so it has to be preferred for

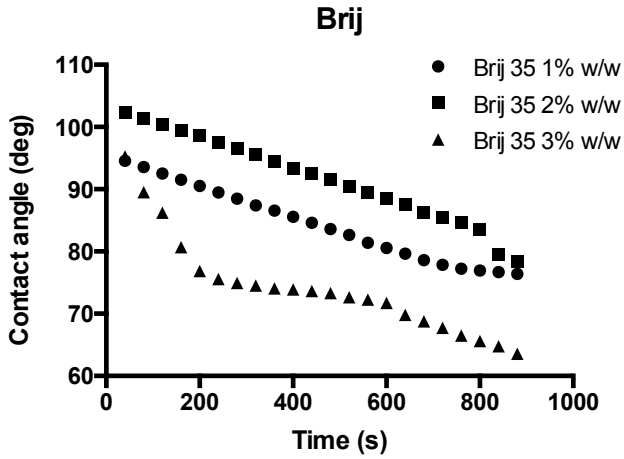

Figure 2.11: Representation of Contact angle measurements in PDMS/Brij 35 at various concentrations.

microfluidic applications, where a visual inspection is fundamental. Brij 35 also shows less settling time than Tween 20 at high concentrations, so it is more suitable for driving the flow with capillary interactions (Figure 2.14). Even if the characteristic time is on the order of hours, the hydrophilic borderline is crossed in few minutes. In the end Brij 35 resulted to perform better than Tween 20 in any aspect, so it was chosen as surfactant for making the device. Brij 35/PDMS resulted to have minor characteristic time (3200s for Brij 35 vs 4900s for Tween 20).

2.4.2 Capillary speed measurement

With soft-lithography techniques was built a structures with 8 micro channels of different diameters, (50, 100, 150, 200, 250, 300, 350 and 400 μm, respectively) and height 200 μm, as depicted in Figure 2.16.

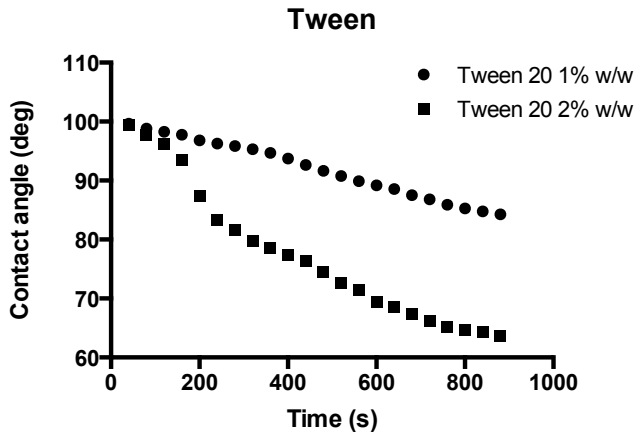

Figure 2.12: Representation of Contact angle measurements in PDMS/Tween 20 at various concentrations.

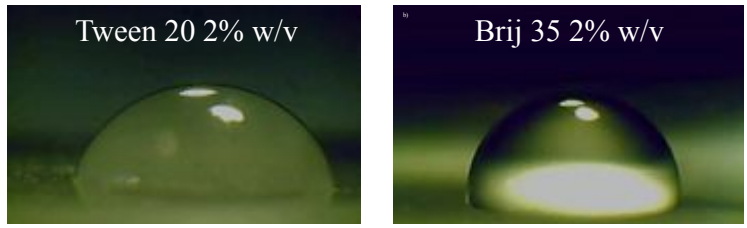

Figure 2.13: View of treated PDMS transparency loss, tolerable only in PDMS/Brij 35 case.

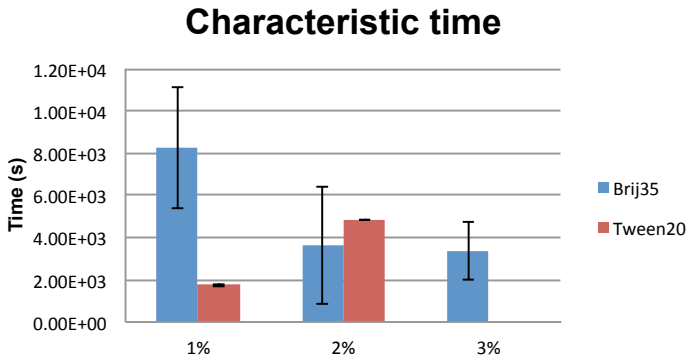

Figure 2.14: View of characteristic contact angle drop times. Brij35 shows also in this case better performances.

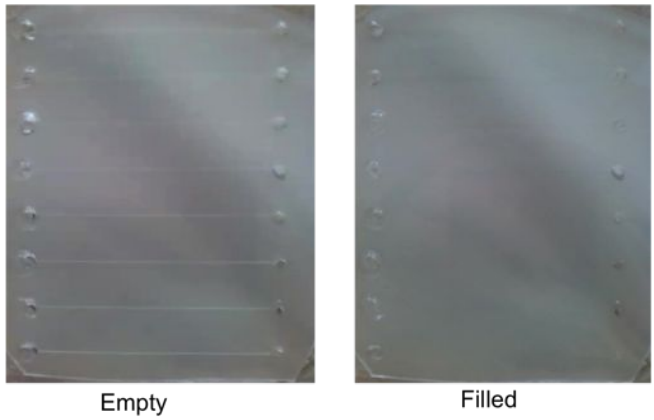

Figure 2.15: View of made micro channels with different diameters, in filled and not filled state.

Brij 35 3%-PDMS was cast over the silicon master, let to degas for 2 hours and then cured for 8 hours at 70 °. After detaching the polymer from the master holes were punched in correspondence of each channel inlet and outlet. The 3% concentration was chosen because it showed the best hydrophilic performance in lower settling time and minimum angle reached. The polymer with enclosed micro channels was then placed over a glass petri dish so sealing the micro channels, and a drop of deionised water was placed at the micro channels inlets. A movie of the droplet moving into the micro channel thanks to capillary interaction (yes, now the PDMS is removing the air and sucking water!!), was taken. The velocity was measured as $\Delta x/\Delta t$ where x is the position of the micro channel liquid front at a time t. Six movies for each channel were taken and averaged for having a reliable average velocity measure.

2.4.2.1 Results

As expected the flow speed is the highest in the lowest section micro channel, slightly decreasing as the micro channel section rises (Figure 2.16). The small velocity, that increases in largest section capillaries is due to the capillary pressure/hydraulic resistance ratio. In fact, while the capillary pressure is less than previous case, also the hydraulic resistance (which has a growth law proportional to the square of channel height) is less, leading to a biggest ratio than previous cases, that results in higher flow speed.

2.5 Conclusions

Root Mean Square (RMS) differences between expected and simulated behaviour were analysed. Peclet number was shown to regulate the device performances. In particular with higher Pe the concentration profile is shown to be closer to

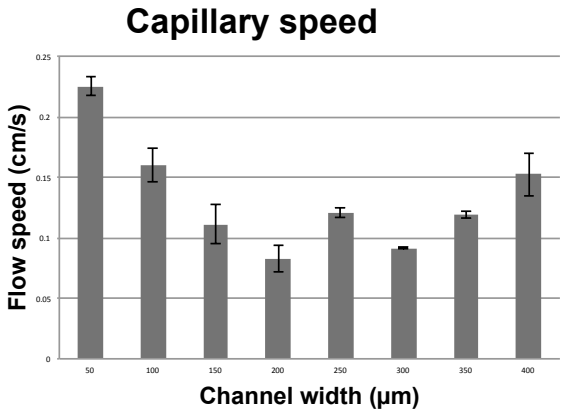

Figure 2.16: View of average capillary speed in function of duct diameter.

desired one. The working range however is wide. The device was proven to be more sensitive to inlets flow ratio, which shows a narrow effective working range instead, but still compatible with common pump requirements. PDMS modified with Brij 35 resulted to have better features than the one modified with Tween 20. In particular Brij 35/PDMS resulted to have lesser contact angle (down to 40 ° in the long run, instead of 60 ° related to Tween 20/PDMS), minor characteristic time (3200s for Brij 35 vs 4900s for Tween 20) and better transparency of its Tween 20 counterpart. Capillary velocity was measured in microchannels made with PDMS modified with 3% Brij 35, and the flow was resulted to be successfully capillary-driven, so eliminating the bubbles in the micro channels autonomously, without the need of pressurising the system. However while the new layout was proven to be easier to use with cells, the device was still not usable for cell culturing, in fact interactions of hydrophilic PDMS with the surfactants inside the medium culture led into pouring from inlets and micro channels network. So the cell culturing problem was still unresolved.

Chapter 3

Cell Perfusion within a 2D concentration gradient bioreactor

In this chapter, cell experiments using a 2D concentration gradient maker are described. BJ skin fibroblasts (foreskin fibroblasts) were seeded on an 18 mm x 18 mm glass coverslip, which was inserted in the microdevice culture chamber. The whole device was made in Plexiglas by laser micromachining (microchannels width of 250 μm), and sealed with a nuts and bolts locking system. A thin PDMS layer was used as gasket. This solution was chosen in order to allow users to seed the cells in a glass slide with common culture techniques, and then place it in the gradient maker, starting the perfusion afterward. A 10^x shaped concentration H_2O_2 gradient [0;10^{-2}] mM was let to flow in the culture chamber for 3h. The percentage of live cells/total cells for each zone was evaluated by Live/Dead assay, in order to evaluate the effect of H_2O_2 on seeded cells. A dose-response curve was successfully extracted pharmacologically relevant pa-

rameters such as the concentration required to kill half the members of a tested population after a specified test duration, the so-called LC_50.

3.1 Introduction

Thermoplastic polymers are highly attractive substrate materials for microfluidic systems, with important benefits in the development of low cost disposable devices for a host of bioanalytical applications. They have also interesting features such as hydrophilicity, negligible small molecule adsorption, and negligible gas permeability (for avoiding uncontrolled bubble growth in microchannels). Laser micromachining is a promising method for making thermoplastic devices employing microchannels (37, 38, 39). It is a highly precise, fast and contactless alternative to classic machining. In this part a laser micro machined Plexiglas micro device was used, avoiding hydrophobicity and gas-permeation problems relative to the initially appealing PDMS. A thin PDMS layer was however used as gasket. The channel layout was the same as previous chapter, that was found to be robust and reliable, and also allowed users to seed the cells in a glass slide with common culture techniques. Cells will be then seeded in a glass slide and placed in the gradient maker, starting the perfusion experiment afterward. A 10^x shaped concentration H_2O_2 gradient $[0;10^{-2}]$ mM was let to flow in the culture chamber for 3h. H_2O_2 was chosen as toxicant due to its high lethality and fast action time, so a short time perfusion is enough for assessing its effects on cell cultures. The percentage of live cells/total cells for each zone was evaluated by Live/Dead assay, in order to evaluate the effect of H_2O_2 on seeded cells. A dose-response curve was successfully extracted and pharmacologically relevant parameters such as LC_50 (concentration required to kill half the members of a tested population after a specified test duration) measured.

3.2 Layout

The proposed layout was similar of the previous chapter one, as can be seen in Figure 3.1. In fact also this time there is a Plexiglas-PDMS-Plexiglas sandwich, but this time the micro channels are directly machined on the polymer, and the PDMS is a thin layer which acts just as gasket. A nuts and bolts locking system (Figure 3.2) was used to ensure the tightness of the sealing.

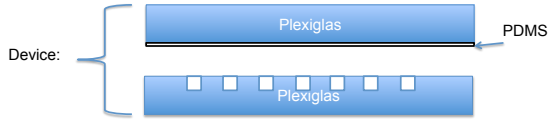

Figure 3.1: New layout of the GM. In this case micro channels are directly engraved into the PMMA bottom piece, and the PDMS is directly bonded with the top PMMA part.

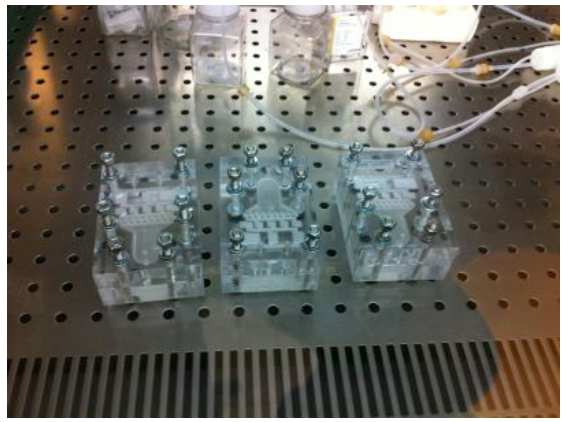

Figure 3.2: View of the assembled device. The six M6 nuts and bolts system ensured a very tight and uniform sealing pressure.

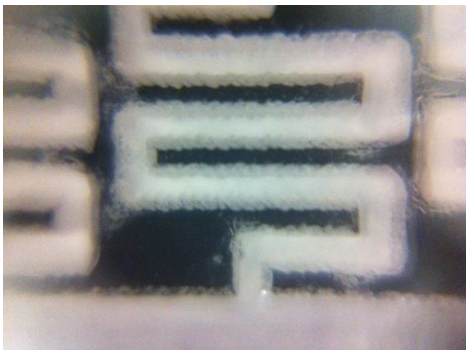

Figure 3.3: Magnification (15x) of a micro channel ablated by laser micro machining.

3.2.1 Laser Micromachining PMMA

In recent years, microfluidics has emerged as an advanced technology for analytical, biological, diagnostics and biomedical research. For the fabrication of microfluidic devices, polymers have become more and more important compared with conventional materials such as silicon and glass due to a number of advantages such as low cost, ease of fabrication and bulk material properties. A large number of polymer microfabrication technologies have been established. These technologies can be divided into two main groups: replication techniques (40), in which a master structure is replicated onto the polymer material, and the direct technique (41, 42), in which each single device is manufactured separately. For a small number of devices, replication methods such as hot embossing and injection moulding are not only complex but also expensive compared with a direct technique such as laser ablation. Laser micromachining is a promising method for making polymer devices employing microchannels. It is a highly precise, fast and contactless alternative to classic machining. A number of groups have investigated laser ablation of polymers (43, 44). Klank (37) and Snakenborg

(45) investigated the use of a commercial CO_2 laser system for the fabrication of polymethyl-methacrylate (PMMA) microfluidic systems. The laser ablation mechanism is a complex combination of photochemical and photothermal processes (43). This means that some chemical bonds of the substance are broken directly during the process of photon absorption while others are broken thermally by the released heat of those excited molecules that do not break up photochemically. Whenever the focused laser beam meets the workpiece surface, the temperature of the irradiated spot will rise so rapidly that the material will first melt and then decompose and vaporise, leaving a void in the workpiece (39). When the laser beam moves across the workpiece surface, it creates a pool of molten polymer in a spot where it impinges on the surface. The pool is driven away from the hot spot to all directions by the heated gas of the vaporising plastics, while most of the melted material re-solidify in the wake of the beam. In this manner, the moving laser beam is able to cut structures such as channels and wells into the workpiece. PMMA is fast burning thermoplastic. Below the glass transition temperature T_g, it remains in a glassy state. When the temperature increases beyond glass transition, it reaches a rubbery state. At higher temperatures between 170 10 °C and 210 10 °C, long-range deformations of chains of molecules occur. It is generally accepted that PMMA degrades thermally by chain depolymerisation, yielding MMA as the only decomposition product. This type of degradation is, in its general character, the reverse of polymerisation.

In this case a .DXF CAD file, generated with the previously described MATLAB library, defined the area to be laser ablated. Hence PMMA was fabricated at Plex Factory (Montopoli Val d'Arno, Pisa, Italy), and it is shown in Figure 3.5. The channel width was 250 μm, while the channel depth was 2.5 mm, so precipitating the hydraulic resistances in the network and shear stress in the

culture chamber (Figure 3.3). The flow chamber was not flat due to the nature of the laser machining, but in low *Re* the roughness effect on flow is negligible.

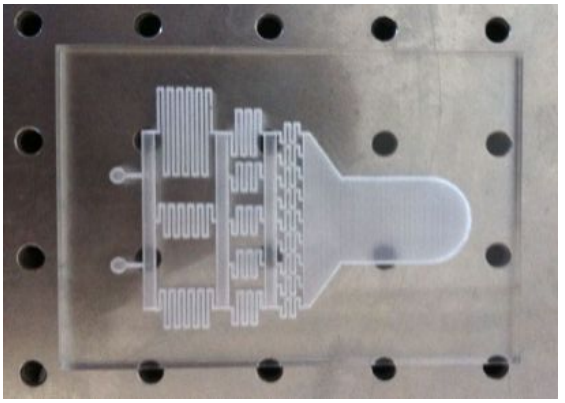

Figure 3.4: View of the laser ablated PMMA piece. The culture chamber bottom is not flat, but the effects on flow field are negligible due to the low *Re*.

3.2.2 Assembling

As depicted in Figure 3.1, the device is composed by a bottom PMMA piece where the micro channels are groved, a thin layer of PDMS (that in this case is Sylgard ®184), and a blank piece of PMMA. 6 mm aligned holes were made in the plexiglas, in which a nuts and bolts system connected the two polymeric parts (Figure 3.2). Also holes for inlets and outlet were made in the blank PMMA in correspondence of inlets and outlets of the bottom parts. The holes were 3.7 mm diameter, so a LUER lock (3.8 mm diameter) could fit and be mechanically locked into them, acting as non pouring device-to-world connection (Figure 4.26). The PDMS was deposed on this part as a thin layer with the aid of a spatula, left to degas and uniform for 2 hours, and finally cured overnight at 60 degrees, obtaining a PMMA part coated with PDMS. The PDMS was so thin to not clog

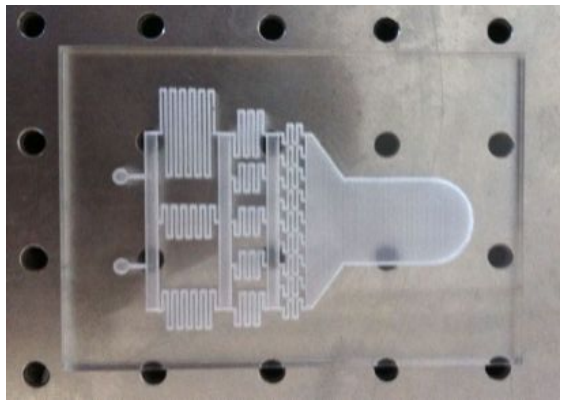

Figure 3.5: View of the laser ablated PMMA piece. The culture chamber bottom is not flat, but the effects on flow field are negligible due to the low Re.

the inlets/outlet channels and interfere with the nuts and bolts of the locking system. The device was perfused with water/dye in order to evaluate if the simulated profile was close to experimental one. As in Chapter 2 case, the two profiles are quite close (Figure 4.26). Also the device was filled with cell medium culture obtaining a complete filling without bubbles formation, sign that with this design also bubble formation problems were avoided (Figure 3.7)

3.2.3 Perfusion System

The perfusion system was composed by the Bioreactor, two bubble traps in series to the flow inlets (Figure 3.8), a multi channel peristaltic pump (Figure 3.9), and reservoirs (Figure 3.10). The bubble traps were needed in order to eliminate bubbles that nucleates spontaneously in the silicone tube during the peristaltic pumping, but also if they are only half-filled with culture medium they acts as hydraulic capacitor in parallel with the micro device, so acting as lowpass filter in order to smooth the pulsations of the peristaltic pump, allowing

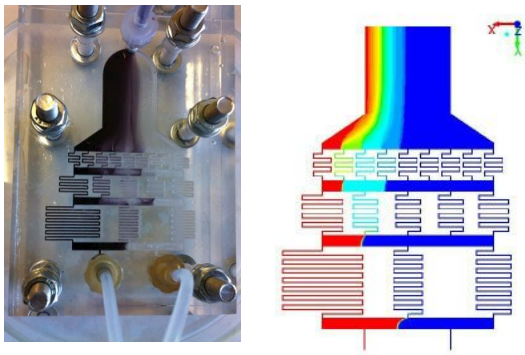

Figure 3.6: Comparison between simulated and experimental concentration profile. As in Chapter 2, there is a close matching between the two profiles.

cells in the culture chamber to experience continuous flow. The reservoirs have different size because the larger one contains blank culture medium, while the smaller one contains a 10^{-2} mM solution of H_2O_2 in medium culture. At the bigger reservoir was connected a 1 mm inner diameter silicone tube, while a 0.5 mm inner diameter silicone tube was connected to the other one. The inlet flows ratio k is the ratio between the tube inner sections. In this case $k = 4$, which falls in the robust working zone analysed in the previous chapter (nominal $k_0 = 3.75$. $k = 4$ is included in the interval $k_0 \cdot [0.9; 1.5]$), allowing to use a single peristaltic pump varying just the inlets diameter tubes.

3.3 Cell toxicity tests

BJ skin fibroblasts were seeded on an 18 mm x 18 mm glass coverslip, which was inserted in the microdevice culture chamber. This solution was chosen in order to allow users to seed the cells in a glass slide with common culture techniques, and then place it in the gradient maker, starting the perfusion afterward. A

Figure 3.7: Comparison between simulated and experimental concentration profile. As in Chapter 2, there is a close matching between the two profiles.

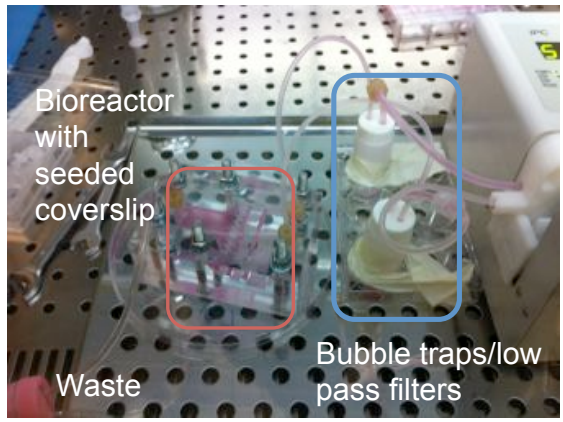

Figure 3.8: View of the Bioreactor and Bubble traps/lowpass filter parts.

10^x shaped concentration H_2O_2 gradient $[0;10^{-2}]$ mM was let to flow in the culture chamber for 3h. The percentage of live cells/total cells for each zone was evaluated by Live/Dead assay, in order to evaluate the effect of H_2O_2 on seeded cells.

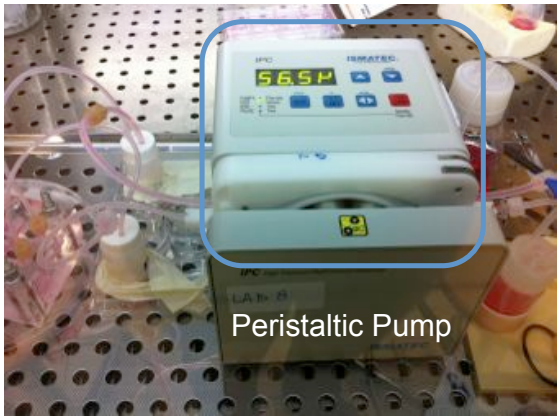

Figure 3.9: View of the peristaltic pump part.

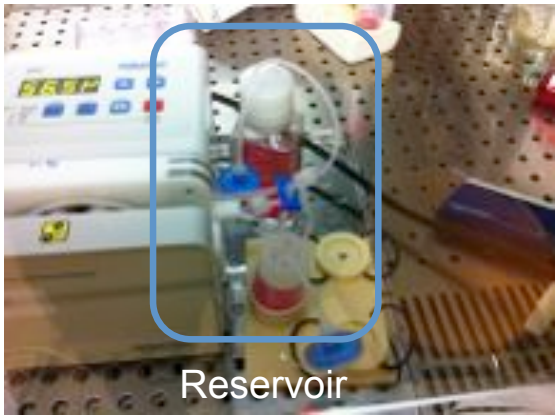

Figure 3.10: View of the two reservoirs. The larger one contains blank culture medium, while the smaller one contains a 10^{-2} mM solution of H_2O_2 in medium culture.

3.3.1 Cell tests

The cell test protocol was the following:

1. BJ skin fibroblasts were seeded on an 18 mm x 18 mm glass coverslip, which was placed into a 6-wells multi well plate.

2. Cells were left to arrive at complete confluence, because a uniform slide coverage was needed for detecting cells differences due to H_2O_2 concentration gradients.

3. At the beginning of the experiment the seeded coverslip was placed into the bioreactor;

4. The bioreactor was sealed with the nuts and bolts and then filled with medium culture.

5. A 3 h perfusion at 56 μL/min (in the lower section channel, the other one is 4 times the value) was then started, where a 10^x shaped concentration H_2O_2 gradient [0;10^{-2}] mM was let to flow in the culture chamber.

6. After 3 h perfusion the device was disassembled and the coverslip was processed with Live/Dead fluorescence assay kit.

7. Fluorescence images of the glass coverslips were then acquired in green and red channels. The coverslip was divided in 6 x 10 sections.

8. Images were processed and the local cell viability evaluated as % of Live cells (Green area) divided by Total cells (Green+Red area). ...

3.4 Results

The H_2O_2 gradient was shown to selectively kill the cells depending on H_2O_2 concentration, as depicted in Figure 3.11. A dose-response curve was then extrapolated from Live/Dead assay data . A 3h perfusion LC_{50} of 2 μM was successfully evaluated in our bioreactor with a one-shot experiment (Figure 3.12).

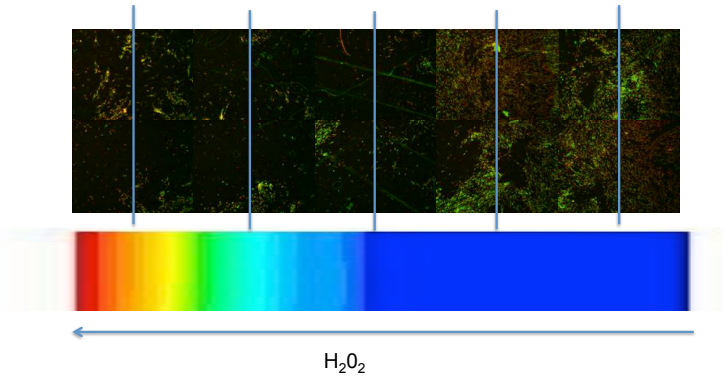

Figure 3.11: View of cells viability in function of coverslip position. As it is possible to note the percentage of live cells (green) depends directly on hydrogen peroxide concentration.

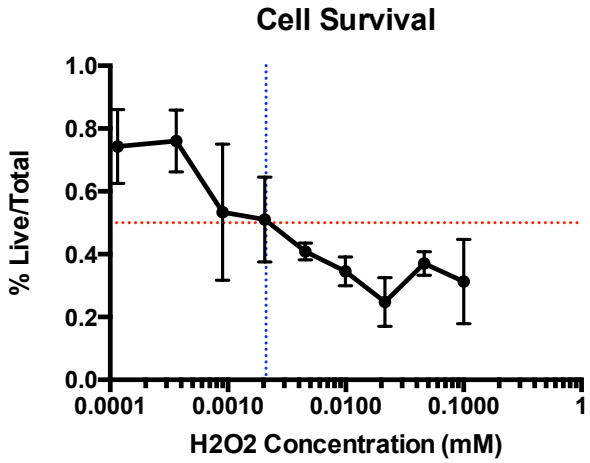

Figure 3.12: View of the extrapolated dose-response curve. An LC_{50} of 2 μM was successfully evaluated.

3.5 Conclusions

A dose-response curve was successfully extrapolated in a one-shot experiment, and a LC_{50} successfully evaluated. This kind of approach could be easily extended to other drug or pollutant in order to extract parameters of interests such as LC_{50}. The device could also have several applications in pharmacological testing and chemotaxis research. An intrinsic limit of the GM, with respect to static microwell plates, is that the cells state evaluation must be done always by imaging methods, differently from common colorimetric assays typical of multi well cells cultures.

Chapter 4

3D Concentration Gradient Maker

Soluble species spatial gradients are known for their morphogenic action during cell development, and they take place in a 3D environment. Also gradients of mechanical properties could lead cell migration and differentiation, and in the body also them are developed in 3D. During my thesis I bring the paradigms for building a concentration gradient from 2D to 3D. A novel 3D Concentration Gradient Maker, able to generate three-dimensional concentration gradients, was developed, which could be used scaffolds perfusion or stimulation with a 3D concentration gradient. The device also could be applied to build hydrogel matrixes with a 3D gradient of mechanical properties, as we demonstrated within the chapter. CFD analysis was used to develop the device; FEA and experimental studies were used to validate the 3D gradient of stiffness. The device and its application could have several applications in studying phenomena related to cell chemotaxis and mechanotaxis, but also on differentiation in simultaneous presence of gradients of both soluble chemical species and substrates stiffness.

4.1 Introduction

It has been proven that homeotic genes responsible for cellular specialisation (46, 47) are activated by specific temporal and spatial gradients of soluble compounds, the so-called morphogens (48, 49, 50). An example of morphogen is the Sonic Hedgehog Homolog (SHH), a protein of the Hedgehog family (present only in mammals). This protein plays a key role in the differentiation of tissues making up the limbs, hands, feet, and in the organization of the nervous system(51, 52, 53). For example, in the last decade has been found that SHH plays a fundamental role in the development of the central nervous system of mice. The concentration gradient of SHH enables the correct positioning of eyes at the sides of what would become the nasal cavity. Around the seventh day of embryonic life, a SHH gradient, that allows the cell growing around it to specialize and to organize, is released by cells of the notochord. The SHH plays the same role in the human embryo (54). Recent in vivo experiments performed on samples of mouse and zebra fish have shown that the presence of gradients of certain substances have a repulsive effect on the expansion of endothelial cells that make up the blood vessels. The cells placed on area of development stop growing in that direction when they feel an increasing concentration of Sema3A, Ephrin B2, Slit-2 and Netrin-1 (protein chemo-repulsive) (55). Other gradients, however, promote cell growth and therefore the expansion of vascular tissue in certain directions (56, 57). In this case the cells of the vascular tissue grow when they detect an increasing concentration of VEGF and Slit-2 (chemo-attractive protein)(58, 59). The Slit-2 assumes the role of chemical attractant or repulse depending on receptor, which binds it. If it is bonded to Robo-1 promotes growth, while if it is bonded to the Robo-4 exerts opposite action (58). These concentration changes are necessary for the development of vascular system and

ensure the correct presence of it throughout the human body and therefore the necessary support of nutrients at any tissue. It is therefore very interesting to be able to recreate those chemical gradients in order to mimic biological phenomena driven by them. Because human being and each its tissue is a complex three-dimensional structure, to fully understand the phenomena that act within it, it is necessary to reproduce the physiological signal in a 3D environment. Gradients of mechanical properties are also proven to influence cell migration, differentiation and activity (5, 60, 61). For example, a durotaxis i.e., migration guided by substrate rigidity, was discovered for fibroblasts on substrates with step-gradients in their mechanical compliance(62). As Engler and his group demonstrated, the most straightforward way to create substrates with continuous variations in mechanical compliance is to control the crosslinking density of the substrates (5). This can be achieved by tuning the monomer/crosslinker ratio during polymerization. Materials with gradients in crosslinker concentration that extend over several centimeters or millimeters could be generated easily using a gradient generator (63).In literature microfluidic devices were mainly developed to generate two dimensional (2D) concentration gradients, which are far too simple for mimicking a real physiological environment. The first 2D concentration gradient bioreactor has been developed by Whitesides in 2000 (1), but over the years many different 2D concentration gradient generators appeared (21, 22, 64). Whitesides and his followers however have always developed other variations of this bioreactor, but always preserving the two-dimensionality of the developed concentration gradient. For example there were developed microdevices capable of creating monotonic nonlinear shaped concentration gradients in the culture chamber(65), but neither of those allow creating a 3D soluble species gradient. Also the Institute of Biomedical Engineering of National University of Taiwan has developed another device, with a geometric structure different

from those before mentioned, in 2008 (66). This device however, while showing a different approach from Whitesides' one, was not either able to generate a three-dimensional concentration gradient. The gradient maker (GM) developed in this thesis preserves some characteristics of its 2D predecessors, such as: a microchannels network able to generate monotonic soluble species gradients, and a chamber where cells/tissues can be placed and stimulated by the chemical gradient. The flow regime in the GM chamber had to be steady and laminar, but with low Reynolds number, in order to maintain a stable concentration gradient. In these flow conditions fluid streams flow side-by-side, so the mixing is driven by species diffusion, with diffusion length proportional to Peclet number (typically $\gg 1$ in liquids), and convective mixing effects are typically neglected (67). This allows predicting and controlling the gradient shape with great accuracy. In this work we first developed and characterized our microfluidic device using Computational Fluid Dynamics (CFD) in order to select the optimal topology and flow rate. Then the device has been realised using 3D rapid prototyping techniques. Prototype performances have been tested on a hydrogel matrix used as tissue model, placed in the GM chamber. Two dye solutions have been used as "morphogens" in order to analyse the effective formation of a 3D concentration gradient not only in the GM chamber but also inside the "tissue". As discussed before, a GM can be used to fabricate a substrate with a gradient of mechanical properties: such technologies have only been very recently realised through the development of microfluidic networks, which one can easily generate solution and surface gradients (68). Here, thanks to our 3D GM, we developed a method for fabricating 3D gradients of mechanical properties in a hydrogel, which could be then perfused with a gradient of a soluble species. The 3D GM could have several applications in studying phenomena related to cell chemotaxis and durotaxis, but also on differentiation in simultaneous presence of gradients

of both soluble chemical species and substrates stiffness. The device could be used in two ways: generating 3D concentration gradients of multiple substances i.e. growth factors, in order to have differential growth within a scaffold, and generating 3D stiffness gradient for the same purpose, in order to promote differentiation and/or differential durotaxis. A 1-D gradient is usually not enough for those applications (69, 70).

4.2 Materials and Methods

4.2.1 Numerical simulations

As in the previous cases the design of 3D GM started with a CFD analysis. Its performances were evaluated by solving the following set of equations:

$$\nabla \cdot \mathbf{u} = 0 \tag{4.1}$$

$$\rho \mathbf{u} \cdot \nabla \mathbf{u} + \nabla p = \nabla \cdot [\mu(\nabla \mathbf{u} + \nabla \mathbf{u}^{+})] + \rho \mathbf{g}. \tag{4.2}$$

Here $\mathbf{u}$ denotes the velocity vector, ρ is the fluid density, p the pressure, μ the viscosity, $\mathbf{g}$ the gravity acceleration. In case the diffusion of a specie is involved, we have to add the advection-diffusion equation (4.3) to the governing equations:

$$\mathbf{u} \cdot \nabla \phi = D \nabla^2 \phi. \tag{4.3}$$

Also In this case we chose to treat the species diffusion as the mixing of two identical fluids, each one diffusing in the other with a diffusion coefficient D, as did in (23) and (24), instead of tracking the specie concentration. By imagining to add a small amount of contaminant, i.e. a dye, to one of the

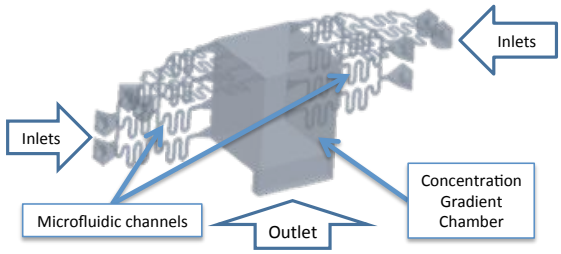

Figure 4.1: Concept of the 3D GM: view of wireframe and functional parts of the 3D GM.

fluids (which therefore continue to have the same physical properties) we have that ϕ indicates the (normalized) dye mass fraction. A three-layer "Christmas tree" network, similar to Whitesides' (1) solution and used in previous works (71, 72), was used in order to generate a linear concentration gradient through four trapezoidal inlets of the main GM chamber (the same one of Figure 4.1).

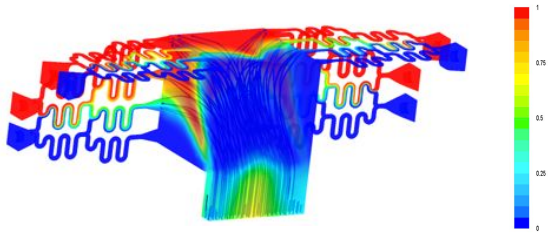

Figure 4.2: CFD simulation of the 3D GM, with normalised concentration pattern (in colour scale) and fluid streamlines (blue lines inside).

The structure consisted of a cubic chamber at the centre of the device (2.4 cm side length), in which there are the inputs of 4 mixing network perpendicularly placed. The output of the system is placed on the bottom of x-y plane. The mixing structure had 8 inputs and 16 outlets, which are inputs of GM chamber.

The GM chamber had only one output (Figure 4.1). The height of the mixing channels was set to 300 microns. All pair of input channels were set on the same average flow rate, while the chemical concentration are equal to C_{min} and C_{max} respectively. 3D gradient concentration is obtained thanks different solute concentrations in the x-y and z plane. Tetrahedral mesh was used with average size of 0.05 mm in the inlets and 0.5 mm in the mixing chamber. In this case the flow regime is highly laminar (Re= 7 in the inlets and Re= 30 in the mixing chamber). A commercial Computational Fluid Dynamic (CFD) code, Fluent 12.0 by Ansys Inc., was used to solve the three-dimensional equations of motion. However there is a limited range of flow rate that allows the formation of the concentration gradient. In fact, if flow rate is 20 times bigger or lower than the one reported in Table 1, for example, there is no marked gradient concentration profile in the GM chamber. Low flow rate enhances the effect of diffusive mixing, so the average length in order to have complete mixing due to diffusion in a 3D environment $UL^2/6D$ (73), where L is the characteristic chamber length and U is the average velocity, is comparable to chamber length. High flow rate instead lead to fast convective mixing in the main chamber. By increasing Re, in fact, fluid inertial effects on fluid streams become bigger, and there is a fast mixing of liquid streams due to convective effects. The mass exchange between fluid streams in this case becomes not mainly diffusion-driven. In water-based systems Pe is usually $\gg 1$, and so convective mixing, when occurs, largely predominates diffusive mixing.

4.2.2 3D GM fabrication

The mould and the frame of the bioreactor (Figure 4.6-4.10) were made in Acrylonitrile Butadiene Styrene (ABS) using a rapid prototyping system (Dimension Elite Stratasys, U.S.A.). The topology of mould was designed using Solidworks

software, exported in STL format and then imported in the control software of Stratasys machine. However we found that we could not directly build the microfluidics channels with that technique, due to the finite resolution of the 3D printer. In fact the natural roughness of the 3D printer (250 μm, Figure 4.9) was comparable to our micro channels size (300 μm), and it could lead to a not tight sealing and unwanted leakage from the microchannels.

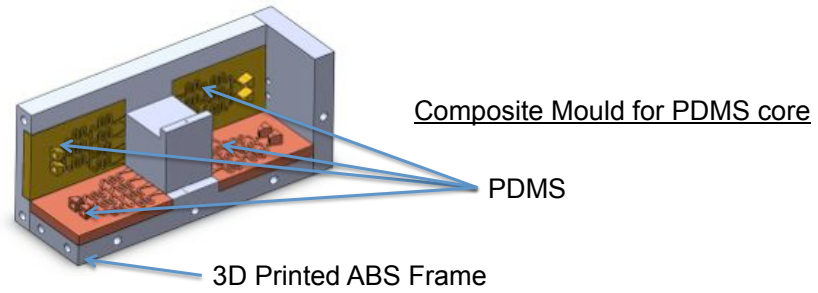

Figure 4.3: Concept of the 3D GM mould.

Figure 4.4: Realisation of SU-8 negative on the silicon wafer.

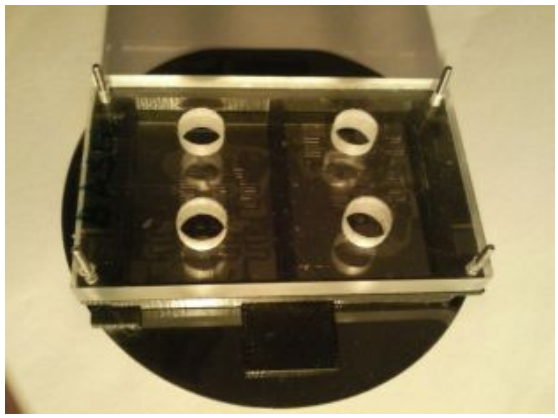

Figure 4.5: Plexiglas cover on silicon wafer, with holes for casting PDMS.

In order to avoid that, we made the microchannels mould by casting the PDMS (Sylgard 184, Dow Corning) onto a Silicon Wafer, where negative $300\mu m$ SU-8 structures of the microchannels were previously made (Figure 4.4). The negative photoresist SU-8 (MicroChem, Newton, MA) was spin-coated on the wafer baked to drive away the solvent and exposed to UV rays (CL-1000 Ultraviolet Crosslinker UVP) through a mask. The mask was created using CorelDraw 9.0 and printed on a transparency using a commercial Linotronic-Hercules 3300 dpi high-resolution line printer. The exposed photoresist was baked again to complete polymerization, and then developed (SU-8 developer, MicroChem) to dissolve un-irradiated material(74).

A 3D printed base plus a Plexiglas cover (Figure 4.5) was placed over the silicon wafers in order to act as a mould for the PDMS. The PDMS has been prepared mixing in weight ratio 10:1 monomer and catalyst. The PDMS solution was degassed under vacuum, casted in this mould, and then cured overnight at 60°. These parts were then placed in a 3D printed support as shown in Figure

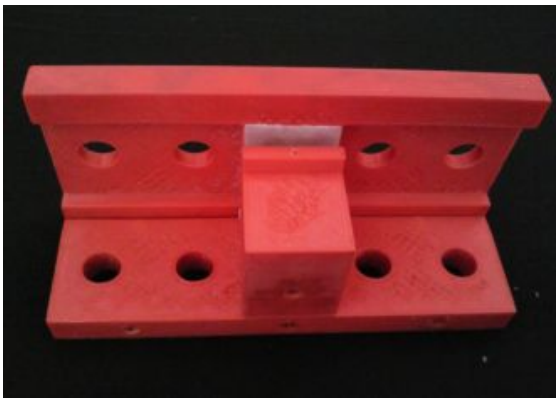

Figure 4.6: View of the 3D printed ABS support.

2e-f. GM main core was also made in PDMS, prepared as previously described, by casting the polymer in the previous described. Silicone tubes with an inner diameter of 2 mm and external diameter of 4 mm have been placed in the GM inlet positions, before casting process of PDMS in the mould began. After PDMS casting the mould has been cured for 7 hours at $70°C$.

With this procedure, the PDMS was not completely stuck to the PDMS positive parts of the mould, so we was able to extract the GM core from the mould without destroying both the mould and GM core. As it is possible to see in Figure 2g the GM surface obtained in this manner is very flat. To ensure a perfect sealing a purposely-developed locking system (Figure 4.10) has been designed and realised. It was composed of a plastic frame made of ABS and two 6 mm Plexiglas layers, in order to maintain a free visual path onto what happened inside the chamber and the microchannels. To ensure a tight sealing of all parts 8 plastic O-rings have been placed between the cylindrical inserts present on the external surfaces of the frame. The deformability of PDMS granted a tight sealing after compression. Figures 4.11-4.12 show the assembled reactor with

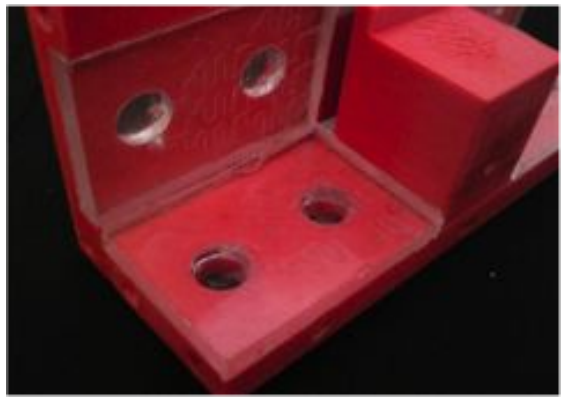

Figure 4.7: View of the 3D printed ABS support assembled with PDMS positives of microchannels.

the concentration gradient formation inside. Figure 4.14 also shows different concentration patterns that could be obtained in the GM. A set of peristaltic pumps (IPC, ISMATEC) was used for system perfusion. Here is shown a first gradient maker prototype, which was built with an 8 ml chamber in order to have polymer samples big enough to be tested mechanically. External gradient length depends on the application, varying from $\sim 150\mu m$ in cell development (75) to several mm for complex embryo development (i.e. Xenopus)(76). If there is the need for the gradient to develop in shorter length scales the system is easily down scalable.

4.2.3 PAAM Mechanical Characterization in function of BIS concentration

Polyacrylamide (PAAM) was chosen as a template hydrogel, due to the easiness in tuning its mechanical properties by just changing the acrylamide (AAM) to N,N'-Methylenebisacrylamide (BIS) ratio (monomer to crosslinker ratio). Com-

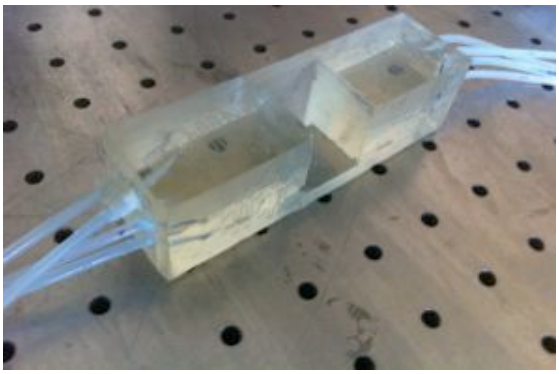

Figure 4.8: View of the de-molded PDMS core.

pressive mechanical tests were performed imposing different strain rates using the twin column ProLine Z005 testing machine (Zwick Roell) equipped with a 10 N (0.04 N sensitivity) load cell at room temperature. PAAM samples were tested partially immersed in water to preserve their hydration. Each test was performed using a starting configuration with the upper plate placed near the sample but not in contact, in similar manner as Tirella et al. did in their work (77), necessary to guarantee known initial conditions. Quasi-static stress-strain time series were collected compressing samples up to 10% (n = 3) deformation using two different strain rates (0.0125 min^{-1} and 0.0063 min^{-1}), in order to evaluate the Young modulus dependency from strain rate. The Young modulus of the tested sample was evaluated as the slope of first linear part of the Stress-Strain diagram. The strain rate was chose on the basis of previous works on hydrogels (78). The strain rate however was found to not influence on measured mechanical properties, as shown in Figure 4.17, so the tests were all performed at the max strain rate. A major challenge in testing PAAM was to obtain uniform samples. By just pouring the PAAM using a 24 well plate we observed the

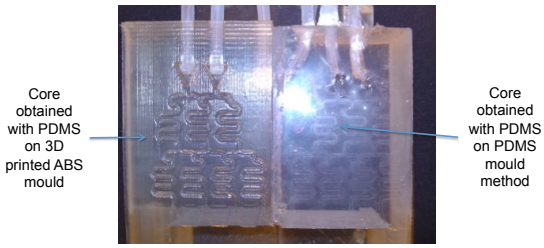

Figure 4.9: Differences between PDMS casted on a 3D printed mould (on left) and the one made with our mould (right). As it is possible to see the surface of the one on the right is very flat, so it avoids leakages;

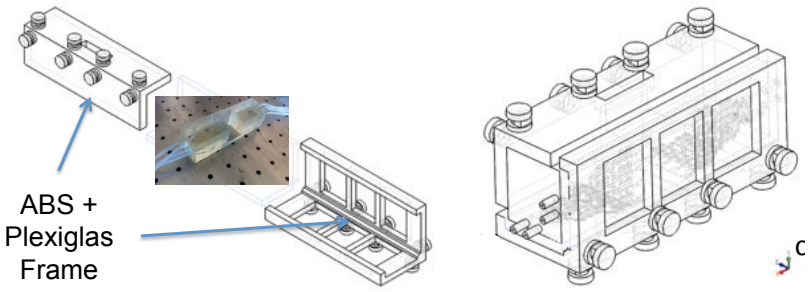

Figure 4.10: The 3D GM and its sealing system: concept and design.

formation of a meniscus on the sample, which was due to the combined effect of PAAM volume retirement during gelation and capillary forces.

The meniscus induced a non-reliable estimation on Young modulus, greatly increasing the standard deviation of the measure to 20% of the mean. In order to obtain reliable uniform samples we developed a custom-made mould, which is depicted in Figure 4.15. The mould was inspired to the 24 well plates, and it is made from three parts:

- A flat base, where just 3 mm holes for assembling with nuts and bolts were

Figure 4.11: Front view of the assembled device with a dye gradient developing inside.

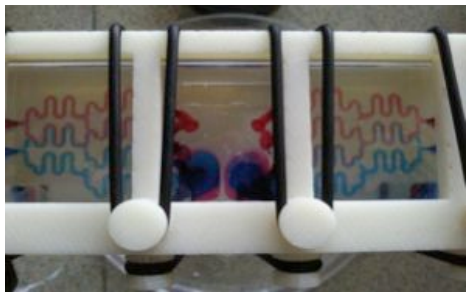

Figure 4.12: Top view of the assembled device with a dye gradient developing inside.

drilled.

- A middle part where, apart from assembling holes, 24 holes with a diameter of 13 mm were drilled, being the PAAM samples locations.
- A top part, identical to the previous one. This one will be detached just after the polymerization, to cut the top part of the sample.

After the PAAM polymerization and the detachment of the top part, we cut the top part of the samples that protruded from the middle part with a microtome sharp blade. In this way we obtained smooth surfaces also in the top part of

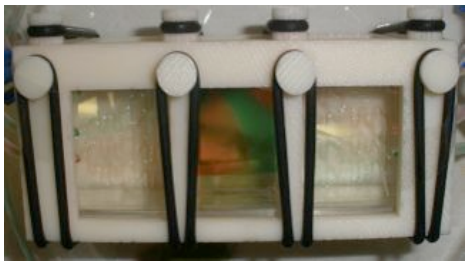

Figure 4.13: View of the assembled device with a steady developed gradient inside the chamber.

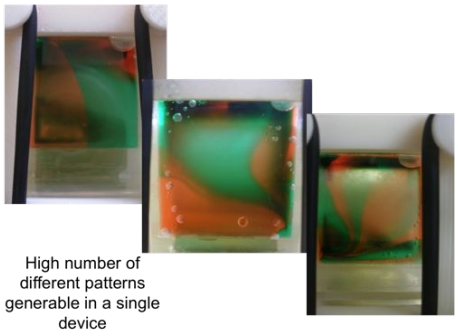

Figure 4.14: Examples of different gradients that we could develop by varying the flow rates and the distributions of dyes at the inlets.

our samples, and so eliminating the meniscus problem. In this way we obtained 13 mm x 8 mm uniform samples. PAAM gel was made by 8% (w/v) AAM, and from 0.04% up to 0.6% (w/v) BIS. As reported from datasheet (Bio-Rad, "Acrylamide Polymerization - A Practical Approach") 1/100 of Amonium Persulfate (AP, initiatior) and 1/1000 of Tetramethylethylenediamine (TEMED, catalyst) were added to the solution, in order to have the PAAM gelation. We decided to use free radical Polyacrylamide polymerization, because as reported from Biorad DataSheet "In chemical polymerization, visible gelation occurs in 15-20 min and

Figure 4.15: Mechanical characterisation of PAAM hydrogels in function of BIS concentration: view of the support used for uniform testing samples making;

polymerization is essentially complete in ~ 90 min. In photochemical polymerization, however, visible gelation takes 30-60 min and complete polymerization requires up to 8 hr". The 3D diffusion time $L^2/6D \sim 9h$ (73) becomes comparable to photopolymerization time in this case, while not in chemical polymerization case. Certainly photocrosslinking could be combined in future with the 3D concentration generator, in order to achieve more complex structures, but there is the need to choose carefully the initiator, the material to be crosslinked and the light source.

4.2.4 Realization and Characterization of a Hydrogel with a 3D Gradient of Mechanical Properties

An 8% w/v solution of AAM with respectively 0.04% w/v or 0.6% w/v of BIS flowed from the inlets, so that a BIS concentration gradient was set in the main chamber. Also the initiator AP was perfused from the inlets. When the flow steady state was reached an injection of TEMED from a hole on the top in the main chamber quickly polymerized the hydrogel into the main chamber.

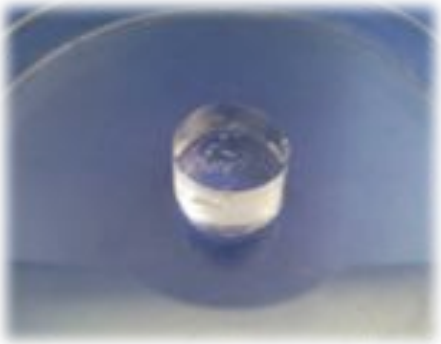

Figure 4.16: View of a 8% PAAM sample: its surfaces are both flat.

The 3D controlled distribution of BIS into the gradient chamber lead into the development of a gradient of mechanical properties into the polymerized hydrogel. Reaction time (first gelation observed, in minutes) is significantly higher than BIS diffusion time (several hours), so we can reasonably be sure that the distribution of BIS remains the same as the applied gradient, even during the polymerization. The diffusivity of BIS ($D \sim 10^{-9} m^2/s$) (79) is slightly higher than VEGF and SHH ($D \sim 1.5 \cdot 10^{-10} m^2/s$) (80).

However it is possible to tune the chamber flow rate in order to bring the chamber Pe to the same one as BIS, so the diffusion pattern remains the same. For these reasons BIS could be also used as a reliable diffusion model for a growth factor. The main "cube" was cut in 3 x 3 x 4 small samples, in order to have a good estimation of the distribution of the mechanical properties in the 3D environment. The "cube" was cut using the tools depicted in Figure 4.20-4.21, in order to assure a uniform and repeatable slicing. Briefly it was put in the bigger mould, and then cut into four slices with a histological sharp blade. Each one of the four slices was then placed in the second mould and then sliced

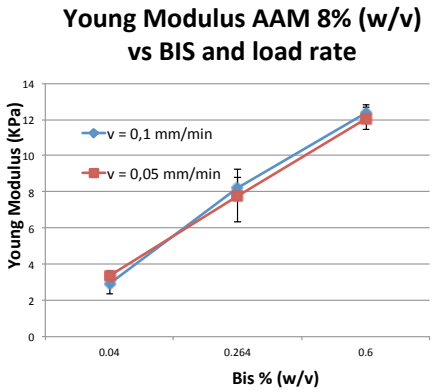

Figure 4.17: PAAM Young modulus vs. BIS concentration: as it is possible to see both the deformation velocity (corresponding to 0.0125 min^{-1} and 0.0063 min^{-1} strain rates respectively) do not affect the curve behaviour.

in 9 equal pieces. The choice of critical size was due to the detection limit of load cell. Each sample was subjected to a compression test using the previously described Zwick-Roell Z005 testing machine. The slope of first linear part of the Stress-Strain diagram evaluated the Young modulus of the tested sample, as above. Results are depicted in Figure 4.23.

4.2.5 Mechanical simulation of mechanical gradient structure

We faced the challenge about comparing experimental vs. simulated data. Classical fluid dynamics investigation tools such as Laser Induced Fluorescence (81) or 3D Laser Doppler Anemometry (82) could only evaluate the fluid behaviour in the inner device. We would like to have a direct comparison between the measured Young Moduli of the sliced cube parts and the simulated concentration profile into the bioreactor, using the Finite Element Analysis (FEA) In order to

Figure 4.18: Example of catalyst infusion into the main chamber using a yellow dye.

Figure 4.19: The PAAM "cube": view of the polymerised PAAM cube inside the GM;

do this, we first performed the fluid and mass transfer simulation with Ansys FLUENT, as explained above.

We then exported the final BIS concentration profile, by taking into account the spatial node position and value. This concentration profile was "sliced" in 3 x 3 x 4 parts, matching the experimental slicing of the PAAM cube. This concentration profile was then transformed in Young Modulus profile by using the inverse function of measured Young Modulus versus BIS (Figure 4.24), and imported in COMSOL Multiphysics as the point-wise Elastic Modulus of the sample. The mesh size of the 250k tetrahedral elements was 0.3 mm. Each

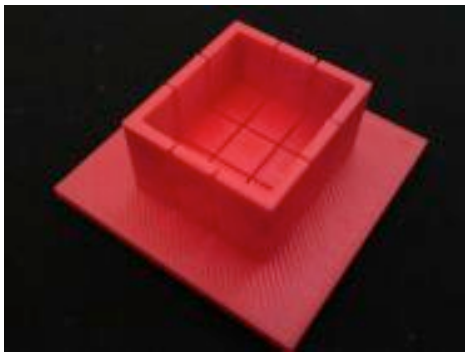

Figure 4.20: View of the first slicing tool: the blade passes between the spaces in the plastic, slicing the cube in 4 pieces.

cubic sample was subjected to 1% compression in the same direction of the experimental slices deformation, by assuming elastic behaviour (evidenced in stress-strain experimental data). The boundary conditions of the sample were a fixed constraint on the bottom face of the sample, while the 1% compression was imposed on the opposite face. We then evaluated the reaction forces in the top boundary by integrating the point-wise force contribution, as the transducer does in the real experiment. The simulated Young modulus was calculated by the well-known formula $E = F/A\epsilon$ where F is the calculated reaction force; A is the nominal undeformed sample section, and $\epsilon = 0.01$, the imposed deformation. The elastic moduli estimated with FEA were then compared with experimental ones. Results are summarised in Figure 4.26.

4.3 Results

The objectives of the presented work is to fabricate and characterise a 3D GM, with a design driven by CFD simulation and whose application can span from

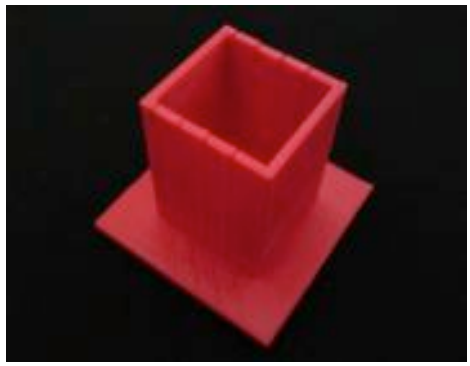

Figure 4.21: View of the second slicing tool: the samples cut before are split in 9 parts.

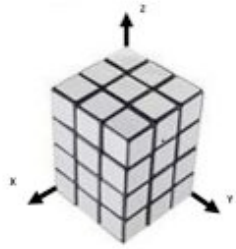

Figure 4.22: View of conceptual cube slicing in 9 x 4 = 36 parts.

the generation of 3D morphogen gradient to fabrication of 3D graded materials. For the fabrication of matrix with a gradient on mechanical properties a series of preliminary steps have been described in the materials and methods section. The results of that demonstrate the accomplished tasks are provided in this section, in which the comparison of FEA and experimental results is performed. The results of the mechanical testing are shown in Figure 4.23. As it is possible to see there is a gradient of mechanical properties developed in 3D. There is a

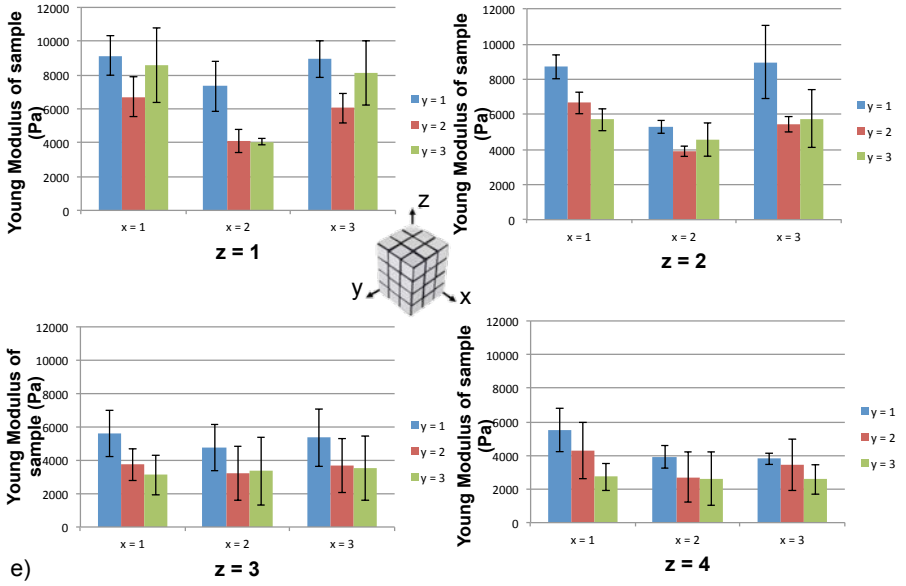

Figure 4.23: Experimental measurements of stiffness distribution within the cube. It is possible to see a stiffness gradient in both z and y directions.

decrease in Young Modulus from z=1 to z=4, and from y=1 to y=3, following the 3D concentration pattern of the flow. Figure 4.26 shows the comparison between theoretical mechanical properties distribution and experimental ones. As it is possible to see the experimental and simulated values are quite close in the upper part of the GM, with an RMS of $\sim 2.5kPa$, while the lower part shows larger discrepancies. The differences in the upper part (near the microchannels outlet) could be due to the peristaltic pump that was used as supply. In fact during pulsed flow the fluid streams reach the GM chamber with some delays, and it could bring unexpected mixing behaviour within the microchannels networks. Literature for example demonstrated that pulsed flow could enhance the

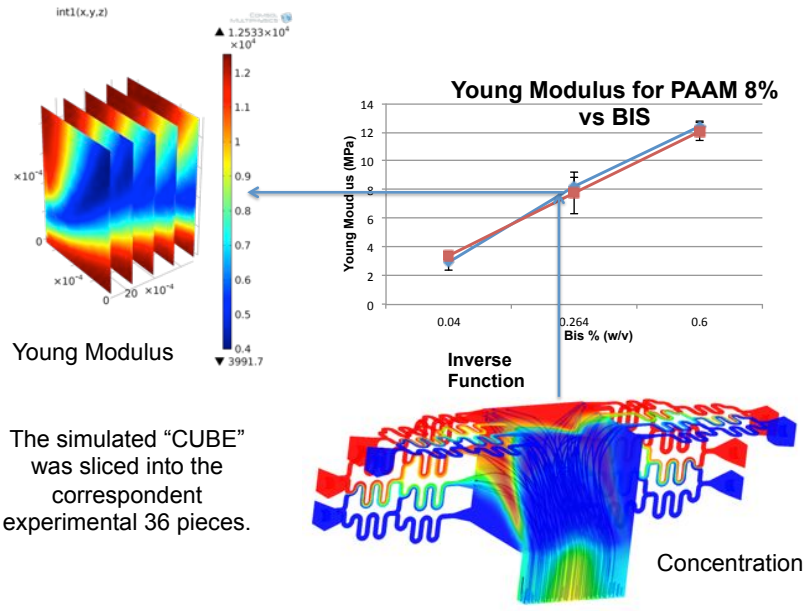

Figure 4.24: View of the technique for simulating structure with a 3D Young modulus gradient. An inverse function is applied mapping the concentrations into Young modulus. A compression test simulation will be subsequently performed on the structure

local mixing in T-shaped microfluidic branches (83). Those structures represent the mixing sites of our microchannels network (23), so the simulated mixing features could be slightly different from the experimental ones. The differences in the lower part however are quite large. This could be probably due to the boundary effects near the outlet, which cause unexpected flow distortions due to the dramatic decrease of flow speed.

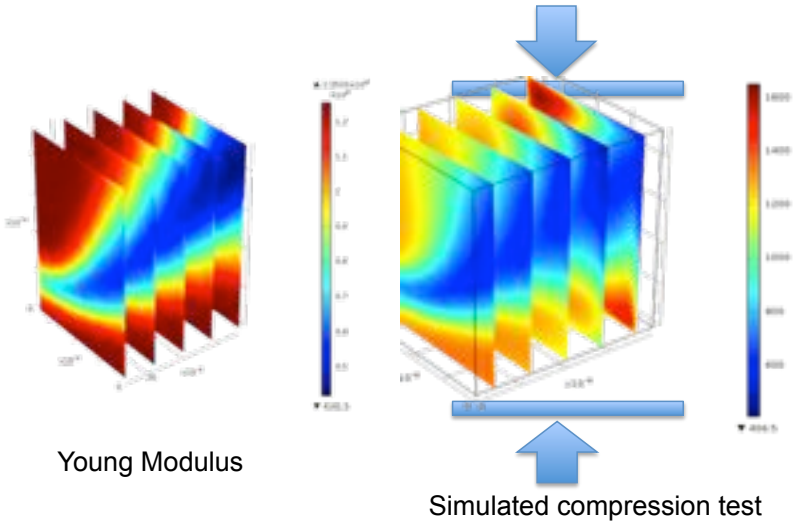

Figure 4.25: FEA Simulation of sample stiffness. View of Young modulus distribution (Pa) in a sliced part (x = 4, y=2; z=2), and its relative Von Mises Stress (Pa) after the compression test simulation ($\epsilon = 1\%$).

4.4 Conclusion

We presented a new generation bioreactor used to fabricate hydrogel matrixes with a 3D gradient of stiffness. Although there are some discrepancies between theoretical and experimental results, on which future robustness analysis will be performed, this bioreactor could also be used for perfusion of 3D cell scaffolds with a stable gradient of chemical species, i.e. growth factor to induce cell differentiation directly into the scaffold. The idea is to seed the cells in a 3D stiffness gradient scaffolds, and stimulate them with a 3D concentration gradient, in order to combine mechanical and chemical stimuli to drive tissue development.

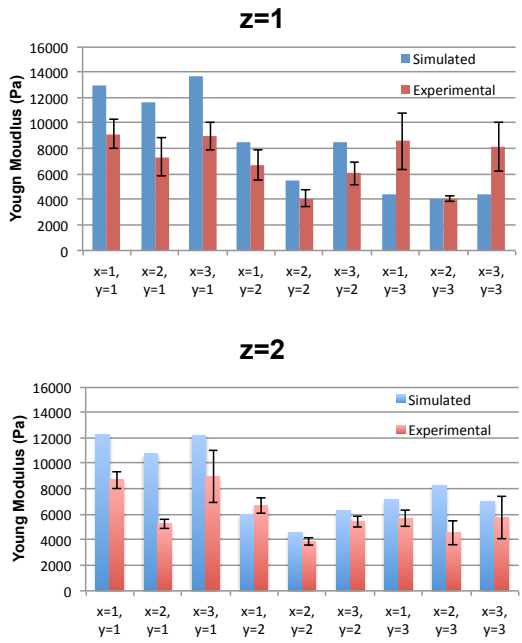

Figure 4.26: Experimental versus simulated Young modulus in the two upper slices: as it is possible to see there is not an exact matching, but the trends are, in general, close to each other.

Table 4.1: Parameters used in CFD

Parameter	Value	Symbol
Density	$10^3\,\mathrm{kg/m^3}$	ρ
Viscosity	$10^{-3}\,\mathrm{Pa\,s}$	μ
Diffusion Coefficient	$10^9\,\mathrm{m^2/s}$	D
Flow Rate	$170\,10^{-6}\,\mathrm{l/min}$	Q

Chapter 5

pH sensitive nano particles and their application

Luminescence imaging of biological parameters is an emerging field in biomedical sciences. Tools to study 2D pH distribution are needed to gain new insights into complex cellular processes. In recent years, luminescence-based methods for pH measurement have been developed. To create a biocompatible 2D sensor, sensitive nanoparticles could be immobilised inside a hydrogel matrix, in order to guarantee a proper SNR. Also inkjet printing is familiar as a method of printing text and images onto porous surfaces. In the last few years it has been used as a free-form fabrication method for building three-dimensional parts and is being explored as a way of printing electrical and optical devices. Inkjet printing was used either as a rapid prototyping method for custom biosensors. Sol-gel method is naturally bound with inkjet, because the picoliter-size ink droplets evaporate quickly, thus allowing quick sol-gel transitions on the printed surface. In this chapter will be shown how to merge those technologies, in order to make a nanoparticles doped printable hydrogel, and to realise 2D/3D smart scaffolds able to monitor cell activities.

An automated image analysis system was developed in order to quickly have the pH measurements from pH nano sensors fluorescence images.

5.1 Introduction

There is great interest in luminescence imaging of essential biological parameters, such as pH, pO_2 , hydrogen peroxide (H_2O_2), and Ca^{2+}, at the moment (84, 85, 86, 87, 88, 89). Recently, luminescence-based methods for pH measurement have been developed (90, 91). The standard tool for pH measurement, the glass electrode, only allows single-spot measurements, which makes 2D imaging impossible. Multiple methods for pH imaging exist: ratiometric luminescent pH detection is a straightforward and referenced approach, which has been used, for instance, to measure intracellular pH (92). In these works, either combinations of dextran-conjugated indicator and reference dyes (fluorescein/tetramethylrhodamine and pHrodo/ rhodamine-green) have been used (93, 94, 95, 96). However, to obtain 2D images, either modifications of the optical system during measurements or the use of an image splitter are necessary to separate the signals. Ratiometric methods may suffer from Forster's fluorescence resonance energy transfer (FRET) and most importantly, from differential photobleaching of indicator/reference dyes. Actually, no pH sensor exists that detects pH over a wide proton concentration range, allows for fast micro- and macroscopic 2D pH imaging, and is noninvasive and biocompatible for in vivo imaging. The University of Nottingham developed a fluorescent pH nanosensor that meets these requirements (92, 95, 97). The prerequisites include (i) the use of a referenced method, because in vivo conditions are quite variable, (ii) nontoxic and easily applicable materials, (iii) a dynamic range from pH 3 to

8, and (iv) a noninvasive method, allowing it to be suitable for clinical applications. Fluorescent pH-sensitive nanosensors are spherical probes typically composed of a pH-sensitive fluorophore and a pH-insensitive reference fluorophore encapsulated or covalently linked to an inert porous cross-linked matrix (98, 99). The inert matrix shields the fluorophores from cellular components, which could hinder sensing capabilities, while safeguarding biological components from free fluorophores (100). The combination of pH-sensitive and pH-insensitive fluorophores in a single nanoparticle enables accurate ratiometric pH measurements (101). Nanosensors composed of fluorescein based pH-sensitive fluorophores, such as carboxy- fluorescein (FAM) and Oregon Green (OG), when suspended in aqueous media, exhibit high and low fluorescent responses at near neutral and acidic pH values, respectively. This effect is due to the pH-dependent ionic equilibria of fluorescein based fluorophores, which demonstrate high quantum yields when fully ionised, e.g., in aqueous solutions greater than pH 8.0, and a diminished fluorescent response and quantum yields when protonated, e.g., in aqueous solutions with a pH less than 3.0. (102). Nanoparticles composed of a single pH-sensitive fluorophore, either FAM or OG, have a limited ranges of pH measurement, pH 5.00-7.50 and pH 3.50-6.00, respectively (95). In contrast, extended dynamic range pH-sensitive nanosensors, which combine FAM and OG in 1:1 ratio in a single nanosensor, are capable of measuring the full physiological pH range, from pH 3.50 to 7.50 (92, 97, 103, 104). The present work describes the application of extended dynamic range pH-sensitive nanosensors in making 2D pH sensitive surfaces. The nanosensors, opportunely immobilised into hydrogel matrixes, were used to convert pH dependent changes in fluorescence intensity into quantifiable pH measurements, using a custom automated image analysis system. The nanosensors were successfully used to sense pH within thin uniform PAAM and Gelatine/Glycydoxypropyl-trymethoxysilane (GPTMS) films,

and printed within a Gelatine/GPTMS Ink with a modified Inkjet printer.

5.2 pH sensitive nanoparticles

Extended dynamic range pH-sensitive nanosensors (97) were prepared by covalently linking pH- sensitive (FAM and OG) and pH-insensitive (TAMRA) fluorophores to N-(3-aminopropyl)methacrylamide (APMA), which was then copolymerised with acrylamide and TEMED to produce an inert polyacrylamide nanoparticle matrix, Figure 5.1.

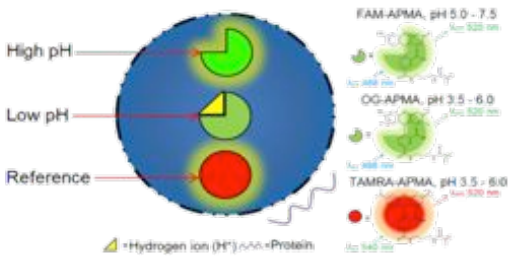

Figure 5.1: Schematic diagram of extended dynamic range pH-sensitive nanosensors.

Nanosensors were sized using environmental scanning electron microscopy (ESEM) and dynamic light scattering (DLS) and shown to have a nominal diameter of around 40 nm. FAM and OG are both excited at 488 nm for which they demonstrate a pH-dependent overlapping emission peak at 520 nm, whereas TAMRA, when excited at 540 nm, exhibits a pH-independent fluorescence response at 577 nm, Figure 5.2.

A ratiometric pH calibration curve can be generated, Figure 5.3, by taking a ratio of the fluorescence response of pH-sensitive and pH-insensitive channels (λem 520 nm/λem 577 nm) from nanosensors suspended in a range of pH buffer

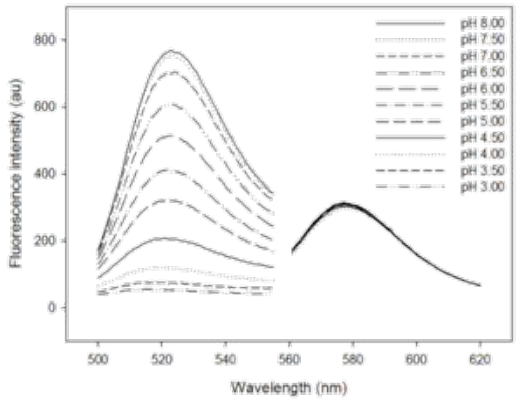

Figure 5.2: Emission curves for pH-sensitive nanosensors suspended in buffer solutions ranging from pH 3.00 to 8.00. FAM-APMA and OG-APMA both excite and emit fluorescence at 488 nm and 520 nm, respectively, whereas TAMRA-APMA excites and emits fluorescence at 540 nm and 577 nm, respectively.

solutions, Figure 5.3. The calibration curve can then be used to make accurate ratiometric pH measurements from environments containing pH-sensitive nanosensors. Synthesis of nanosensors with covalently linked fluorophores overcomes measurement inaccuracies associated with fluorophore leaching. Over time, nanosensors prepared through the encapsulation of dextran bound pH-sensitive fluorophores have been found to leach (105) Nanosensors which leach fluorophores are subject to pH measurement artefacts, as the operator cannot be certain if pH measurements are being made from the nanosensors or free fluorophore (106). Leached fluorophores could also initiate cellular toxicity due to photoexcitation and/or nonspecific protein binding (100). Nanosensors prepared with covalently linked fluorophores are also extremely bright when compared to nanosensors composed of encapsulated fluorophores(107). Brighter nanosensors allows:

1. a reduction in fluorescence excitation energy, preserving biological function and reduced fluorophore photobleaching (108);
2. use of lower nanosensors concentrations for measurement;
3. a reduction in the required exposure time of fluorescence microscopy, permitting faster imaging of dynamic process through increases in sampling rate.

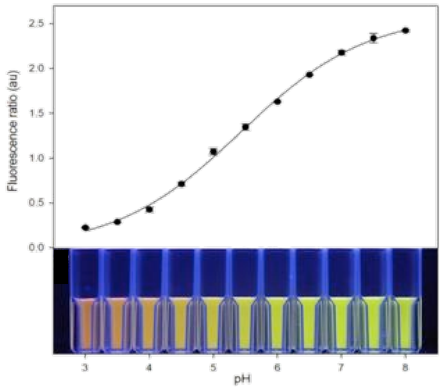

Figure 5.3: Calibration curve for pH-sensitive nanosensors suspended in buffer solutions ranging from pH 3.00 to 8.00. Data points for the calibration curve are fitted to a sigmoidal expression, where error bars represent standard deviation (pK_a = 5.44 (0.07). Below is depicted the ultraviolet trans-illuminated pH-sensitive nanosensors (λex 302 nm).

5.2.1 pH-Sensitive Nanosensor Synthesis

. As described in (97) Surfactants Brij 30 (3.080 g, 8.508 mmol), dioctyl sodium sulfosuccinate salt (1.590 g, 3.577 mmol) and deoxygenated hexane (42 mL) were stirred under argon for 10 min. Succinimidyl esters forms of the fluorophores were conjugated to APMA, via a nucleophilic addition reaction. FAM-APMA

(15 μL, 5 mg/mL), OG-APMA (15 μL, 5 mg/mL), TAMRA-APMA (60 μL, 5 mg/mL), acrylamide (0.540 g, 7.579 mmol), and N,N' methylenebis(acrylamide) (0.160 g, 1.307 mmol) were dissolved in deionized water made up to 2 mL. This monomer solution was added to the stirring hexane surfactant solution and allowed to deoxygenate for a further 10 min. Polymerisation initiators ammonium persulfate (30 μL, 10% w/v) and TEMED (15 μL, 0.1 mmol) were added to the stirring solution to initiate polymerisation. The mixture was left to stir for 2 h under argon. Hexane was removed via rotary evaporation. Nanoparticles were precipitated and washed with ethanol (30 mL) using centrifugation (10 times, 6000 rpm, 10 min), with a Hermle centrifuge (Z300). After the final wash, the pellet was resuspended in a small amount of ethanol (10 mL) and rotary evaporated until dry. Nanoparticles were stored in a light protected container at 4 degrees.

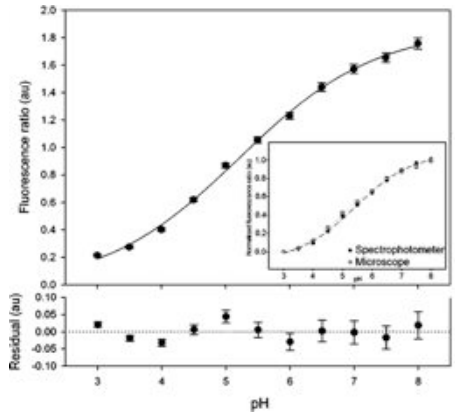

Figure 5.4: pH calibration for extended dynamic range pH-sensitive nanosensors and residual error, when imaged using fluorescence microscopy. (Inset) Comparison of normalised calibration curves from peak fluorescent intensity from fluorescence spectrophotometer and high-throughput analysis of pH calibration images.

5.3 Image Analysis

Interpretation of data from imaging can be variable and open to subjective input from the operator especially when handing large volumes of data (109, 110). To overcome these challenges, an automated image processing system, independent of the operator, was realised. The system is programmed to analyse images used for calibrating pH-sensitive nanosensors and then use this information to transform images for analysis to pH images for measurement. Calibration images were analysed, by taking a pixel-wise ratio of green and red fluorescent channels to obtain calibration points (I) from which a calibration curve was generated, Figure 5.4. Calibration curves are fitted to a sigmoidal function, as described in eq 5.1,

$$f(pH) = R_{min} + \frac{R_{max} - R_{min}}{1 + e^{[pK_a - pH/b]}} \tag{5.1}$$

where, R_min and R_max are the minimum and maximum fluorescent ratio, pK_a represents the pH at which the fluorophore exhibits its greatest sensitivity to changes in pH, and the slope factor b represents the sensitivity of the nanosensor to changes in pH (95, 97). Calibration curves generated from analysis of data from spectrophotometer and pH measurements made using a pH meter were used to validate the automated the image analysis system and used to determine the accuracy of extended dynamic range pH-sensitive nanosensors to make pH measurements. Figure 5.4 inset shows normalised ratiometric calibration curves from both peak fluorescence intensity from fluorescence spectrophotometer and high throughput methods using fluorescence microscope. Statistical analysis of both curves indicates there are no significant differences between the calibrations curves ($p < 0.05$) and have comparable pK_a values of 5.36 ± 0.16. Furthermore, Figure 5.5 confirms pH measurements made using the high-throughput image

analysis system are not statistically different to pH measurements made with the pH meter ($p < 0.05$). The Bland- Altman mean difference plot, Figure 5.5, also demonstrates concordance between the two methods,(111) such that between pH 3.50 and 7.50 the 95% confidence interval remains between 0.17 pH units, which could be taken to be the pH measurement resolution, Figure 5.5 . A ratiometric image was generated by taking a pixel- wise ratio of green and red fluorescent channels to produce a greyscale image which was transformed into a false colour pH heat map.

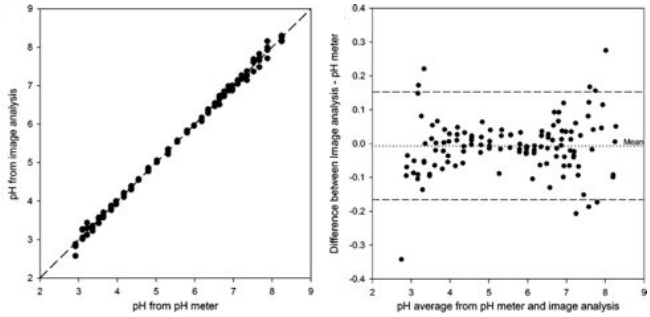

Figure 5.5: Left: Comparison of pH measurements made with pH meter and image analysis of pH calibration images. Right: Bland-Altman mean difference plot used to demonstrate agreement between pH measurements made with image analysis and pH meter where dashed lines and dotted lines represent 95% confidence intervals and mean of plotted data, respectively.

5.3.1 Calibration

Automated image analysis can be broken down to the two stages of 1) calibration and 2) pH image transformation. Calibration images were obtained by taking images of nanosensors suspended in buffer solutions ranging from pH 3.00 to 8.00. The microscope was focused using a scratch on inside of a glass bottom

dish and subsequently moved away from the scratch to acquire an image. All images were taken with sequential excitation at 475/28 nm and 542/27nm using the same settings (laser power, gain, and resolution) and fluorescence was collected using a polychroic quad mirror, at 523/36 nm and 594/45 nm, respectively. Automated image processing of calibration images was performed using the algorithm presented in Figure 5.6, implemented with MATLAB (see Appendix 2).

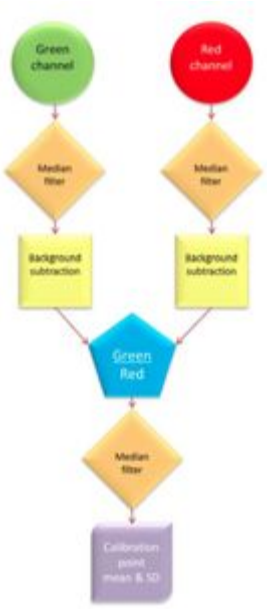

Figure 5.6: Algorithms used to derive calibration points for the curve fitting.

Initially, random saturated and blank pixels (salt and pepper noise) were removed from the FAM and OG (green) and TAMRA (red) channels images with a median filter (2.0 pixels). Background corrected images were generated through subtraction of green and red fluorescent intensities of suspensions containing

nanoparticles by solutions without nanoparticles. Ratiometric calibration images were created by taking a pixel wise ratio of the background corrected green and red fluorescent channels. An additional median filter (2.0 pixels radius) was applied to remove any further saturated/unsaturated pixels. Calibration points (I) were constructed by averaging 3 different ratiometric images and were fitted to a sigmoidal expression, as described in the main article. Non-linear parameter estimation of calibration curve was performed using the well-known sum squares weighted residuals method,(111, 112, 113, 114) which is based on minimising the following likelihood function ($l.f.$),

$$l.f. = \sum_{i=1}^{n} w_i \left[y_i - f(pH_i, R_{min}, R_{max}, pK_a, b) \right]^2 \tag{5.2}$$

where y_i, σ_i, pH_i representing respectively i-th point mean value, standard deviation and relative pH, whereas, w_i represents the weight of each point. Experimental data shows that the standard deviation of the fluorescent ratio increases with intensity value (Figure 5.4), suggesting the observed noise is proportional to fluorescence ratio rather than being absolute. Consequently, the classical weights scheme, where $w_i = 1/\sigma_i^2$, could lead to a biased estimation of the calibration curves, especially with the effect of negative bias at the higher pH values of the calibration curve. Therefore, for an unbiased estimation the inverse fractional variance, $w_i = 1/(\sigma_i/y_i)^2$, is used as weight, so that the relative importance of each point in the global fit is given by relative error for each calibration point.

5.3.2 pH Image generation

The algorithm, Figure 5.7, was used to obtain ratiometric images, from acquired green and red fluorescent channels. A ratiometric image was generated by taking a pixel-wise ratio of green and red fluorescent channels (with background

removed), in order to produce a grey scale image which was transformed into a false colour pH heat map using FIJI Open source software. Basically an inverse function of the sigmoidal calibration curve was used in order to transform Green/Red fluorescence ratio in pH. Ratiometric images were post-processed through introduction of pH measurement thresholds, to eliminate all pH measured values below 3.50 and above 7.50. This is because, as shown by the Bland-Altman mean difference plot, Figure 5.5, pH measurements made at the extremes of the calibration curves (<pH 3.50 and >pH 7.50) are either approaching saturation or are where the signal to noise ratio is low.

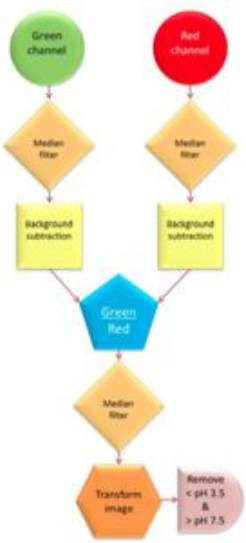

Figure 5.7: Algorithms used to transform fluorescence images in a proper false colour pH heat map.

5.3.3 Validation

In plane focused images (n = 4) of nanosensors suspended in buffer solutions (n = 31), ranging from pH 2.92 to 8.25 were acquired for measurement validation using the developed system. Student's t test was used to identify significant differences between measurements made with image analysis system and fluorescence spectrophotometer, and image analysis and pH meter. Measurements made using the automated image analysis system were compared to measurements made from a pH meter (Jenway 3510) and used to determine a method resolution using 95% confidence intervals on a Bland-Altman mean difference plot (Sigma-Plot 12.0). Colocalization analyses were performed using the *Coloc 2* macro on FIJI open source software, from which images with Pearson's correlation coefficients, for green and red fluorescent channels, greater than 0.95 were taken for pH measurement. The 95% confidence interval remains between 0.17 pH units, which could be taken to be the pH measurement resolution.

5.3.4 Application: Real Time Mapping the Pharyngeal and Intestinal pH of Caenorhabditis elegans

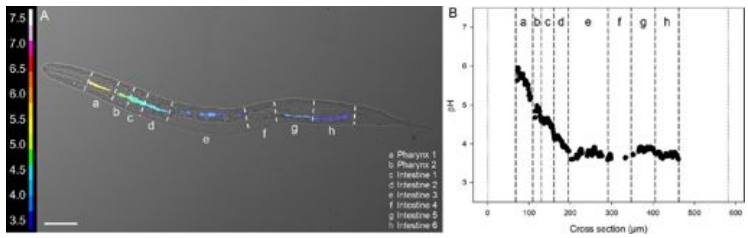

Figure 5.8: (A) Green, (B) red, and (C) merged fluorescence microscopy images of *C. elegans* with ingested extended dynamic range pH-sensitive nanosensors. (D) Co-localization analysis of green and red channels (Pearson's correlation coefficient = 0.98). (E) Transformed false colour pH heat map image. Scale bar = 50 μm.

Looking into living beings with non-invasive methods is a great challenge. In particular monitoring physiological variables in-vivo, such as pH, is extremely important. However pH probes can give only point wise averaged informations. An imaging system able to take "pictures" of what is happening in vivo could be an answer to common probes limits. Coupled with the ratiometric nanosensors developed by the University of Nottingham, the image processing algorithm was able to measure pharyngeal and intestinal pH in *C. elegans*, a nematode commonly used as animal model. The nanosensors were used to convert pH dependent changes in fluorescence intensity into quantifiable pH measurements, using the proposed automated image analysis system.

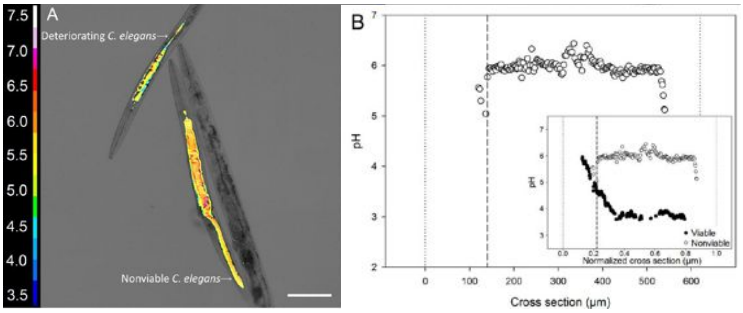

Figure 5.9: (A) pH image of nonviable *C. elegans* alongside a deteriorating nematode and a nonviable *C. elegans*, which has not ingested nanosensors. (B) Luminal pH values for nonviable nematodes and (inset) comparison of viable and nonviable *C. elegans* luminal pH, through normalization of worm anatomy. Dotted lines represent start of head and end of tail of nematode. Dashed line represents location of pharyngeal-intestinal junction. Scale bar = 100 μm.

The nanosensors were successfully delivered to nematodes and used to map pH of the pharyngeal and intestinal lumen of *C. elegans* in vivo (Figure 5.8), and to discriminate between live and dead nematodes (Figure 5.9). In addition, through control of the pharyngeal pumping rate, the acidification of the intestinal

lumen was mapped in real-time (Figure 5.10). Further details are available in the article (97).

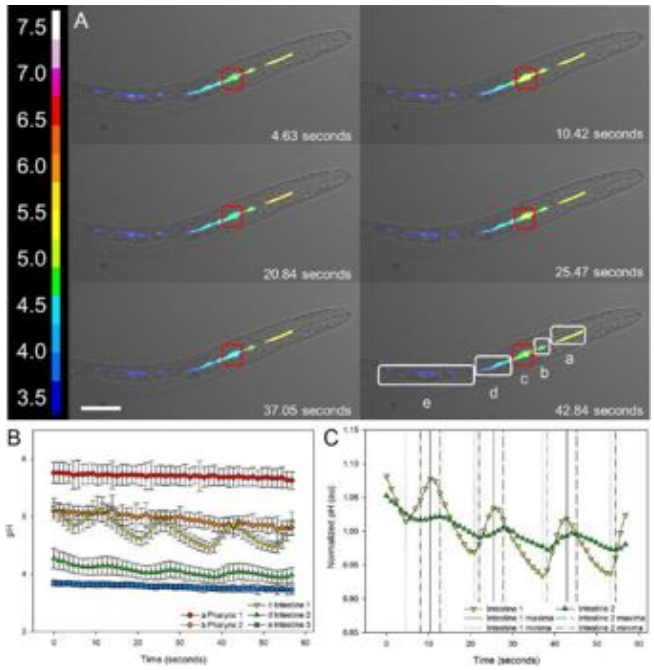

Figure 5.10: (A) Cross section of C.elegans at a peak(10.42, 25.47,and 42.84s) and trough(4.63,20.84,and 37.05 s)pH oscillations. (B) Measured and (C) normalized changes in pH over time. Regions a and b correspond to Pharynx 1 and Pharynx 2, whereas regions c to e correspond to Intestine 1 to Intestine 3. Error bars represent standard deviation of sampling area. Scale bar = 50 μm.

5.4 Developing thin hydrogels sensitive films

The objective was to create an engineered surface capable to sense pH variation. The first approach was to try to immobilise directly the pH sensitive nanoparticles on a surface, i.e glass, PDMS or plastic, but it did not give reliable results

on pH sensing. In fact the nano layer of immobilised particles gave a fluorescent signal with low SNR, making it unreliable for using it as pH sensor, while fluorescence was however visible. The idea, based on works of Wang (115) and Schreml (116), was to immobilise the nano sensor into an hydrogel matrix, that intrinsically assure ion diffusion needed for pH sensing. The chosen matrixes were polyacrylamide (PAAM) and Gelatine/GPTMS. The two hydrogels are formed with two different mechanisms: radical polymerisation and sol-gel transition, respectively.

5.4.1 PAAM chemistry

Polyacrylamide gels are formed by copolymerisation of acrylamide (AAM) and bis-acrylamide (BIS, N,N'-methylene-bis- acrylamide). The reaction is a vinyl addition polymerisation initiated by a free radical-generating system (117) (Figure 5.11). Polymerisation is initiated by ammonium persulfate (AP) and TEMED. The latter accelerates the rate of formation of free radicals from persulfate and these in turn catalyse polymerisation. The persulfate free radicals convert acrylamide monomers to free radicals which react with unactivated monomers to begin the polymerisation chain reaction (118). The elongating polymer chains are randomly crosslinked by BIS, resulting in a gel with a characteristic porosity which depends on the polymerisation conditions and monomer concentrations.

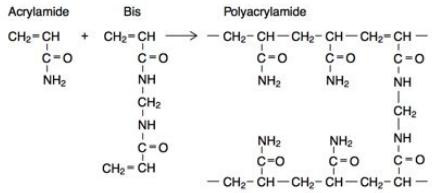

Figure 5.11: PAAM polymerisation scheme.

5.4.2 Gelatine/GPTMS Chemistry

γ-Glycidoxypropyltrimethoxysilane (GPTMS) is a silane-coupling agent, which has epoxy and methoxysilane groups. The oxirane rings on the GPTMS molecules react with the amino groups on the G chains and hydration of the trimethoxy groups on the GPTMS forms pendent silanol groups (Si-OH) through an acid catalysed reaction. Then Si-O-Si bonds were formed through condensation of two Si-OH occurring mainly during the solvent evaporation period of the membrane formation process. The Si-O-Si linkages formed from the condensation reaction provided inter-chain covalent bonds to result in a crosslinked structure (119, 120). Gelatin was chosen as the toughening polymer as it is a hydrolysed form of collagen, which is a major constituent of the extracellular matrix of all tissues and as such recognisable and adhered to by many cell types. Gelatin is more practical than collagen from a materials processing point of view and was preferred over other popular resorbable polyesters such as poly lactic and glycolic acids as these degrade through a self catalysed hydrolysis process that can lead to poor control of dissolution characteristics in vivo (121). Silica gelatine conventional composites have been synthesised in the past using sol-gel techniques,(122, 123, 124). Under acidic conditions,in fact, GPTMS is subject to cleavage of the C-O bond in the epoxy group (125). The protonated epoxy group is so activated to attack nucleophilic groups likeNH_2, or COOH on the amino acid residues comprising the gelatine chains that GPTMS molecules are grafted to the gelatine chains. It is thus likely that the hydrolysis and condensation of the metal alkoxides and ring-opening reactions of the epoxy groups yield a crosslinked network in the gelatin-siloxane hybrids as illustrated in Fig. 5.12 <Gelatin skeleton> R-Si-O-Si-R <Gelatin skeleton> (R denotes organic skeleton of GPSM) bonds are formed as the GPTMS molecules bridge a fraction

of such nucleophilic active sites on the side groups of the amino acid residues. However it is important to *dehydrate the sol in order to promote the gel formation*. By doing this the polycondensation of silica part can happen properly.The gel then can be rehydrated, and it proven to be stable in water at 70 degrees overnight.

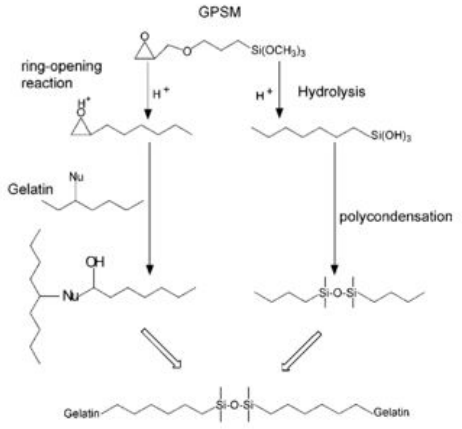

Figure 5.12: Scheme of Gelatin/GPTMS polymerisation.

5.4.3 Materials and methods

PAAM thin films (8% w/v AAM, 0.5% w/v BIS, 1/100 v/v of AP 10% w/v, 1/1000 v/v of TEMED) doped with 5 mg/ml PAAM pH nanosensors (45 μm size) were adhered on glass functionalised with methacryloxypropyltrymethoxysilane (MPTMS) were developed as effective pH sensitive surfaces. For making stable PAAM thin films the following protocol was used (Figure 5.13:

1. Clean the glass coverslips/slides with acetone, then rinse with deionised water and finally gently dry with a stream of nitrogen or air;

2. Dip a glass coverslip/slide inside a petri dish filled with 1% v/v MPTMS/water solution, and let them to react for 30 min. The MPTMS molecule binds itself to the glass, leaving the methacrylic groups exposed on the glass surface. They will act as anchoring sites for PAAM gel, because they will be covalently bonded within the PAAM network.
3. Mix AAM and BIS in a vial. The final solution was a mixture of 16% w/v AAM + 1% w/v BIS;
4. In another vial prepare a 10 mg/ml pH sensitive nanoparticles suspension. It is important to sonicate properly the suspension in order to uniform the nanoparticles concentration within the vial;
5. Mix the two solutions in a 1:1 v/v ratio, so obtaining a 8% w/v AAM, 0.5% w/v BIS, 5 mg/ml nanoparticles solution;
6. Add 1/100 v/v AP and 1/1000 v/v TEMED to the solution above, then vortex the mixture.
7. Quickly pipette 50 μL of the final solution on a functionalized glass coverslip. For functionalised microscope slides instead 3 x 50 50 μL must be spread over the glass.
8. Cover the glass with a not functionalised glass of the same size, and let the PAAM to polymerise for at least 4 hours (overnight preferred however). The surface tension align the two glass and distribute uniformly the solution. The not functionalised glass not anchors to PAAM, while the functionalised one does. In this manner removing the cover glass is easy and safe for the newly formed hydrogel. Spin coating can also be used as technique for making uniform thin films, so avoiding the glass-gel-glass sandwich.
9. Dismount the glass and collect the glass + PAAM slides.

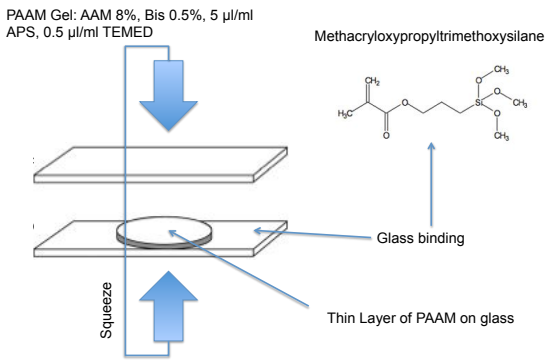

Figure 5.13: Scheme for making PAAM films without a spin-coater.

Gelatine (5% w/v) + GPTMS (96 μl / g Gelatine) films, doped with 5 mg/ml PAAM pH nanosensors were tested as pH sensitive surfaces. The protocol in this case was:

1. Clean the glass coverslips/slides with acetone, then rinse with deionised water and finally gently dry with a stream of nitrogen or air;
2. Put gelatine into water in order to reach 10% w/v.
3. Add 96 x 2 μl of GPTMS for each g of Gelatine used.
4. Stir the solution for 1 h at 60 degrees, activating the GPTMS-Gelatin bond.
5. Meanwhile prepare a 10 mg/ml pH sensitive nanoparticles suspension, and sonicate it.
6. Mix the two solutions, so reaching the final concentrations of Gelatine (5% w/v) + GPTMS (96 μl / g Gelatine) + 5 mg/ml nano sensors.
7. Deposit the solution on glass coverslips by spin coating.
8. Let the sample dry overnight in the hood, so activating polycondensation of GPTMS groups. In this case GPTMS self-adhere to glass, so the gel is

naturally anchored to the glass surface.

5.4.4 Results

Sensing properties of both kind of thin films were analysed. In particular a calibration curve was extracted with the methodologies described in par. 5.3.1. Both PAAM and Gelatin/GPTMS films showed good pH sensing features, as depicted in Figure 5.14. In It is interesting that the normalised calibration curves almost collapse, meaning that the hydrogel matrix did not interfere with fluorescence sensing. In the end however Gelatin/GPTMS ones demonstrated better performances, because they are easier and safer to make (not polymerised AAM is hazardous).

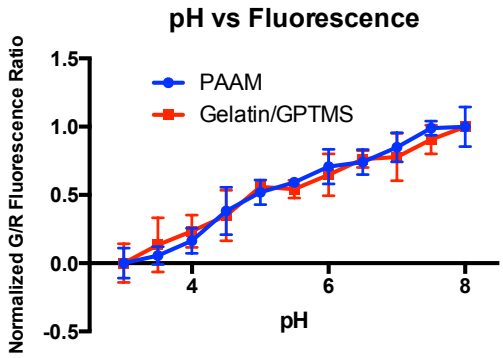

Figure 5.14: View of calibration curve of PAAM and Gelatine/GPTMS thin films. The normalised calibration curves almost collapse, meaning that the hydrogel matrix did not interfere with fluorescence sensing.

5.5 Printing pH sensitive Inks

Inkjet printing is familiar as a method of printing text and images onto porous surfaces. In the last few years it has been used as a free-form fabrication method for building three- dimensional parts and is being explored as a way of printing electrical and optical devices, especially where these involve organic components. Inkjet printers are also being used to produce arrays of proteins and nucleic acids. Inkjet printing was also used either as a rapid prototyping method for custom biosensors. Sol- gel method is naturally bound with inkjet, because the picoliter-size ink droplets evaporate quickly, thus allowing quick sol-gel transitions on the printed surface.

5.5.1 Materials and methods

A Gelatine (0.1%) + GPTMS (96 μl / g Gelatine) + 1 mg/ml PAAM pH nanosensors mixture was tested as ink for a modified commercial inkjet printer, coming from a previous work of Dr. De Maria (126), Figure 5.15. After the printer cartridge was filled with the Ink, frid patterns with lines of 250 m, spaced by 750m (Figure 5.16) were printed on 18mm x 18mm glass coverslips. The glass coverslips were then or left to dry overnight, or dried with the heat of an incandescence lamp. The choice of the Ink composition was done after a trial and error procedure, starting from the composition of thins films and diluting it until the Ink was printable. Once dried, fluorescence signal of the structures was measured in different pH conditions, as did in par. 5.3.1.

5.5.2 Cell tests

BJ skin fibroblasts were cultivated on the previously made structures, in order to check the ink biocompatibility. Briefly, the printed coverslips were placed into

Figure 5.15: View of the modified inkjet printer by De Maria et al. (126).

a 6-wells multi well plate. In particular in 3 wells were placed the coverslips+ink structures. The structures then were seeded with BJ skin fibroblasts, and left to arrive at complete confluence, in order to see if there were differences in cell density between zones with and without the printed structure.

5.6 Results

Printed patterns show no sign of degradation after 3 days in water at 60C, and are able to self-adhere to the glass thanks to covalent bonding. Also the fluorescent signal of patterns is still viable, and can act as pH sensitive surface. As it is possible to see from Figure 5.17 the fluorescence response in function of pH is still in the printed nano structures. In particular the green signal is, as expected, stronger at high pH and almost negligible at low one, while the red signal is stable at any pH, acting so properly as reference. Enhanced fluorescence at the borders of the structures respect to inside are due to coffee-ring (127) effects, that concentrates the nanoparticles in the borders.

Finally the seeded cells show no differences in colonisation between the glass

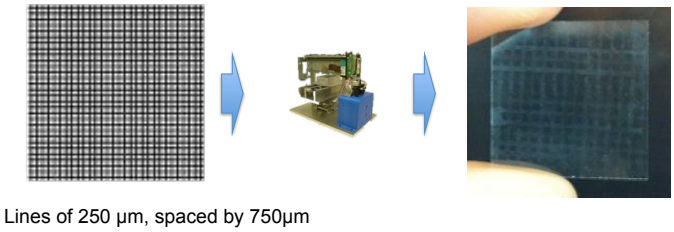

Figure 5.16: View of the printing conceptual scheme: from grid concept to print on glass coverslip.

and the Gelatin/GPTMS/Nanoparticles pattern, as it is possible to see in Figure 5.18 and 5.19, where the red signal, showing the structures, was merged to a phase contrast image of the cells. Fluorescence signal is still available on printed pattern after 4 days of cell culture. The Inkjet printed structures are then a reliable biocompatible pH sensor.

5.7 Conclusions

In conclusion thin hydrogel sensitive surfaces, doped with nanoparticles proven to be a reliable and biocompatible pH sensor. It is to note that the application field could not be directly monitoring pH in standard cell cultures, because the environment of a classic petri dish is highly buffered and has already the colour indicators (i.e. Phenol Red) for bulk pH variation. Widely used non buffered cell culture environments such as the Xenopus one, however, could be a natural application of this work, which demonstrated successfully the proof of concept of printed sensitive surfaces. Inkjet printing also allows making smart scaffolds of Gelatin/GPTMS, which inner behaviour could be investigated by

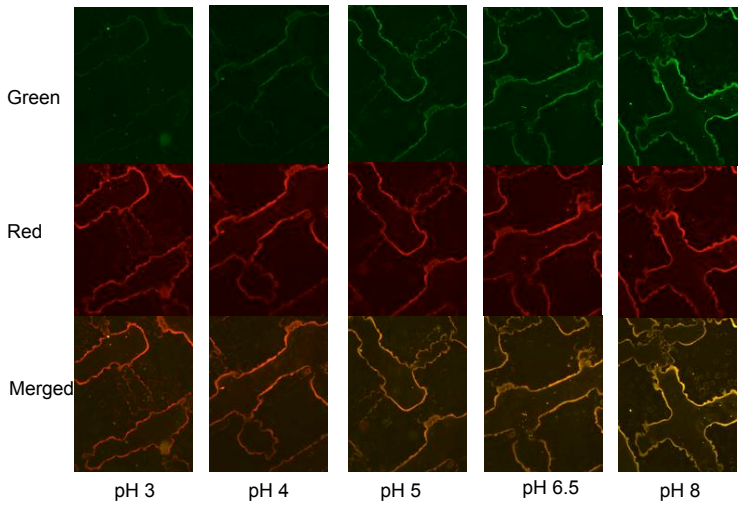

Figure 5.17: View of the fluorescence response of the structures at different pH. The green signal is higher at high pH, and almost negligible at low one. The red signal is stable at any pH, acting properly as reference. The image at the bottom is obtained by merging the G/R channels.

optical fluorescence techniques, such as confocal microscopy, in order to have a measure on the local environment pH.

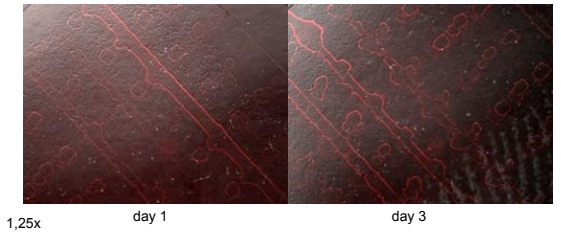

Figure 5.18: 1.25x magnification of the cells seeded on the glass coverslip with the structures. There is no difference of cell density between the structure and the free coverslip, meaning that the structure is biocompatible.

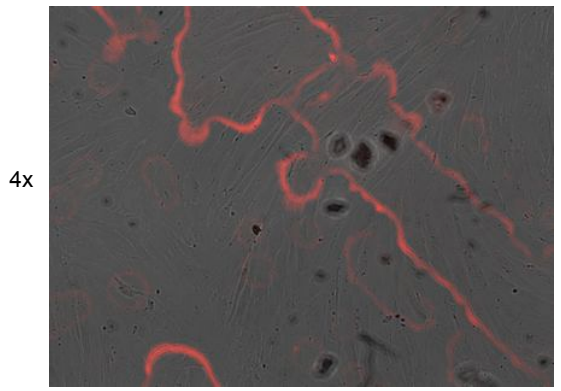

Figure 5.19: 4x magnification of the cells seeded on the glass coverslip with the structures. Also in this case there is no difference between cell density inside and outside the printed structures.

Conclusion

Microfluidic concentration Gradient Makers (GM)of various kind were developed, analysed and realised during this PhD. Several tools ranging from theoretical, simulations and experimental realisation allowed to gain insight about the properties of GM systems. First of all an engineered microfluidic concentration GM was successfully developed and realised. The match between expected, simulated and experimental behaviour of the device was proven to be very close. However the first version of the microdevice was not suitable for cell culturing, because the hydrophobicity of PDMS was an obstacle to GM perfusion, causing unwanted burst due to the local high pressure. Even in the case of plasma-treated PDMS-Glass devices there was an hydrophobic recovery after 40 minutes, which caused serious issues during cells seeding phase by injection from the device outlet. In fact cells were subjected to very high shear stresses during this phase, leading them to death. Also the small hydrophobic channels acted as nucleation sites for air bubbles (effect also amplified in cell medium culture respect to water), that can both clog the micro channels and destroy the cells at the air/liquid interface. Those problems were resolved in the second version of the GM, which presented a bigger culture chamber, allowing to insert a glass/plastic slide already with seeded cells into the device and starting the experiment. The hydrophobicity problem was solved using nonionic surfactants

(Brij35 and Tween20) mixed with the PDMS in order to make it act with an hydrophilic behaviour. Thanks to capillary pressure, in fact, air bubbles were automatically removed in hydrophilic micro channels. The hydrophilic PDMS was then enclosed between two thick Plexiglas pieces, allowing it to be sealed just by pressure. This new layout was completed with a CFD analysis of the "robustness" of the new layout, in order to understand the sensitivity of the formed gradient to flow conditions different from the nominal case. Root Mean Square (RMS) differences between expected and simulated behaviour were in fact analysed. Peclet number was shown to be the quantity that regulated the device performances: in particular with Pe of culture chamber >10 the concentration profile was always matching the desired one. The device was proven to be more sensitive to inlets flow ratio, which shows a narrow effective working range instead, however still compatible with common peristaltic pump requirements. PDMS modified with Brij 35 resulted to have better features than the one modified with Tween 20. In particular Brij 35/PDMS resulted to have lesser contact angle (down to 40 degree in the long run, instead of 60 degrees related to Tween 20/PDMS), minor characteristic time (3200s for Brij vs 4900s for Tween) and better transparency of its Tween 20 counterpart. Capillary velocity was measured in microchannels made with PDMS modified with 3% Brij, and the flow was resulted to be successfully capillary-driven, so eliminating the bubbles in the micro channels autonomously, without the need of pressurising the system. However while the new layout was proven to be easier to use with cells, the device was still not usable for cell culturing. In fact interactions of hydrophilic PDMS with the surfactants inside the medium culture led into pouring from inlets and micro channels network. So the cell culturing problem was still unresolved. So the whole device was made in Plexiglas by laser micromachining (microchannels width of 250 μm), and sealed with a custom nuts and bolts locking system. A

thin PDMS layer was used as gasket between the PMMA layers. In this case all perfusion problems were finally resolved, and the device was proven to be effective with cells . A 10^x shaped concentration H_2O_2 gradient $[0;10^{-2}]$ mM was, in fact, let to flow in the culture chamber for 3h. The percentage of live cells/total cells for each zone was evaluated by Live/Dead assay, in order to evaluate the effect of H_2O_2 on seeded cells. A dose-response curve was successfully extrapolated in a one-shot experiment, and a LC_{50} successfully evaluated. This kind of approach could be easily extended to other drug or pollutant in order to extract parameters of interests such as LC_{50}. The device could also have several applications in pharmacological testing and chemotaxis research. Then a conceptual shift was made, where the GM concept was extended from 2D to 3D. The 3D GM developed, in fact, preserved some characteristics of its 2D predecessors, i.e. the micro channel network. The device was first characterized using Computational Fluid Dynamics. Then the device has been realised using 3D rapid prototyping techniques. Prototype performances have been tested on a hydrogel matrix used as tissue model, placed in the GM chamber. Also this GM showed the ability to be used to fabricate hydrogel substrates with 3D gradient of stiffness. The 3D GM could have several applications in studying phenomena related to cell chemotaxis and durotaxis, but also on differentiation in simultaneous presence of gradients of both soluble chemical species and substrates stiffness. The device could be used in two ways: generating 3D concentration gradients of multiple substances, and generating 3D stiffness gradient for the same purpose, in order to promote differentiation and/or differential durotaxis. FEA and experimental studies were used to validate the 3D gradient of stiffness, which shows to be close to simulated one only in a part of the device. Finally there was the need to develop 2D pH nano sensors with the perspective to be

integrated into the micro devices. To create a biocompatible 2D pH sensor, sensitive nanoparticles could be immobilised inside a hydrogel matrix, in order to guarantee a proper fluorescence SNR. The extended range pH sensitive nanoparticles were developed by the University of Nottingham, and the collaboration with that foreign university led to the development of those sensitive surfaces. The nanosensors were successfully used to sense pH within thin uniform PAAM and Gelatine/Glycydoxypropyl-trymethoxysilane (GPTMS) films. The idea of sensitive surfaces was then extended using inkjet printing coupled with Sol-gel method, which is naturally bound with inkjet technology, because the picoliter-size ink droplets evaporate quickly, thus allowing quick sol-gel transitions on the printed surface. A Gelatine/GPTMS Ink doped with the pH sensitive nanoparticles was successfully printed with a modified Inkjet printer. Thanks to inkjet printing is also possible to look at 3D smart scaffolds of Gelatine/GPTMS, which inner behaviour could be investigated by optical fluorescence techniques, such as confocal microscopy, in order to have a measure on the local pH. An automated image analysis system was also developed in order to quickly have the pH measurements from pH nano sensors fluorescence images, and was successfully applied in measuring the pharyngeal and intestinal pH of Caenorabditis Elegans, a nematode commonly used as animal model.

Appendix 1

Main.m

```
%The function generates a complete concentration gradient maker in a ...
    .dxf file
%given a set of parameters

clear
clc
close all

%Parameters


N=3;                                %Number of desired layers
q=ones(1,2^N+1);

D=5e-10;                            %m^2/s      Diffusion Coefficient
w=250e-6;                    %m          Microchannels width
h=600e-6;                           %m          Microchannels heigth

lchamber=38e-3;                     %m          Size of the culture chamber
vtypical=(1e-4)*19e-3/lchamber;     %m/s        Velocity in cell ...
    culture chamber
eta=1e-3;                           %Pa*s       Viscosity of fluid
kappa=12*eta/(w-0.63*h)/h^3;        %Pa*s/m^4   Hydraulic resistance ...
    constant
```

APPENDIX 1

```
rho=1000;                          %Kg/m^3     Density of fluid

A=w*h;                             %m^2        Channel Section
P=2*(w+h);                    %m          Channel Perimeter

Dh=4*A/P;                          %m          Hydraulic diameter of ...
    the channel

x=linspace(0,3,(2^N)+1);             %           Interval of x ...
    function coordinates

f=@(x)10^x                    %           Function

ck=arrayfun(f,x);

plot(x,ck,'o');

%Campbell & Groisman algorithm

ck=[zeros(N,length(ck));ck];

for i=(N+1):-1:2
    k=1;
    for j=1:2:(2^(i-1)+1)
        ck(i-1,k)=ck(i,j);
        k=k+1;
    end
end


alpha=zeros(N,(length(ck)+1)/2);
beta=zeros(N,(length(ck)+1)/2);
q=[zeros(N,length(q));q];
for i=(N+1):-1:2
    for n=2:(2^(i-2)+1)
        alpha(i-1,n)=(ck(i,2*n-2)-ck(i-1,n-1))/(ck(i-1,n)-ck(i-1,n-1));
    end
    for n=1:(2^(i-2))
        beta(i-1,n)=(ck(i,2*n)-ck(i-1,n+1))/(ck(i-1,n)-ck(i-1,n+1));
    end
end
```

```
                            %Flux ratios
for i=(N+1):-1:2
    for n=1:(2^(i-2)+1)
        switch (n)
            case {1}
                q(i-1,n)=q(i,2*n-1)+beta(i-1,n)*q(i,2*n);
            case {2^(i-2)+1}
                q(i-1,n)=alpha(i-1,n)*q(i,2*n-2)+q(i,2*n-1);
            otherwise
                q(i-1,n)=alpha(i-1,n)*q(i,2*n-2)+q(i,2*n-1)+beta(i-1,n)*q(i,2*n);
        end
    end
end

                            %length to length ratios
l=q*0;
for i=(N+1):-1:2
    [val,j_max]=max(q(:,i));
    for j=1:(2^(i-1)+1)
        l(i,j)=q(i,j_max)/q(i,j)*2^(N+1-i);
    end
end

                            %Flux in culture chamber m^3/s
qch=vtypical*h*lchamber;

                            %Fluxes in channels m^3/s
qr=qch/(2^N+1)*q/q(end,1);

                            %Velocities m/s
v=qr/A

%Reynolds number
Re=v*rho/eta*Dh;

                            %Maximum velocity channel features
[aux,i]=max(v(2:end,:))
[vmax,j]=max(aux)
lmin=l(i(j)+1,j)
l
                            %Channel Length
l=l*w^2/D*vmax/lmin;
```

```
                                %Hydraulic resistance
R=kappa*l;
                                %Pressure drop (Pa)
deltaP=qr.*R;

                                %Inlets
l(1,1)=1e3*Dh*0.06*Re(1,1);
l(1,2)=l(1,1);

d0=3*w;                             %Inlet distance
di=3*w;                         %Serpentine lateral distance


dd=ones(size(l));

for i=2:(N+1)
    dd(i,1:(2^(i-1)+1))=(lchamber-w-(2^(i-1))*4*w)/(2*(2^(i-1)+1)-2);

end

n=floor((l-w-2*d0)./(2*dd+di));

ns_v=max(n,[],2);
ns=ns_v;
for i=2:length(l)
        ns=[ns,ns_v];
end

dls=(l-ns*di-2*d0-w)./ns;
d_n=(ns+1)*w+ns*di+2*d0;

w=w*1e3;
dls=dls*1e3;
l=l*1e3;
h=h*1e3;
di=di*1e3;
d_n=d_n*1e3;

chl=10*w;

                                % Circuit generation
```

```
cube_dxf('ciao2',[],0)

off=-lchamber/2*1e3;

ppp=diff(linspace(off,-off,2^N+1))/2

off0=off;

ch_lg=5;

points=cube([off0-w/2;-ch_lg+ch_lg/4;0],[abs(2*off0)+w;ch_lg/4;h]);
cube_dxf('ciao2',points,1);
points=cube([-19/2;-ch_lg/4-19-19/2;0],[19;19;h]);
cube_dxf('ciao2',points,1);

for i=(N+1):-1:2

    aa=linspace(off,-off,2^(i-1)+1);
    points=cube([off-w/2;chl*(N-i)+sum(d_n((N+1):-1:(i)));0],[abs(2*off)+w;chl;h]);
    cube_dxf('ciao2',points,1);
                                %Serpentine generation
    for j=1:(2^(i-1)+1)
                    serpentine_center('ciao2',[aa(j);chl*(N-i)+sum(d_n((N+1):-1:(i+1
    end

end
                            %Chamber generation
points=cube([(off-w)/2;chl*(N-i+1)+sum(d_n((N+1):-1:(i)));0],[w;l(1,1);h]);
cube_dxf('ciao2',points,1);
points=cube([(off-w)/2+abs(off-w);chl*(N-i+1)+sum(d_n((N+1):-1:(i)));0],[w;l(1,2);h]
cube_dxf('ciao2',points,1);

cube_dxf('ciao2',[],2)
```

Serpentine_center.m

```
function [] = serpentine_center(fname,pos,w,h,l,n)
                            % This function writes a  a serpentine ...
                                channel in a .dxf file fname,
```

```
                            % in position pos, with channel width w, ...
                                height h, total length l and with n ...
                                turns

d0=3*w;                             %Distance from inlet
di=3*w;                             %Distance from outlet
d=(l-n*di-2*d0-w)/n;                    %Distance between serpentine turns

                            %inlet
points=cube(pos+[-w/2;0;0],[w;d0;h]);
cube_dxf(fname,points,1);
points=cube(pos+[-w/2;0;0],[w;w/2;h]);
cube_dxf(fname,points,1);

                            %Container
points=cube(pos+[-d/2;d0;0],[d;(n+1)*w+n*di;h]);
cube_dxf(fname,points,1);

                            %Dividers

points=cube(pos+[-d/2;d0;0],[d/2-w/2;w;h]);
cube_dxf(fname,points,1);
for i=1:n
    points=cube(pos+[mod(i+1,2)*w-d/2;d0+i*w+di*(i-1);0],[d-w;+di;h]);
    cube_dxf(fname,points,1);
end
points=cube(pos+[-d/2+(d/2+w/2)*mod(i+1,2);d0+n*w+di*n;0],[d/2-w/2;w;h]);
cube_dxf(fname,points,1);

                            %Outlet

points=cube(pos+[-w/2;d0+(n+1)*w+n*di;h],[w,d0,h]);
cube_dxf(fname,points,1);
points=cube(pos+[-w/2;d0+(n+1)*w+n*di+d0-w/2;h],[w,w/2,h]);
cube_dxf(fname,points,1);

end
```

cube_dxf.m

```
function[]=cube_dxf(fname,points,sit_code)

                            % Given a filename and a set of points ...
                                in standard format it writes a ...
                                parallelepiped
                            % in a .dxf file with name fname
                            % The data format is the vector points, ...
                                which is a vector with ...
                                ([X,Y,Z],[dx,dy,dz]).
                            % X,Y,Z are the co-ordinates of bottom ...
                                left parallelepiped angle, while ...
                                dx,dy,dz are the
                            %parallelepiped dimensions.
                            %sit_code represents the action to be done:
                            %   sit_code = 0 creates the .dxf file
                            %   sit_code = 1 add a parallelepiped to ...
                                the .dxf file
                            %   sit_code = 2 closes the .dxf file

fullname=sprintf('%s.dxf',fname);

switch sit_code
    case 0
        fid=fopen(fullname,'w');
        fprintf(fid,'0\nSECTION\n2\nHEADER\n0\nENDSEC\n0\nSECTION\n2\nENTITIES\n0\n'
    case 1
        fid=fopen(fullname,'a');

        fprintf(fid,'3DFACE\n8\n0\n');
        %top left corner
        fprintf(fid,'10\n%.10f\n20\n%.10f\n30\n%.10f\n',points(:,3));
       %top right corner
        fprintf(fid,'11\n%.10f\n21\n%.10f\n31\n%.10f\n',points(:,7));
        %bottom right corner
        fprintf(fid,'12\n%.10f\n22\n%.10f\n32\n%.10f\n',points(:,5));
        %bottom left corner
        fprintf(fid,'13\n%.10f\n23\n%.10f\n33\n%.10f\n',points(:,1));
        %thickness
        fprintf(fid,'39\n%.10f\n',points(3,2)-points(3,1));
        fprintf(fid,'0\n');

        fid=fopen(fullname,'a');
```

```
        fprintf(fid,'ENDSEC\n0\nEOF\n');
end

fclose(fid);

end
```

Appendix 2

CalCurve20.m

```
                    %The function make a quick calibration of pH ...
                        nanosensors
                    %based on image analysis
close all
clear all
clc

                    %The name of the folder where images are. This ...
                        must be located in
                    %/localfolder/Data/


background_name='Water';
calibration_name='Calibration_';
green_name='_R3D_w523';
red_name='_R3D_w594';

                    %Image format
iformat='.tif';

files_bg_g = ...
    dir(strcat(cd,'/',background_name,'*',green_name,'*',iformat));
files_bg_r = ...
    dir(strcat(cd,'/',background_name,'*',red_name,'*',iformat));
```

```
files_cal_g = ...
    dir(strcat(cd,'/',calibration_name,'*',green_name,'*',iformat));
files_cal_r = ...
    dir(strcat(cd,'/',calibration_name,'*',red_name,'*',iformat));

                    %pH series
pH=load('pH.txt');

                    %Number of repetition for each calibration image
n=4;

%Image size
imsize=1024;

%Vector allocation
avg=zeros(1,length(pH));
sd=avg;
md=avg;
CV=avg;

% Background estimation
% set zeros
% bg_g=uint16(zeros(1024,1024));
% bg_r=uint16(zeros(1024,1024));

%read in images

bg_g=[];
bg_r=[];
for i=1:numel(files_bg_g);
    bg_g=[bg_g,medfilt2(uint16(imread(strcat(cd,'/',files_bg_g(i).name))))];
    bg_r=[bg_r,medfilt2(uint16(imread(strcat(cd,'/',files_bg_r(i).name))))];

end
% divide sums by number of images
bg_g=uint16(double(bg_g)/double(numel(files_bg_g)));
bg_r=uint16(double(bg_r)/double(numel(files_bg_r)));

% bg_g=110;
% bg_r=100;

for i=1:n:(length(pH)*n)
```

```
    %Image acquisition
    %green  – green channel image
    %red    – red channel image

%     green=uint16(zeros(1024,1024));
%     red=uint16(zeros(1024,1024));
green=[];
red=[];

    for j=1:n
        i+j-1;
        green=[green,imread(strcat(cd,'/',files_cal_g(i+j-1).name))];
        red=[red,imread(strcat(cd,'/',files_cal_r(i+j-1).name))];

    end


    green=green-mean2(bg_g);
    red=red-mean2(bg_r);


    rimage=double(green)./double(red);

    rimage=medfilt2(rimage);

    %Calibration extraction
    %avg    = average of the image
    %sd     = standard deviation of the image
    %md     = median of image

    [w,h]=size(rimage);
    resh_image=reshape(rimage,1,w*h);

    ind=(i+j-1)/n;

    avg(ind)=nanmean(resh_image);
    sd(ind)=nanstd(resh_image);
    md(ind)=nanmedian(resh_image);
    CV(ind)=sd(ind)/avg(ind)*100;
```

```
    errorbar(pH(1:ind),avg(1:ind),sd(1:ind),'o'),...
        %     plot(pH(1:i),avg(1:i),'o'),...
    xlim([min(pH)*0.9 max(pH)+0.1*min(pH)]),...
        xlabel('pH'),...
        ylabel('G/R Intensity Ratio');
    drawnow;



end

%Curve fitting procedure
% LB — Parameters lower boundaries vector
% UB — Parameters upper boundaries vector
% par0 — Parameter initial guess vector
% weights — Weights vector

LB=[0 0 0 0];
UB=[2*max(avg) 2*min(avg) Inf 14];
par0=[max(avg) 0.04 0.1 5.3];
weights=1./((sd./sd).^2);



%Defining fitting options
s = fitoptions('Method','NonlinearLeastSquares',... %Estimation ...
    algorithm
    'Lower',LB,...                %Parameters lower boundaries
    'Upper',UB,...                %Parameters upper boundaries
    'Startpoint',par0,...         %Parameters initial guess
    'Weights',weights,...
    'Exclude',[0 0 0 0 0 0 0 0 0]);          %Weights vector

%Defining fitting object
f = fittype('Imin+(Imax-Imin)/(1+exp((pKa-pH)/b))',...
    'independent','pH',...
    'options',s);

%Experimental Data Fitting
[c_fit,gof,output] = fit(pH',avg',f)
```

```
%Final curve plot, with function prediction boundaries
hold on
plot(c_fit,'predfunc',0.68),...
    xlim([min(pH)*0.9 max(pH)+0.1*min(pH)]),...
    xlabel('pH'),...
    ylabel('Intensity');
hold off

pp=coeffvalues(c_fit);

cc=@(x)pp(2)+(pp(1)-pp(2))/(1+exp((pp(4)-x)/pp(3)));

res=avg-arrayfun(cc,pH);

figure
plot(c_fit,pH',avg','o','residuals')

FID=fopen(strcat(cd,'_cal_curve.txt'),'w');
fprintf(FID,'0\tImax\tImin\tb\tpKa\r\n');
fprintf(FID,'Value\t%f\t%f\t%f\t%f\r\n',coeffvalues(c_fit));
fprintf(FID,'SD\t%f\t%f\t%f\t%f\r\n',diff(confint(c_fit,0.68)));
fprintf(FID,'CV\t%f\t%f\t%f\t%f\r\n',(diff(confint(c_fit,0.68)))./coeffvalues(c_fit)
fclose(FID);
```

ImagepH20.m

```
%Open calibration curve file
close all
clear all
clc

fold_name='final stoat123';
localfolder='/Users/gianniorsi/Documents/MATLAB/Image Analysis ...
    Rob/Data/';
resfolder='/Users/gianniorsi/Documents/MATLAB/Image Analysis ...
    Rob/Results/';

bg_folder='Spheroid control nosensors/4/';
calibration_folder='1 mgml/4';
file_folder='Stack 1/4/';
```

```
background_name='stoat contro_z0';
file_name='stoat3          _z';
green_name= '_ch06';
red_name=   '_ch14';


%Image format
iformat='.tif';

files_bg_g = ...
    dir(strcat(localfolder,fold_name,'/',bg_folder,background_name,'*',green_name,iformat));
files_bg_r = ...
    dir(strcat(localfolder,fold_name,'/',bg_folder,background_name,'*',red_name,iformat));

files_g = ...
    dir(strcat(localfolder,fold_name,'/',file_folder,file_name,'*',green_name,iformat));
files_r = ...
    dir(strcat(localfolder,fold_name,'/',file_folder,file_name,'*',red_name,iformat));

%Calibration Curve acquisition
alldata=importdata(strcat(localfolder,fold_name,'/',calibration_folder,'/',fold_name,'_cal_cu
Imax=alldata.data(1,1);
Imin=alldata.data(1,2);
b=alldata.data(1,3);
pKa=alldata.data(1,4);

I=Imin:(Imax-Imin)/100:Imax;

pH=@(I)pKa-b*log((Imax-Imin)/(I-Imin)-1);

plot(I,arrayfun(pH,I))

%Number of images
n=numel(files_g);


tic
% Background estimation
% set zeros
bg_g=uint8(zeros(512,512));
bg_r=uint8(zeros(512,512));
```

```
%read in images
for i=1:numel(files_bg_g);
    bg_g=bg_g+medfilt2((imread(strcat(localfolder,fold_name,'/',bg_folder,files_bg_g
    bg_r=bg_r+medfilt2((imread(strcat(localfolder,fold_name,'/',bg_folder,files_bg_r

end
%divide sums by number of images
bg_g=bg_g/(numel(files_bg_g));
bg_r=bg_r/(numel(files_bg_r));

% bg_g=120;
% bg_r=125;
toc

% bg_g=180;
% bg_r=185;

tic


for k=1:n


     green=imread(strcat(localfolder,fold_name,'/',file_folder,files_g(k).name));
        red=imread(strcat(localfolder,fold_name,'/',file_folder,files_r(k).name));
%     grey=(imread(strcat(localfolder,fold_name,'/',files_br(k).name)));

    green=reshape(green,1,512*512);
      kk=find(green >= 250);
      green(kk)=NaN;
      green=reshape(green,512,512);

      red=reshape(red,1,512*512);
      kk=find(red >= 250);
      red(kk)=NaN;
      red=reshape(red,512,512);

    green=medfilt2(green-max(max(bg_g)));
    red=medfilt2(red-max(max(bg_r)));

    rimage=double(green)./double(red);
```

```
    resh_image=reshape(rimage,1,512*512);
    i=find(resh_image>=Imax);
    j=find(resh_image<=Imin);

    pHimage=arrayfun(pH,resh_image);

    pHimage(i)=NaN;
    pHimage(j)=NaN;

    i=find(pHimage>7.5);
    j=find(pHimage<4.5);
    pHimage(i)=NaN;
    pHimage(j)=NaN;

    pHimage=reshape(pHimage,512,512);


    pHimage=medfilt2(pHimage);

    barr=flipud([NaN*ones(1,6),linspace(4.5,7.5,500),NaN*ones(1,6)]');
    c_scale=[];
    for cc=1:20
        c_scale=[c_scale,barr];
    end
    blank=NaN*c_scale;


    pHimage=[blank,c_scale,blank,pHimage];

    resc=uint16((pHimage-4)/(8-4)*(2^16-1));

    fname=files_g(k).name;



    imwrite(resc,strcat(resfolder,fold_name,'/',file_folder,'pH ...
        Images/pH_',fname(1:end-4),'.tif'),'tif');
    save(fname(1:end-9),'pHimage');
    k

end
toc
```

Author's publication

International Journals

C. Andreoni, G. Orsi, C. De Maria, F. Montemurro, G. Vozzi, *In-silico Models for Dynamic Connected Cells Cultures, Mimicking Hepatocyte-Endothelial-Adipocyte Interaction Circle*, PLOS ONE,in review.

F. Montemurro, C. De Maria, G. Orsi, G. Vozzi, *Modelling and analysis of reaction and diffusion constant of gelatin crosslinked with genipin to develop scaffold for tissue engineering*, Materials, in review.

G. Fogli, G. Orsi, C. De Maria, F. Montemurro, S. Rizzo, M. Palla, G. Vozzi, *A new eye phantom for ophthalmic surgery*, RETINA The Journal of Retinal and Vitreous Diseases, in review.

G. Orsi, M. Fagnano, C. De Maria, G. Vozzi, *A new 3D Concentration Gradient Maker and its application in Building Hydrogels with a 3D Stiffness Gradient*, Annals of Biomedical Engineering, in review.

A. Micheloni, G. Orsi and G. Vozzi. *ADMET: ADipocyte METabolism Mathematical Model.* Computer Methods in Biomechanics and Biomedical Engineering, in press.

G. Orsi and R. Mauri, *Volume of mixing effect on fluid counter-diffusion*, Physics of Fluids, August 2013.

G. Valvano, G. Orsi, M. A. Guzzardi, F. Vozzi, and G. Vozzi, *CREPE: mathematical model for CRosstalking of Endothelial cells and hePatocytE metabolism*, IEEE Transactions on BioMedical Engineering, July 2013.

G. Orsi, E. Brunazzi, C. Galletti and R. Mauri, *Mixing features of two miscible liquids in T-shaped microdevices*, Chemical Engineering Transactions, June 2013.

G. Orsi, S. Ghelardoni, A. Saba, R. Zucchi and G. Vozzi, *Characterization of 3-Iodothyronamine in- vitro dynamics by mathematical modeling*, Cell Biochemistry and Biophysics, May 2013.

V. M. Chauhan, G. Orsi, A. Brown, D. Pritchard and J. W. Aylott, *Mapping the Pharyngeal and Intestinal pH of Caenorhabditis elegans and Real-Time Luminal pH Oscillations Using Extended Dynamic Range pH-Sensitive Nanosensors*, ACS Nano, May 2013.

G. Orsi, M. Roudgar, E. Brunazzi, C. Galletti and R. Mauri, *Water-Ethanol Mixing in T-Shaped Microdevices*, Chemical Engineering Science, Mar. 2013.

G. Orsi, S. Frascarelli, R. Zucchi, and G. Vozzi, *LTI models for 3-Iodothyronamine time dynamics: a multiscale view*, IEEE Transactions on BioMedical Engineering, Aug. 2011.

G. Orsi, C. De Maria, M. Guzzardi, F. Vozzi, and G. Vozzi, *HEMETβ: improvement of hepatocyte metabolism mathematical model*, Computer Methods in Biomechanics and Biomedical Engineering, Jan. 2011

Book Chapters

G. Orsi, V. Carta, and G. Vozzi, *Hydrogels with 3D gradient of mechanical properties*, Book Chapter in "Hydrogels: Synthesis, Characterization and Applications from Nova Science Publishers.

Oral Presentations

G. Orsi, C. De Maria, F. Montemurro, V. M. Chauhan, J. W. Aylott, G. Vozzi, *Nanoparticles doped sol-gel Ink for inkjet printers*, Termis 2014, 10-13 June 2014, Genova, Italy, accepted.

G. Orsi, C. De Maria, G. Vozzi, *Generation of Hydrogel Matrixes with a 3D Gradient of Mechanical Properties in a novel 3D Concentration Gradient Bioreactor*, Biofabrication 2013, November 3-6 2013, El Paso (TX), USA

G. Orsi, E. Brunazzi, C. Galletti and R. Mauri, *Mixing features of two miscible liquids in T-shaped microdevices*, 11th International Conference on Chemical & Process Engineering, June 2-5 2013, Milan, Italy

V.M. Chauhan, G. Orsi, A. P. Brown, D. I. Pritchard, and J. W. Aylott, *Mapping the Intestinal pH of C. elegans Worms Using Ratiometric Extended Dynamic Range pH-Sensitive Nanosensors*, Nanosensor Technologies for Monitoring, November 7-9 2012, London, UK

G. Orsi, F. Gattazzo and G. Vozzi, *Modelling and characterization of microfluidic nonlinear gradient maker for toxicity assessment*, International Conference on Biofabrication 2012, October 29-31 2012, Manchester, UK

G. Valvano, G. Orsi, M. A. Guzzardi, F. Vozzi, and G. Vozzi, *CREPE: a first mathematical model for CrossTalking of Endothelial cells and hePatocytE metabolism*, The Ninth IASTED International Conference on Biomedical Engineering BioMed 2012, February 15-17 2012, Innsbruck, Austria

I was also co-chairing the Cell Biology Session during this conference.

Proceedings

G. Orsi, C. De Maria, F. Montemurro, C. Andreoni, G. Vozzi, *Making hydrogels with 3D stiffness gradients with a novel 3D concentration gradient bioreac-*

tor, Congresso Nazionale di Bioingegneria (GNB) 2014, 25-27 June 2014, Pavia, Italy, accepted.

G. Orsi, C. De Maria, F. Montemurro, V. M. Chauhan, J. W. Aylott, G. Vozzi, *Nanoparticles doped sol-gel Ink for inkjet printers*, Termis 2014, 10-13 June 2014, Genova, Italy, accepted.

G. Orsi, C. De Maria, F. Montemurro, G. Vozzi, *A novel concentration gradient bioreactor by PMMA laser micromachining*, Termis 2014, 10-13 June 2014, Genova, Italy, accepted.

G. Orsi, E. Brunazzi, C. Galletti and R. Mauri, *Mixing features of two miscible liquids in T-shaped microdevices*, 11th International Conference on Chemical & Process Engineering, June 2-5 2013, Milan, Italy

G. Orsi, G. Vozzi, *Fluid dynamics characterization of a microfluidic concentration gradient maker*, Congresso Nazionale di Bioingegneria (GNB) 2012, 26-29 June 2012, Rome, Italy.

V. Carta, G. Orsi, G. Vozzi, *Hydrogels with 3D gradient of mechanical properties*, Congresso Nazionale di Bioingegneria (GNB) 2012, 26-29 June 2012, Rome, Italy.

G. Fogli, G. Orsi, G. Vozzi, *Rheological characterization of vitreous humor analogous*, Congresso Nazionale di Bioingegneria (GNB) 2012, 26-29 June 2012, Rome, Italy.

G. Valvano, G. Orsi, M. A. Guzzardi, F. Vozzi, G. Vozzi, *Mathematical modelling of Endothelin-1 effect on hepatocytes*, Congresso Nazionale di Bioingegneria (GNB) 2012, 26-29 June 2012, Rome, Italy.

G. Valvano, G. Orsi, M. A. Guzzardi, F. Vozzi, and G. Vozzi, *CREPE: a first mathematical model for CrossTalking of Endothelial cells and hePatocytE metabolism*, The Ninth IASTED International Conference on Biomedical Engineering BioMed 2012, February 15-17 2012, Innsbruck, Austria

Posters

G. Orsi, V.M. Chauhan, J.W. Aylott, G. Vozzi. *Nanosensorisation of a microfluidic concentration gradient bioreactor*, Termis 2013, 16-20 June 2013, Istanbul, Turkey.

G. Orsi, C. De Maria, G. Vozzi. *Application of a New 3D Concentration Gradient Bioreactor: Building Matrixes with a 3D Gradient of Mechanical Properties*, Termis 2013, 16-20 June 2013, Istanbul, Turkey.

G. Orsi, G. Vozzi, A. Ahluwalia. *Nanoparticles dynamics in a microfluidic gradient maker*, Bioimaging 2012, 20-21 September 2012, Porto, Portugal.

G. Orsi, G. Vozzi, *Fluid dynamics characterization of a microfluidic concentration gradient maker*, Congresso Nazionale di Bioingegneria (GNB) 2012, 26-29 June 2012, Rome, Italy.

V. Carta, G. Orsi, G. Vozzi, *Hydrogels with 3D gradient of mechanical properties*, Congresso Nazionale di Bioingegneria (GNB) 2012, 26-29 June 2012, Rome, Italy.

G. Fogli, G. Orsi, G. Vozzi, *Rheological characterization of vitreous humor analogous*, Congresso Nazionale di Bioingegneria (GNB) 2012, 26-29 June 2012, Rome, Italy.

G. Valvano, G. Orsi, M. A. Guzzardi, F. Vozzi, G. Vozzi, *Mathematical modelling of Endothelin-1 effect on hepatocytes*, Congresso Nazionale di Bioingegneria (GNB) 2012, 26-29 June 2012, Rome, Italy.

References

[1] Noo Li Jeon, Stephan K W Dertinger, Daniel T Chiu, Insung S Choi, Abraham D Stroock, and George M Whitesides. **Generation of Solution and Surface Gradients Using Microfluidic Systems**. *Processing*, (15):8311–8316, 2000. 2, 5, 10, 12, 20, 79, 82

[2] R Byron Bird, Warren E Stewart, and Edwin N Lightfoot. *Transport phenomena*. John Wiley & Sons, 2007. 3

[3] Thomas M Keenan, Chia-Hsien Hsu, and Albert Folch. **Microfluidic ?jets? for generating steady-state gradients of soluble molecules on open surfaces**. *Applied physics letters*, **89**(11):114103–114103, 2006. 3

[4] GM Walker, MS Ozers, and DJ Beebe. **Cell infection within a microfluidic device using virus gradients**. *Sensors and Actuators B: Chemical*, **98**(2):347–355, 2004. 3

[5] N. Zaari, P. Rajagopalan, S. K. Kim, a. J. Engler, and J. Y. Wong. **Photopolymerization in Microfluidic Gradient Generators: Microscale Control of Substrate Compliance to Manipulate Cell Response**. *Advanced Materials*, **16**(23-24):2133–2137, December 2004. 3, 79

[6] Jason A Burdick, Ali Khademhosseini, and Robert Langer. **Fabrication of gradient hydrogels using a microfluidics/photopolymerization process**. *Langmuir*, **20**(13):5153–5156, 2004. 3

[7] Stephan KW Dertinger, Xingyu Jiang, Zhiying Li, Venkatesh N Murthy, and George M Whitesides. **Gradients of substrate-bound laminin orient axonal specification of neurons**. *Proceedings of the National Academy of Sciences*, **99**(20):12542–12547, 2002. 3

[8] Kari A Fosser and Ralph G Nuzzo. **Fabrication of patterned multicomponent protein gradients and gradient arrays using microfluidic depletion**. *Analytical chemistry*, **75**(21):5775–5782, 2003. 3

[9] Rico C Gunawan, Eric R Choban, John E Conour, Jonathan Silvestre, Lawrence B Schook, H Rex Gaskins, Deborah E Leckband, and Paul JA Kenis. **Regiospecific control of protein expression in cells cultured on two-component counter gradients of extracellular matrix proteins**. *Langmuir*, **21**(7):3061–3068, 2005. 3

[10] Bong Geun Chung, Lisa A Flanagan, Woo Rhee, Philip H Schwartz, Abraham P Lee, Edwin S Monuki, and Noo Li. **Human neural stem cell growth and differentiation in a gradient-generating microfluidic device {**3, 5
. *Lab on a Chip*, pages 401–406, 2005.

[11] Noo Li Jeon, Harihara Baskaran, Stephan KW Dertinger, George M Whitesides, Livingston Van De Water, and Mehmet Toner. **Neutrophil chemotaxis in linear and complex gradients of interleukin-8 formed in a microfabricated device**. *Nature biotechnology*, **20**(8):826–830, 2002. 4, 5

[12] Francis Lin, Connie Minh-Canh Nguyen, Shur-Jen Wang, Wajeeh Saadi, Steven P Gross, and Noo Li Jeon. **Effective neutrophil chemotaxis is strongly influenced by mean IL-8 concentration**. *Biochemical and biophysical research communications*, **319**(2):576–581, 2004. 4, 5

[13] Francis Lin, Connie Minh-Canh Nguyen, Shur-Jen Wang, Wajeeh Saadi, Steven P Gross, and Noo Li Jeon. **Neutrophil migration in opposing chemoattractant gradients using microfluidic chemotaxis devices**. *Annals of biomedical engineering*, **33**(4):475–482, 2005. 4, 5, 6

[14] Vinay V Abhyankar, Mary A Lokuta, Anna Huttenlocher, and David J Beebe. **Characterization of a membrane-based gradient generator for use in cell-signaling studies**. *Lab on a Chip*, **6**(3):389–393, 2006. 4

[15] Hanbin Mao, Paul S Cremer, and Michael D Manson. **A sensitive, versatile microfluidic assay for bacterial chemotaxis**. *Proceedings of the National Academy of Sciences*, **100**(9):5449–5454, 2003. 4

[16] Jinpian Diao, Lincoln Young, Sue Kim, Elizabeth A Fogarty, Steven M Heilman, Peng Zhou, Michael L Shuler, and Matthew P Delisa. **A three-channel microfluidic device for generating static linear gradients and its application to the quantitative analysis of bacterial chemotaxis**. *Lab on a Chip*, pages 381–388, 2006. 4

[17] Sachiko Koyama, Dragos Amarie, Helena A Soini, Milos V Novotny, and Stephen C Jacobson. **Chemotaxis assays of mouse sperm on microfluidic devices**. *Analytical chemistry*, **78**(10):3354–3359, 2006. 4

[18] Glenn M Walker, Jiqing Sai, Ann Richmond, Mark Stremler, Chang Y Chung, and John P Wikswo. **Effects of flow and diffusion on chemotaxis studies in a microfabricated gradient generator**. *Lab on a Chip*, **5**(6):611–618, 2005. 5

REFERENCES

[19] Wajeeh Saadi, Shur-jen Wang Francis, and Noo Li Jeon. **A parallel-gradient microfluidic chamber for quantitative analysis of breast cancer cell chemotaxis**. *Biomedical Microdevices*, pages 109–118, 2006. 5

[20] Stephan KW Dertinger, Xingyu Jiang, Zhiying Li, Venkatesh N Murthy, and George M Whitesides. **Gradients of substrate-bound laminin orient axonal specification of neurons**. *Proceedings of the National Academy of Sciences*, **99**(20):12542–12547, 2002. 5

[21] Kyle Campbell and Alex Groisman. **Generation of complex concentration profiles in microchannels in a logarithmically small number of steps**. *Lab on a Chip*, pages 264–272, 2007. 11, 12, 15, 19, 20, 46, 47, 49, 79

[22] Stephan K W Dertinger, Daniel T Chiu, Noo Li Jeon, and George M Whitesides. **Generation of Gradients Having Complex Shapes Using Microfluidic Networks**. *Society*, **73**(6):1240–1246, 2001. 12, 20, 79

[23] Gianni Orsi, Mina Roudgar, Elisabetta Brunazzi, Chiara Galletti, and Roberto Mauri. **Water–ethanol mixing in T-shaped microdevices**. *Chemical Engineering Science*, **95**:174–183, 2013. 23, 25, 81, 99

[24] Chiara Galletti, Mina Roudgar, Elisabetta Brunazzi, and Roberto Mauri. **Effect of inlet conditions on the engulfment pattern in a T-shaped micro-mixer**. *Chemical Engineering Journal*, January 2012. 23, 25, 81

[25] J Hussong, R Lindken, M Pourquie, and J Westerweel. **Numerical study on the flow physics of a T-shaped micro mixer**. In *IUTAM Symposium on Advances in Micro-and Nanofluidics*, pages 191–205. Springer, 2009. 25, 49

[26] JM Ottino. **Mixing and chemical reactions a tutorial**. *Chemical Engineering Science*, **49**(24):4005–4027, 1994. 25

[27] Lily Kim, Yi-Chin Toh, Joel Voldman, and Hanry Yu. **A practical guide to microfluidic perfusion culture of adherent mammalian cells.** *Lab on a chip*, **7**(6):681–94, June 2007. 40

[28] Irena Barbulovic-Nad, Sam H Au, and Aaron R Wheeler. **A microfluidic platform for complete mammalian cell culture**. *Lab on a Chip*, **10**(12):1536–1542, 2010. 40

[29] Aigars Piruska, Irena Nikcevic, Se Hwan Lee, Chong Ahn, William R Heineman, Patrick A Limbach, and Carl J Seliskar. **The autofluorescence of plastic materials and chips measured under laser irradiation**. *Lab on a Chip*, **5**(12):1348–1354, 2005. 40

[30] Yun Seok Heo, Lourdes M Cabrera, Jonathan W Song, Nobuyuki Futai, Yi-Chung Tung, Gary D Smith, and Shuichi Takayama. **Characterization and resolution of evaporation-mediated osmolality shifts that constrain microfluidic cell culture in poly (dimethylsiloxane) devices**. *Analytical chemistry*, **79**(3):1126–1134, 2007. 40

[31] Michael W Toepke and David J Beebe. **PDMS absorption of small molecules and consequences in microfluidic applications**. *Lab Chip*, **6**(12):1484–1486, 2006. 40

[32] MA Chappell and SJ Payne. **A physiological model of the release of gas bubbles from crevices under decompression**. *Respiratory physiology & neurobiology*, **153**(2):166–180, 2006. 41

[33] Todd Thorsen, Sebastian J Maerkl, and Stephen R Quake. **Microfluidic large-scale integration**. *Science*, **298**(5593):580–584, 2002. 41

[34] H Bruus. *Theoretical Microfluidics*. Oxford Master Series in Physics. OUP Oxford, 2008. 43

[35] Hojjat Madadi and Jasmina Casals-Terré. **Long-term behavior of nonionic surfactant-added PDMS for self-driven microchips**. *Microsystem technologies*, **19**(1):143–150, 2013. 56

[36] Hirotugu Akaike. **A Bayesian analysis of the minimum AIC procedure**. *Annals of the Institute of Statistical Mathematics*, **30**(1):9–14, 1978. 56

[37] Henning Klank, Jörg P Kutter, and Oliver Geschke. **CO2-laser micromachining and back-end processing for rapid production of PMMA-based microfluidic systems**. *Lab on a Chip*, **2**(4):242–246, 2002. 64, 66

[38] Nimai C Nayak, YC Lam, CY Yue, and Ayan T Sinha. **CO2-laser micromachining of PMMA: the effect of polymer molecular weight**. *Journal of Micromechanics and Microengineering*, **18**(9):095020, 2008. 64

[39] Ting-Fu Hong, Wei-Jhong Ju, Ming-Chang Wu, Chang-Hsien Tai, Chien-Hsiung Tsai, and Lung-Ming Fu. **Rapid prototyping of PMMA microfluidic chips utilizing a CO2 laser**. *Microfluidics and nanofluidics*, **9**(6):1125–1133, 2010. 64, 67

[40] Jagannathan Narasimhan and Ian Papautsky. **Polymer embossing tools for rapid prototyping of plastic microfluidic devices**. *Journal of Micromechanics and Microengineering*, **14**(1):96, 2004. 66

[41] Liying Yao, Baoan Liu, Tao Chen, Shibing Liu, and Tiechuan Zuo. **Micro flow-through PCR in a PMMA chip fabricated by KrF excimer laser**. *Biomedical microdevices*, **7**(3):253–257, 2005. 66

[42] Biao Li, Hui Yu, Andre Sharon, and Xin Zhang. **Rapid three-dimensional manufacturing of microfluidic structuresusing a scanning laser system**. *Applied physics letters*, **85**(12):2426–2428, 2004. 66

[43] R Srinivasan. **Ablation of polymethyl methacrylate films by pulsed (ns) ultraviolet and infrared (9.17 μm) lasers: A comparative study by ultrafast imaging**. *Journal of applied physics*, **73**(6):2743–2750, 1993. 66, 67

[44] Ji-Yen Cheng, Cheng-Wey Wei, Kai-Hsiung Hsu, and Tai-Horng Young. **Direct-write laser micromachining and universal surface modification of PMMA for device development**. *Sensors and Actuators B: Chemical*, **99**(1):186–196, 2004. 66

[45] Detlef Snakenborg, Henning Klank, and Jörg P Kutter. **Microstructure fabrication with a CO2 laser system**. *Journal of Micromechanics and microengineering*, **14**(2):182, 2004. 67

[46] József Zákány, Marie Kmita, and Denis Duboule. **A dual role for Hox genes in limb anterior-posterior asymmetry.** *Science*, **304**(5677):1669–72, 2004. 78

[47] Wolfgang Driever and Christiane Nüsslein-Volhard. **A gradient of bicoid protein in Drosophila embryos**. *Cell*, **54**(1):95–104, July 1988. 78

[48] Marcos Nahmad and Arthur D Lander. **Spatiotemporal mechanisms of morphogen gradient interpretation.** *Current opinion in genetics development*, **21**(6):726–731, 2011. 78

[49] Katherine W Rogers and Alexander F Schier. **Morphogen Gradients: From Generation to Interpretation.** *Annual Review of Cell and Developmental Biology*, **27**(July):377–407, 2010. 78

[50] A M Turing. **The Chemical Basis of Morphogenesis**. *Philosophical Transactions of the Royal Society B Biological Sciences*, **237**(641):37–72, 1952. 78

[51] Karen S Ho and Matthew P Scott. **Sonic hedgehog in the nervous system: functions, modifications and mechanisms.** *Current Opinion in Neurobiology*, **12**(1):57–63, 2002. 78

[52] Edwina McGlinn and Clifford J Tabin. **Mechanistic insight into how Shh patterns the vertebrate limb.** *Current opinion in genetics development*, **16**(4):426–432, 2006. 78

[53] D Hu and JA Helms. **The role of sonic hedgehog in normal and abnormal craniofacial morphogenesis**. *Development*, **126**(21):4873–4884, November 1999. 78

[54] Marc Fuccillo, Alexandra L Joyner, and Gord Fishell. **Morphogen to mitogen: the multiple roles of hedgehog signalling in vertebrate neural development.** *Nature Reviews Neuroscience*, **7**(10):772–783, 2006. 78

[55] Stéphane Nédelec, Mirza Peljto, Peng Shi, Mackenzie W Amoroso, Lance C Kam, and Hynek Wichterle. **Concentration-dependent requirement for local protein synthesis in motor neuron subtype-specific response to axon guidance cues.** *The Journal of neuroscience : the official journal of the Society for Neuroscience*, **32**(4):1496–506, January 2012. 78

[56] Matthias P Lutolf, Penney M Gilbert, and Helen M Blau. **Designing materials to direct stem-cell fate.** *Nature*, **462**(7272):433–41, November 2009. 78

[57] Gera Neufeld, Tzafra Cohen, Stela Gengrinovitch, and Zoya Poltorak. **Vascular endothelial growth factor (VEGF) and its receptors**. *FASEB J*, **13**(1):9–22, January 1999. 78

[58] Anne Eichmann, Ferdinand Le Noble, Monica Autiero, and Peter Carmeliet. **Guidance of vascular and neural network formation.** *Current Opinion in Neurobiology*, **15**(1):108–115, 2005. 78

[59] Anil Prasad, Zahida Qamri, Jane Wu, and Ramesh K Ganju. **Slit-2/Robo-1 modulates the CXCL12/CXCR4-induced chemotaxis of T cells.** *Journal of leukocyte biology*, **82**(3):465–76, September 2007. 78

[60] Adam J Engler, Shamik Sen, H Lee Sweeney, and Dennis E Discher. **Matrix elasticity directs stem cell lineage specification.** *Cell*, **126**(4):677–89, August 2006. 79

[61] Justin R Tse and Adam J Engler. **Stiffness gradients mimicking in vivo tissue variation regulate mesenchymal stem cell fate.** *PloS one*, **6**(1):e15978, January 2011. 79

[62] C M Lo, H B Wang, M Dembo, and Y L Wang. **Cell movement is guided by the rigidity of the substrate.** *Biophysical journal*, **79**(1):144–52, July 2000. 79

[63] A Domingo. **Exponential gradient maker using a disposable syringe.** *Analytical Biochemistry*, **189**(1):88–90, 1990. 79

[64] Daniel Irimia, Dan A Geba, and Mehmet Toner. **Universal Microfluidic Gradient Generator**. *Society*, **78**(10):3472–3477, 2006. 79

[65] Kang Sun, Zongxing Wang, and Xingyu Jiang. **Modular microfluidics for gradient generation**. (April):1536–1543, 2008. 79

[66] Ji-Yen Cheng, Meng-Hua Yen, Ching-Te Kuo, and Tai-Horng Young. **A transparent cell-culture microchamber with a variably controlled concentration gradient generator and flow field rectifier**. *Biomicrofluidics*, **2**(2):24105, 2008. 80

[67] Robert H Perry and Don W Green. *Perry's Chemical Engineers' Handbook*, **7** of *Chemical Engineers Handbook*. McGraw-Hill, 2008. 80

[68] Xingyu Jiang, Qiaobing Xu, Stephan K W Dertinger, Abraham D Stroock, Tzung-May Fu, and George M Whitesides. **A general method for patterning gradients of biomolecules on surfaces using microfluidic networks.** *Analytical Chemistry*, **77**(8):2338–2347, 2005. 80

[69] Yoshihiro Morishita and Yoh Iwasa. **Accuracy of positional information provided by multiple morphogen gradients with correlated noise**. *Physical Review E*, **79**(6):061905, June 2009. 81

[70] Y. Morishita and Y. Iwasa. **Optimal placement of multiple morphogen sources**. *Physical Review E*, **77**(4):041909, April 2008. 81

[71] Annalisa Tirella, Mauro Marano, Federico Vozzi, and Arti Ahluwalia. **A microfluidic gradient maker for toxicity testing of bupivacaine and lidocaine.** *Toxicology in Vitro*, **22**(8):1957–64, December 2008. 82

[72] Giovanni Vozzi, Daniele Mazzei, Annalisa Tirella, Federico Vozzi, and Arti Ahluwalia. **Finite element modelling and design of a concentration gradient generating bioreactor: application to biological pattern formation and toxicology.** *Toxicology in vitro : an international journal published in association with BIBRA*, **24**(6):1828–37, September 2010. 82

[73] John Crank. *The Mathematics of Diffusion*. 1979. 83, 92

[74] Giovanni Vozzi, Christopher Flaim, Arti Ahluwalia, and Sangeeta Bhatia. **Fabrication of PLGA scaffolds using soft lithography and microsyringe deposition.** *Biomaterials*, **24**(14):2533–40, June 2003. 85

[75] Arthur D. Lander. **Morpheus Unbound: Reimagining the Morphogen Gradient**. *Cell*, **128**(2):245–256, 2007. 87

[76] P.Huw Williams, Anja Hagemann, Marcos González-Gaitán, and James C. Smith. **Visualizing Long-Range Movement of the Morphogen Xnr2 in the Xenopus Embryo**. 2004. 87

[77] A Tirella, G Mattei, and A Ahluwalia. **Strain rate viscoelastic analysis of soft and highly hydrated biomaterials.** *Journal of biomedical materials research. Part A*, August 2013. 88

[78] Gianni Orsi, Veronica Carta, and Giovanni Vozzi. **Hydrogels with 3D Gradient of Mechanical Properties**. In *Hydrogels: Synthesis, Characterization and Applications*. NovaPublishers, New York, 2012. 88

[79] Philippe Pascal, Jean Duhamel, Yongcai Wang, Mitchell A. Winnik, Xiao Xia Zhu, Peter Macdonald, Donald H. Napper, and Robert G. Gilbert. **Fluorescence depolarization and quenching studies of acenaphthalene-labelled poly(acrylamide) in water**. *Polymer*, **34**(6):1134–1140, 1993. 93

[80] Jess V Nauman, Phil G Campbell, Frederick Lanni, and John L Anderson. **Diffusion of insulin-like growth factor-I and ribonuclease through fibrin gels.** *Biophysical journal*, **92**(12):4444–4450, 2007. 93

[81] Jing-Lin Fu, Qun Fang, Ting Zhang, Xin-Hua Jin, and Zhao-Lun Fang. **Laser-induced fluorescence detection system for microfluidic chips based on an orthogonal optical arrangement.** *Analytical Chemistry*, **78**(11):3827–3834, 2006. 94

[82] C Galletti, S Pintus, and E Brunazzi. **Effect of shaft eccentricity and impeller blade thickness on the vortices features in an unbaffled vessel**. *Chemical Engineering Research and Design*, **87**(4):391–400, 2009. 94

[83] Ian Glasgow, Samuel Lieber, and Nadine Aubry. **Parameters influencing pulsed flow mixing in microchannels.** *Analytical chemistry*, **76**(16):4825–32, August 2004. 99

[84] Dongwon Lee, Sirajud Khaja, Juan C Velasquez-Castano, Madhuri Dasari, Carrie Sun, John Petros, W Robert Taylor, and Niren Murthy. **In vivo imaging of hydrogen peroxide with chemiluminescent nanoparticles**. *Nature materials*, **6**(10):765–769, 2007. 104

[85] Takeharu Nagai, Asako Sawano, Eun Sun Park, and Atsushi Miyawaki. **Circularly permuted green fluorescent proteins engineered to sense Ca2+**. *Proceedings of the National Academy of Sciences*, **98**(6):3197–3202, 2001. 104

[86] Takeharu Nagai, Shuichi Yamada, Takashi Tominaga, Michinori Ichikawa, and Atsushi Miyawaki. **Expanded dynamic range of fluorescent indicators for Ca2+ by circularly permuted yellow fluorescent proteins**. *Proceedings of the National Academy of Sciences of the United States of America*, **101**(29):10554–10559, 2004. 104

[87] Junichi Nakai, Masamichi Ohkura, and Keiji Imoto. **A high signal-to-noise Ca2+ probe composed of a single green fluorescent protein**. *Nature biotechnology*, **19**(2):137–141, 2001. 104

[88] Philipp Niethammer, Clemens Grabher, A Thomas Look, and Timothy J Mitchison. **A tissue-scale gradient of hydrogen peroxide mediates rapid wound detection in zebrafish**. *Nature*, **459**(7249):996–999, 2009. 104

[89] Guoqing Zhang, Gregory M Palmer, Mark W Dewhirst, and Cassandra L Fraser. **A dual-emissive-materials design concept enables tumour hypoxia imaging**. *Nature materials*, **8**(9):747–751, 2009. 104

[90] Walter J Bowyer, Wenying Xu, and JN Demas. **Determining proton diffusion in polymer films by lifetimes of luminescent complexes measured in the frequency domain**. *Analytical chemistry*, **81**(1):378–384, 2008. 104

[91] Gregor Liebsch, Ingo Klimant, Christian Krause, and Otto S Wolfbeis. **Fluorescent imaging of pH with optical sensors using time domain dual lifetime referencing**. *Analytical chemistry*, **73**(17):4354–4363, 2001. 104

[92] Arpan S Desai, Veeren M Chauhan, Angus PR Johnston, Tim Esler, and Jonathan W Aylott. **Fluorescent nanosensors for intracellular measurements: synthesis, characterization, calibration, and measurement**. *Frontiers in physiology*, **4**, 2013. 104, 105

[93] STEVEN Bassnett, L Reinisch, and DAVID C Beebe. **Intracellular pH measurement using single excitation-dual emission fluorescence ratios**. *American Journal of Physiology-Cell Physiology*, **258**(1):C171–C178, 1990. 104

[94] Yun Chen and Edgar A Arriaga. **Individual acidic organelle pH measurements by capillary electrophoresis**. *Analytical chemistry*, **78**(3):820–826, 2006. 104

[95] Veeren M Chauhan, Gary R Burnett, and Jonathan W Aylott. **Dual-fluorophore ratiometric pH nanosensor with tuneable pKa and extended dynamic range**. *Analyst*, **136**(9):1799–1801, 2011. 104, 105, 110

[96] Ludmila V Deriy, Erwin A Gomez, Guangping Zhang, Daniel W Beacham, Jessika A Hopson, Alexander J Gallan, Pavel D Shevchenko, Vytautas P Bindokas, and Deborah J Nelson. **Disease-causing mutations in the cystic fibrosis transmembrane conductance regulator determine the functional responses of alveolar macrophages**. *Journal of biological chemistry*, **284**(51):35926–35938, 2009. 104

[97] Veeren M Chauhan, Gianni Orsi, Alan Brown, David I Pritchard, and Jonathan W Aylott. **Mapping the Pharyngeal and Intestinal pH of Caenorhabditis elegans and Real-Time Luminal pH Oscillations Using Extended Dynamic Range pH-Sensitive Nanosensors**. *ACS nano*, 2013. 104, 105, 106, 108, 110, 117

[98] Heather A Clark, Marion Hoyer, Martin A Philbert, and Raoul Kopelman. **Optical nanosensors for chemical analysis inside single living cells. 1. Fabrication, characterization, and methods for intracellular delivery of PEBBLE sensors**. *Analytical Chemistry*, **71**(21):4831–4836, 1999. 105

[99] Andrew Burns, Prabuddha Sengupta, Tara Zedayko, Barbara Baird, and Ulrich Wiesner. **Core/Shell Fluorescent Silica Nanoparticles for Chemical Sensing: Towards Single-Particle Laboratories**. *Small*, **2**(6):723–726, 2006. 105

[100] Mark L Graber, Douglas C DiLillo, Bradford L Friedman, and Enrique Pastoriza-Munoz. **Characteristics of fluoroprobes for measuring intracellular pH**. *Analytical biochemistry*, **156**(1):202–212, 1986. 105, 107

[101] Deboleena Sarkar, Arabinda Mallick, Basudeb Haldar, and Nitin Chattopadhyay. **Ratiometric spectroscopic response of pH sensitive probes: An alternative strategy for multidimensional sensing**. *Chemical Physics Letters*, **484**(4):168–172, 2010. 105

[102] Richard P Haugland. *The handbook: a guide to fluorescent probes and labeling technologies*. Molecular probes, 2005. 105

[103] Honghao Sun, Kristoffer Almdal, and Thomas L Andresen. **Expanding the dynamic measurement range for polymeric nanoparticle pH sensors**. *Chemical Communications*, **47**(18):5268–5270, 2011. 105

[104] Rikke V Benjaminsen, Honghao Sun, Jonas R Henriksen, Nynne M Christensen, Kristoffer Almdal, and Thomas L Andresen. **Evaluating nanoparticle sensor design for intracellular pH measurements**. *ACS nano*, **5**(7):5864–5873, 2011. 105

[105] Aniruddha Ray, Yong-Eun Koo Lee, Remy Elbez, and Raoul Kopelman. **Targeted nanosensor aided three-dimensional pH mapping in tumor spheroids using two-photon microscopy**. In *SPIE BiOS*, pages 822613–822613. International Society for Optics and Photonics, 2012. 107

[106] Anja Schulz, Jana Wotschadlo, Thomas Heinze, and Gerhard J Mohr. **Fluorescent nanoparticles for ratiometric pH-monitoring in the neutral range**. *Journal of Materials Chemistry*, **20**(8):1475–1482, 2010. 107

[107] Hooisweng Ow, Daniel R Larson, Mamta Srivastava, Barbara A Baird, Watt W Webb, and Ulrich Wiesner. **Bright and stable core-shell fluorescent silica nanoparticles**. *Nano letters*, **5**(1):113–117, 2005. 107

[108] Kerry P McNamara, Thuvan Nguyen, Gabriela Dumitrascu, Jin Ji, Nitsa Rosenzweig, and Zeev Rosenzweig. **Synthesis, characterization, and application of fluorescence sensing lipobeads for intracellular pH measurements**. *Analytical chemistry*, **73**(14):3240–3246, 2001. 108

[109] Inger Wendelhag, Quan Liang, Tomas Gustavsson, and John Wikstrand. **A new automated computerized analyzing system simplifies readings and reduces the variability in ultrasound measurement of intima-media thickness**. *Stroke*, **28**(11):2195–2200, 1997. 110

[110] Paul G Kotula, Michael R Keenan, and Joseph R Michael. **Automated analysis of SEM X-ray spectral images: a powerful new microanalysis tool**. *Microscopy and Microanalysis*, **9**(01):1–17, 2003. 110

[111] J Martin Bland and DouglasG Altman. **Statistical methods for assessing agreement between two methods of clinical measurement**. *The lancet*, **327**(8476):307–310, 1986. 111, 113

REFERENCES

[112] G Orsi, C De Maria, M Guzzardi, F Vozzi, and G Vozzi. **HEMETβ: improvement of hepatocyte metabolism mathematical model.** *Computer Methods in Biomechanics and Biomedical Engineering*, **14**(1986):1, 2011. 113

[113] Robert WM Wedderburn. **Quasi-likelihood functions, generalized linear models, and the Gauss?Newton method**. *Biometrika*, **61**(3):439–447, 1974. 113

[114] Mary C Hill. *Methods and guidelines for effective model calibration*. US Geological Survey Denver, CO, USA, 1998. 113

[115] Xu-dong Wang, Robert J Meier, and Otto S Wolfbeis. **Fluorescent pH-Sensitive Nanoparticles in an Agarose Matrix for Imaging of Bacterial Growth and Metabolism**. *Angewandte Chemie*, **125**(1):424–427, 2013. 118

[116] Stephan Schreml, Robert J Meier, Otto S Wolfbeis, Michael Landthaler, Rolf-Markus Szeimies, and Philipp Babilas. **2D luminescence imaging of pH in vivo**. *Proceedings of the National Academy of Sciences*, **108**(6):2432–2437, 2011. 118

[117] Andreas Chrambach. **practice of quantitative gel electrophoresis**. 1985. 118

[118] QINWEI Shi and GEORGE Jackowski. **One-dimensional polyacrylamide gel electrophoresis**. *Gel electrophoresis of proteins: A practical approach, 3rd ed. Oxford University Press, Oxford*, pages 1–52, 1998. 118

[119] C Tonda-Turo, P Gentile, S Saracino, Valeria Chiono, VK Nandagiri, G Muzio, RA Canuto, and G Ciardelli. **Comparative analysis of gelatin scaffolds crosslinked by genipin and silane coupling agent**. *International journal of biological macromolecules*, **49**(4):700–706, 2011. 119

[120] An-Chong Chao. **Preparation of porous chitosan/GPTMS hybrid membrane and its application in affinity sorption for tyrosinase purification with¡ i¿ Agaricus bisporus¡/i¿**. *Journal of membrane science*, **311**(1):306–318, 2008. 119

[121] Iisoto Grizzi, H Garreau, S Li, and M Vert. **Hydrolytic degradation of devices based on poly (DL-lactic acid) size-dependence**. *Biomaterials*, **16**(4):305–311, 1995. 119

[122] Thibaud Coradin, Saliou Bah, and Jacques Livage. **Gelatine/silicate interactions: from nanoparticles to composite gels**. *Colloids and Surfaces B: Biointerfaces*, **35**(1):53–58, 2004. 119

[123] S Smitha, P Shajesh, P Mukundan, TDR Nair, and KGK Warrier. **Synthesis of biocompatible hydrophobic silica–gelatin nano-hybrid by sol–gel process**. *Colloids and surfaces B: Biointerfaces*, **55**(1):38–43, 2007. 119

[124] S Smitha, P Mukundan, P Krishna Pillai, and KGK Warrier. **Silica–gelatin bio-hybrid and transparent nano-coatings through sol–gel technique**. *Materials chemistry and physics*, **103**(2):318–322, 2007. 119

[125] Lei Ren, Kanji Tsuru, Satoshi Hayakawa, and Akiyoshi Osaka. **Synthesis and characterization of gelatin-siloxane hybrids derived through sol-gel procedure**. *Journal of sol-gel science and technology*, **21**(1-2):115–121, 2001. 119

[126] Carmelo De Maria, Julio Rincon, Alonso A Duarte, Giovanni Vozzi, and Thomas Boland. **A new approach to fabricate agarose microstructures**. *Polymers for Advanced Technologies*, **24**(10):895–902, 2013. 124, 125

[127] Tim Still, Peter J Yunker, and Arjun G Yodh. **Surfactant-induced Marangoni eddies alter the coffee-rings of evaporating colloidal drops**. *Langmuir*, **28**(11):4984–4988, 2012. 125